SIMULATION AND TEST OF THE AUXILIARY BEARINGS AND THEIR DAMPERS IN MAGNETIC BEARING SYSTEMS

A Dissertation

by

XIAO KANG

Submitted to the Office of Graduate and Professional Studies of
Texas A&M University
in partial fulfillment of the requirements for the degree of

DOCTOR OF PHILOSOPHY

Chair of Committee,	Alan Palazzolo
Committee Members,	Won-Jong Kim
	Chii-Der Suh
	Peter Keating
Head of Department,	Andreas A. Polycarpou

May 2019

Major Subject: Mechanical Engineering

ABSTRACT

Auxiliary bearings (AB) support the rotor and protect the magnetic bearing (AMB) system when the AMB is disabled due to power loss or excessive loads.

Firstly, this study developed a high fidelity nonlinear elastic-thermal coupled ball bearing type auxiliary bearing model and a two-dimensional plane strain elastic-thermal couple sleep type auxiliary bearing model. These two models can effectively predict the dynamic and thermal response when a flexible rotor drops onto a ball bearing type or a sleeve type auxiliary bearing. Additionally, the rain flow counting method is utilized to count the stress cycles and calculate the bearing fatigue lives along with the Miner's rule.

Secondly, because large vibration and contact forces will occur during rotor drops, this study demonstrates that installing a damping device along with the AB can yield extended AB fatigue life, protect the AMB, reduce vibration, contact force and AB heating. The introduced high fidelity damper models include the squeeze film damper, wavy spring and elastomer O-ring.

Thirdly, a rotor-auxiliary bearing test rig is developed to experimentally investigate the rotor's drop behavior and the dampers effect.

DEDICATION

To my parents and wife for all their love and encouragement.

ACKNOWLEDGEMENTS

I would like to thank my advisor, Dr. Palazzolo, who gave me a lot of guidance, brilliant ideas, encouragements and support during these years, and who sets an example to me by having a passion for his research and work.

Thank you to my committee members, Dr. Kim, Dr. Suh, and Dr. Keating, for their guidance and encouragement.

Thanks also go to my friends and colleagues and the department faculty and staff for making my time at Texas A&M University a great experience. I also want to extend my gratitude to the Turbomachinery Research Consortium, which financially supported the project.

Finally, thanks to my mother and father for their encouragement and to my wife for her patience and love.

CONTRIBUTOR AND FUNDING SOURCES

Contributor:

This work was supported by a thesis (or) dissertation committee consisting of Dr. Alan Palazzolo, Dr. Chii-Der Suh, and Dr. Won-Jong Kim of the Department of Mechanical Engineering and Dr. Peter Keating of the Department of Civil Engineering.

The assembling of the test set up and the rotor drop tests described in Chapter seven were assisted by Steven Farris, Shyam Sundar, and Dr. Xiaojun Li.

All other work conducted for the thesis (or) dissertation was completed by the student independently.

Funding Sources:

This work was financially supported by the Turbomachinery Research Consortium.

NOMENCLATURE

$U(t)$	Periodic contact function
u	Displacement of the AB inner race
v	Displacement of the AB ball
w	Displacement of the AB outer race
μ_r	Friction coefficient between rotor and the AB inner race
K_l	Line contact stiffness
D_{imb}	Maximum deflection purely caused by the imbalance
D_b	Bearing ball diameter
φ_j	Circumferential location of the j'th ball
D	Static deflection of the rotor-auxiliary bearing
WS	Wavy spring
AB	Auxiliary bearing
CB	Catcher bearing
δ	Penetration
v_{irel}	Relative velocity between rotor and bearing
Ω	Rotational Speed
ζ_i	Damping coefficient under frequency no i
ω_i	Frequency no. i
AMB	Active Magnetic Bearing

TABLE OF CONTENTS

Page

LIST OF FIGURES

Page

LIST OF TABLES

Page

CHAPTER I

INTRODUCTION

This part introduces the background of auxiliary bearings in magnetic bearing systems and their previous researches. Additionally, the novel contribution of this research is stated.

1.1 Auxiliary Bearings in Magnetic Bearing Systems

The active magnetic bearing has been widely used in the industrial fields because it can provide non-friction, oil free working conditions. The Auxiliary Bearing (AB), as shown in Figure 1, is a crucial part in the Active Magnetic Bearing (AMB) system because it can not only support the rotor when the AMB fails but protect the AMB from being impacted when the rotor has large vibration.

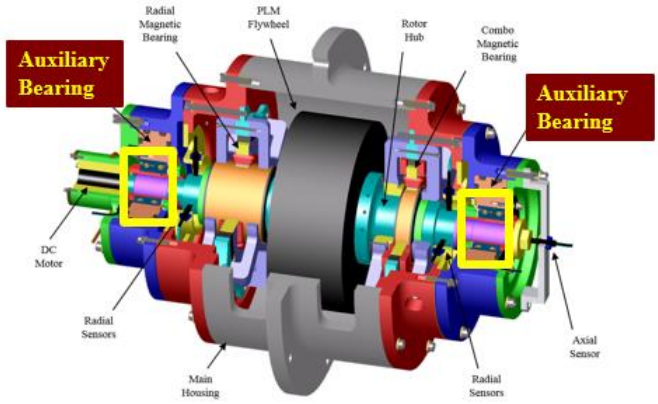

Figure 1 Auxiliary bearings in magnetic bearing systems

When the AMB fails due to power supply failure or other issues, the rotor will drop with a high rotational speed and impact the auxiliary bearing (AB) or Catcher Bearing

(CB) system intensively. During such process, significant contact forces and the thermal power caused by the friction may impair the AB and even the AMB. This result may include plastic deformations, subsurface initiated spalling and thermal abrasion wear, and all will lead to severe noise, vibration and even damage of the entire AMB system. Thus, it is essential to analyze the dynamic and thermal behavior of the rotor and the AB system during rotor's drop process. Only in this way can the proper approaches of the AB design be found so as to minimize not only the impact force but the induced heating and prolong the fatigue life of the AB.

1.2 Literature Review

Numerous researchers have modeled or tested the ball bearing type CB. Gelin et al [1] analyzed the dynamic behavior of flexible rotor drop onto the auxiliary bearing, while the Coulomb friction was neglected. T. Ishii et al. simulated the transient response of the rotor drop onto the CB in 1991 with a Jeffcott rotor model, and the optimal damping was selected to prevent the reverse whirl [2]. Sun et al [3] developed a detail ball bearing model in 2003 and added the 1D thermal model in 2006 [4]. Lee et al. [5] developed a nonlinear ball bearing model where the rain flow counting method was used to calculate the auxiliary bearing fatigue life. Wilkes et al [6] modeled the axial friction between the rotor flange and the axial face of the ball bearing type auxiliary bearing. The axial friction was believed to induce the forward whirl when the vertical arranged rotor dropped onto the auxiliary bearing. All the aforementioned researchers were committed to establish the high-fidelity model of the auxiliary bearing and the rotor, such that both the dynamic responses and the thermal behaviors of each component can be considered.

The above AB models typically omitted high fidelity models of the dampers that are frequently installed with the ABs to mitigate excessive vibration and reduced AB life. The squeeze film damper SFD is a commonly used energy dissipation device used to dampen rotating machinery vibration and is widely used in industry. The SFD typically employs a supply groove to ensure adequate lubricant flow into the film land [7]. The geometry of the AB and SFD with central groove are illustrated in Figure 2. The fluidic forces from the groove were originally ignored due to their relative large depths, however test and theoretical results have shown large added mass coefficients in grooved SFD, i.e. Delgado [7]. This reference provides a linear fluid inertia bulk flow model for the analysis of the forced response of SFDs. The effective clearance is applied to replace the actual clearance of the groove based on the experimental data and the qualitative observations of the laminar flow pattern through annular cavities. Their simulation results of the SFD force coefficients correlated well with the experiments.

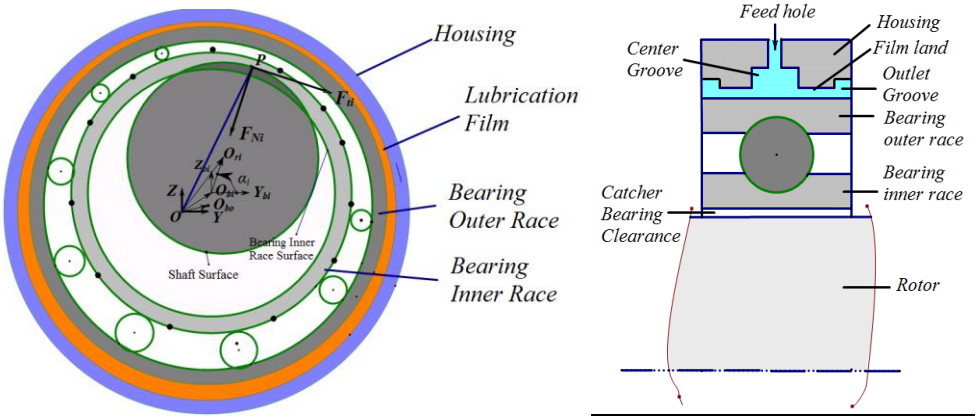

a. Front view b. Cross view

Figure 2. Central Groove SFD integrated into an auxiliary bearing system

Some theoretical and experimental research has been performed with a SFD integrated into the AB system. Sun et al. [4] included an open-ended SFD and thermal analysis in an AB - rotor drop simulation study. However the groove of the SFD and the fluid inertia effect were ignored. Murphy et al [8] integrated the SFD into the AB system of a magnetic bearing levitated flywheel, however a rotor drop simulation was not reported.

Squeeze film dampers SFD can efficiently reduce the contact force. However, magnetic bearings are often installed in machinery that is "oil-free" to reduce the possibility of contamination or for environmental needs or concerns. This and cost considerations would preclude the use of SFD for AB in these applications. "O" Ring OR and WFS provide lower cost, oil free options for AB damping devices [6] [9] and are widely used for suppressing rotating machinery vibrations.

OR and other elastomer dampers are widely used to provide damping to rolling element bearing because of their simplicity, inherent combination of stiffness and damping and lack of need for seals or an oil supply. In 1978, Smalley et al [10] experimentally investigated the dynamic characteristics of OR and obtained their frequency-dependent-stiffness and loss coefficients with different materials, temperatures, squeeze ratios, stretch ratios etc. This reference contains much valuable design information for incorporating OR into SFD and ball bearings. The present paper integrates the OR characteristics measured in [10] into the high fidelity AB ball bearing model provided in chapter 2. An approach for converting the frequency dependent stiffness and loss coefficient data provided in reference [10] to a transfer function representation is presented

in chapter 5. This latter representation provides a form that is readily integrated into the total system model for transient response simulation. Figure 3 illustrates the integration of OR in the overall ball bearing – AB design.

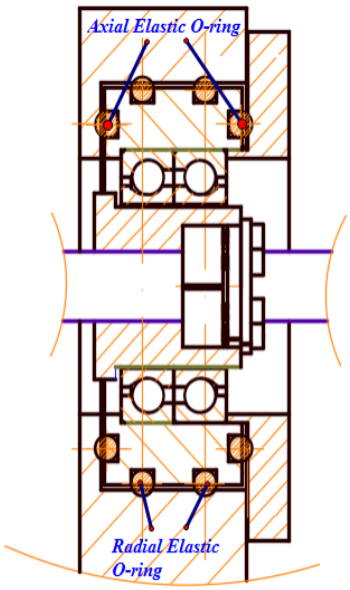

Figure 3. Ball Bearing Type AB with OR Supports

O-Rings are inserted in grooves machined into a steel cartridge assembled between the AB and the housing in Figure 3. The groove depths can be adjusted by inserting shims to change the squeeze ratio of the O-Ring. The influence of the different squeeze ratios on the dynamic and thermal behavior after a rotor drop is studied, and the optimal squeeze ratio is selected.

Another widely applied damper type is the wavy friction spring WFS (corrugated ribbon), which is shown in

Figure 4. Some of the AB literature does consider damping devices such as the corrugated ribbon from Wilkes et al [6] and the tolerance ring from Zhu et al [9]. The shape of the metallic sheet WFS is wavelike, and it is placed between the ball bearing outer race and the bearing housing. The WFS can increase the manufacturing tolerances of the bearing housing to reduce the cost, and the WFS has been applied to AB in [6] [11] . The stiffness of the wavy spring is comparatively lower than the AB housing, thereby lowering the contact force after a rotor drops. Very importantly, the Coulomb friction forces due to internal sliding between the bearing outer race, the wavy spring (WS) and the housing, will provide extra damping to increase the stability of the rotor-auxiliary bearing system.

Figure 4 WFS Ribbon Spring

Some authors have developed mathematical models for the WFS. Ransom et al. [11] and Wilkes et al [6] developed a mathematical model of the WFS represented by the force equation

$$F_{Dmpr} = yk_0\,(1 + i\,\xi) \tag{1}$$

"where k_0 is a (unspecified) function of the ribbon geometry and ξ represents the anticipated coefficient of friction. The real portion of this force is in the radial direction while the imaginary component is in the tangential direction, opposing whirl". This approach assumes a uniform bump stiffness distribution around the circumference with only sliding contact, and determination of k_0 must be performed experimentally or by some unspecified analytical means.

Zhu et al. [9], [12] numerically and experimentally studied the influence of WFS on rotor drop events. Their AB included a single ball bearing or a bearing within a bearing (double-decker). Their experiments showed that the WFS has positive effects on reducing contact force. Their analytical model includes a vector sum of forces from the multiple bumps around the circumference of the WFS. The individual bump stiffness is obtained from (2) in which an approximate formula for an individual bump stiffness of a tolerance ring is provided as

$$K_{bump} = 4.8 * E * \mathrm{w} * \left(\frac{t}{p}\right)^3 \tag{2}$$

where E is the elastic modulus for the material (kN/mm), w is the width, t is the thickness and p is the wave pitch (mm). As in [6] and [12] WFS inertia is neglected and the friction derived energy dissipation is represented by an equivalent lumped "tolerance ring damping" constant. A formula relating this damping with the coefficient of friction is not provided so the analyst must obtain it from experiment, if possible.

In the auxiliary bearing system, the wavy spring (WS) is only constrained radially by the AB housing surface. When the WS is compressed by the AB outer race, it will slide along the tangential direction of the contact surfaces. The sliding will generate some Coulomb friction forces, which is helpful for the energy dissipation.

Most of the literature focuses on ball bearing type auxiliary bearing. Actually, other bearing types, such as the sleeve type auxiliary bearing by WAUKESHA's rotor de-levitation system (RDS), are also used in industries and thus investigated by engineers [13]. There are also some researchers who have investigated sleeve type auxiliary bearing. In 1995, Swanson et al numerically [14] [15] and experimentally [14] analyzed rotor drop onto sleeve type auxiliary bearing. Parametric studies including the lubrication conditions, imbalance, support conditions and auxiliary bearing types, and Swanson et al concluded that lower imbalance, better lubrication and soft support were recommended for the auxiliary bearing design. Wilkes et al numerically and experimentally analyzed the multi-contact dry-friction whip and whirl [16], such research involves the contact model between the rotor and the stator, which is similar as the contact between the rotor and the auxiliary bearing.

However, literatures are quite scarce about the detailed modeling of sleeve type auxiliary bearing related to the rotordynamics, thermodynamics and their coupled relationship. For the thermal analysis, most of the literature simplifies the auxiliary bearing race as a 1D lumped mass and fail to calculate the temperature distribution around the surface which will under predict the peak temperature. Therefore, the 2-dimensional

elastic thermal coupled sleeve type auxiliary bearing model need to be developed to accurately predict the local temperature of the sleeve type AB.

1.3 Novel Contribution of This Research

The present work is designed to develop high fidelity auxiliary bearings and the related damper models together with the experimental validation. The contributions and novelties of the research include:

1) Integrated a high fidelity groove squeeze film damper model considering the fluid inertia effect into the auxiliary bearing system;

2) Integrated a high fidelity wavy spring damper model into the auxiliary bearing system, considering the multi contact nodes' frictions between the wavy spring and the ABOR and the bearing housing

3) Integrated a frequency dependent elastomer O-ring model into the auxiliary bearing system.

4) Developed a 2D elastic thermal coupled plane strain sleeve type auxiliary bearing model, which can predict the 2D temperature distribution and 2D stress distribution;

5) Auxiliary bearing test rig development, enabling the contact force measurement, rotor orbit measurement, rotor rotational speed measurement, auxiliary bearing inner race measurement, eliminating the influence of the motor during rotor drop.

6) Auxiliary bearing damper system testing, investigated the influence of the auxiliary bearing dampers on the rotor drop orbit and contact forces.

CHAPTER II

HIGH FIDELITY ELASTIC THERMAL COUPLED BALL BEARING MODEL WITH LIFE PREDICTION

In this part, the detailed nonlinear elastic-thermal coupled ball bearing model is introduced. In this model, the ball bearing's inner race IR, outer race OR and balls are treated as individual bodies. The nonlinear contact forces between the IR and balls, OR and balls are all calculated. The thermal expansions of each bearing components are also updated at each time step during the numerical integration. Then, based on [5] the rain flow counting method is applied to count the stress cycles and determine the auxiliary bearing's fatigue life.

2.1 Nonlinear Ball Bearing Model

Ball bearings are commonly used as AB's in magnetic bearing applications. The contact forces between bearing races and balls are included in the following detailed model of the AB, and are treated with nonlinear, Hertzian contact representations. The nonlinear auxiliary bearing model is based on references [3] and [5]. Figure 5 illustrates the geometry of the angular contact ball bearing AB.

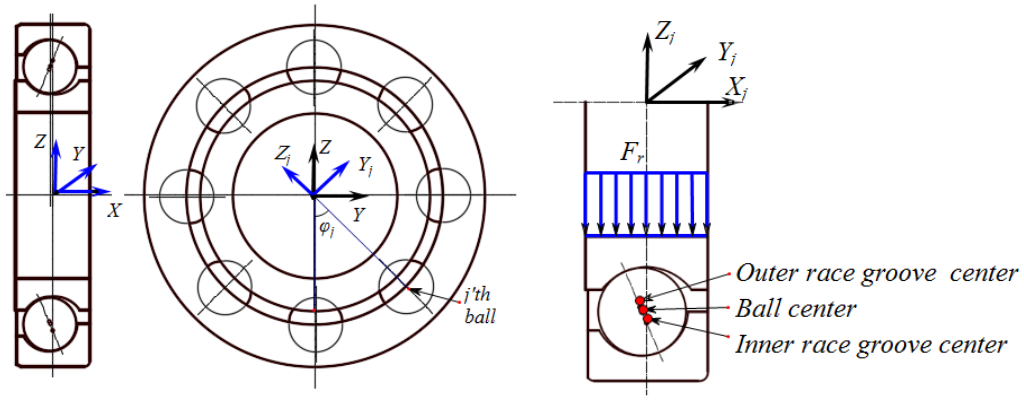

(a) (b)

Figure 5. (a) Auxiliary bearing geometric and local coordinates with respect to *j*th ball. (b) Auxiliary bearing geometric relationship for *j*th ball in its local coordinates

The symbols $X-Y-Z$ represents the global coordinates, and $X_j-Y_j-Z_j$ represents the local coordinates with respect to the *j*th bearing ball, in Figure 5. The transformation between the local coordinate and the global coordinate is

$$\begin{bmatrix} x_j \\ y_j \\ z_j \end{bmatrix} = \begin{bmatrix} 1 & 0 & 0 \\ 0 & \cos\varphi_j & \sin\varphi_j \\ 0 & -\sin\varphi_j & \cos\varphi_j \end{bmatrix} \begin{bmatrix} x \\ y \\ z \end{bmatrix} \tag{3}$$

The coordinate transformation matrix from global coordinates to the *j*th ball local coordinates is

$$T_j = \begin{bmatrix} 1 & 0 & 0 \\ 0 & \cos\varphi_j & \sin\varphi_j \\ 0 & -\sin\varphi_j & \cos\varphi_j \end{bmatrix} \tag{4}$$

The forces between the balls and the inner and outer races, are calculated in the respective ball local coordinates and then transformed to global coordinates.

Figure 6 shows the kinematic and thermal deformation displacements for the inner and outer races and the *jth* ball, where l_{oe} is the initial distance between the outer race groove center and the bearing ball center, l_{oi} is the distance between the inner race groove center and the ball center, α_0 is the initial contact angle, α_{oe} is the contact angle between the outer race and the ball after the external load is applied, α_{oi} is the contact angle between the inner race and the ball after the external load is applied, and ε_b, ε_e, ε_i are the thermal expansions of the ball, outer and inner race, respectively.

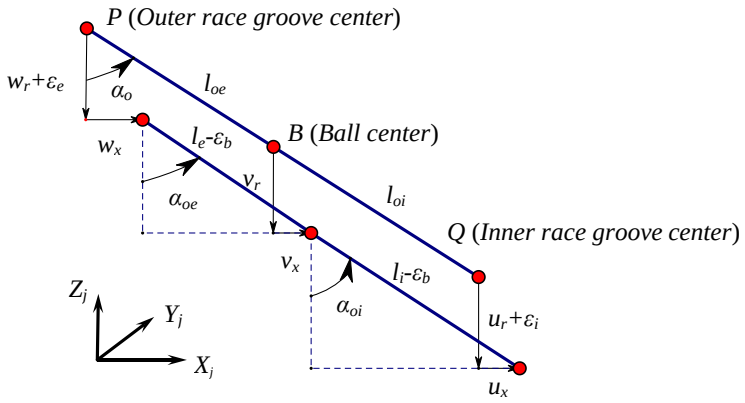

Figure 6. Kinematic and thermal deformation displacements of the races and *j*th ball

The geometric relationships among these displacements and lengths are:

$$l_{oi} = r_i - \frac{D}{2} \tag{5}$$

$$l_{oe} = r_e - \frac{D}{2} \tag{6}$$

$$\tan\alpha_{oi_j} = \frac{l_{oi}\sin\alpha_o - v_x + u_x}{l_{oi}\cos\alpha_o - v_r + u_r + \varepsilon_i} \tag{7}$$

$$\tan\alpha_{oe_j} = \frac{l_{oe}\sin\alpha_o - w_x + v_x}{l_{oe}\cos\alpha_o - w_r - \varepsilon_e + v_r} \tag{8}$$

$$l_{i_j} = \varepsilon_b + \sqrt{(l_{oi}\sin\alpha_o - v_x + u_x)^2 + (l_{oi}\cos\alpha_o - v_r + u_r + \varepsilon_i)^2} \tag{9}$$

$$l_{\varepsilon_j} = \varepsilon_b + \sqrt{(l_{oe}\sin\alpha_o - w_x + v_x)^2 + (l_{oe}\cos\alpha_o - w_r - \varepsilon_e + v_x)^2} \tag{10}$$

The penetration δ_{i_j} between the inner race and the *j*th bearing ball is

$$\delta_{i_j} = l_i - l_{oi} \tag{11}$$

The penetration δ_{e_j} between the outer race and the *j*th bearing ball is

$$\delta_{e_j} = l_e - l_{oe} \tag{12}$$

The contact force between the inner race and the *j*th ball is

$$Q_{i_j} = k_i\delta_i^{\frac{3}{2}}(\frac{3}{2}\beta\delta_i + 1) \tag{13}$$

where the term k_i depends on the geometry and material of the ball and races. Similarly, the contact force between the outer race and the *j*th ball is

$$Q_{e_j} = k_e\delta_e^{\frac{3}{2}}(\frac{3}{2}\beta\delta_e + 1) \tag{14}$$

The equation of motion of the bearing inner race is

$$\begin{bmatrix} 2m_{bi} & 0 & 0 \\ 0 & 2m_{bi} & 0 \\ 0 & 0 & 2m_{bi} \end{bmatrix}\begin{bmatrix} \ddot{x}_{bi} \\ \ddot{y}_{bi} \\ \ddot{z}_{bi} \end{bmatrix} = \begin{bmatrix} F_x \\ F_{ky} \\ F_{kz} \end{bmatrix} + \sum_{j=1}^{n}(T_j^{-1}\begin{bmatrix} Q_{ex_j} \\ Q_{ey_j} \\ Q_{ez_j} \end{bmatrix}) \tag{15}$$

where F_x , F_{ky} *and* F_{kz} are contact forces between the rotor and the inner race, which will be explained in the later section; where Q_{ix_j} , Q_{iy_j} , Q_{iz_j} are projections of contact forces from bearing inner race in global x, y and z directions.

The equation of motion of the outer race is

$$\begin{bmatrix} 2m_{bo} & 0 & 0 \\ 0 & 2m_{bo} & 0 \\ 0 & 0 & 2m_{bo} \end{bmatrix} \begin{bmatrix} \ddot{x}_{bo} \\ \ddot{y}_{bo} \\ \ddot{z}_{bo} \end{bmatrix} = \sum_{j=1}^{n} (T_j^{-1} \begin{bmatrix} Q_{ex_j} \\ Q_{ey_j} \\ Q_{ez_j} \end{bmatrix}) + \begin{bmatrix} F_{stiffx} + F_{dampingx} \\ F_{stiffy} + F_{dampingy} \\ F_{stiffz} + F_{dampingz} \end{bmatrix} \tag{16}$$

The equation of motion for the jth ball is

$$\begin{bmatrix} m_b & 0 & 0 \\ 0 & m_b & 0 \\ 0 & 0 & m_b \end{bmatrix} \begin{bmatrix} \ddot{x}_{b_j} \\ \ddot{y}_{b_j} \\ \ddot{z}_{b_j} \end{bmatrix} = T_j^{-1} \begin{bmatrix} Q_{ix_j} - Q_{ex_j} \\ Q_{iy_j} - Q_{ey_j} \\ Q_{iz_j} - Q_{ez_j} \end{bmatrix} - T_j^{-1} \begin{bmatrix} 0 \\ 0 \\ F_{c_j} \end{bmatrix} \tag{17}$$

where F_{c_j} is the centrifugal force for the *j*th ball.

2.2 Rotor – AB Contact Model

As shown in Figure 7, assume that the rotor node number at the AB location is k.

The contact forces acting on the rotor due to AB inner race contact are

$$F_{ky} = -F_{Nk} \cos\alpha_i + F_{tk} \sin\alpha_k \tag{18}$$

$$F_{ky} = -F_{Nk} \cos\alpha_k + F_{tk} \sin\alpha_i \tag{19}$$

$$F_{kz} = -F_{Nk} \sin\alpha_k - F_{tk} \cos\alpha_k \tag{20}$$

$$T_{\theta_x k} = -R_{rk} F_{tk} \tag{21}$$

The force between the rotor and the AB inner race is treated as a Hertzian line contact [5]

$$F_{Nk} = K_l \delta^{\frac{10}{9}} (1 + \frac{3}{2} \beta \dot{\delta}) \tag{22}$$

where K_l can be calculated from [5] as

$$K_l = \frac{0.39^{\frac{10}{9}}}{l} (\frac{4(1-v_1^2)}{E_1} + \frac{4(1-v_2^2)}{E_2}) \tag{23}$$

The friction force between the AB inner race and the rotor becomes

$$F_{tk} = \begin{cases} \mu_r F_{rk}, & (v_{rel} > 0) \\ F_{rll}, & (v_{rel} = 0) \\ -\mu_r F_{rk}, & (v_{rel} < 0) \end{cases} \tag{24}$$

A Stribeck friction model is employed where

$$\mu_r = -\frac{2}{\pi} \arctan(\varepsilon_f v_{rel}) [\frac{\mu_s - \mu_d}{1 + \delta_f |v_{rel}|} + \mu_d] \tag{25}$$

$$F_{tk} = -\mu_r F_{Nk}, \quad V_{rel} \neq 0 \tag{26}$$

where ε_f determines the steepness of the approximation function, δ_f is a positive number that determines the rate at which the static friction coefficient approaches the dynamic friction coefficient with respect to relative velocity. The term " $-\frac{2}{\pi} \arctan(\varepsilon_f vel_{rel})$ " has a similar function to the "sign" function, but provides improved numerical stability of the system simulation and agrees well with experimental data for

predicting the static friction force according to [17]. The relative tangential velocity of the contact point P, v_{rel}, on the rotor as shown in Figure 7 is

$$v_{rel} = -\dot{y}_i \sin\alpha_i + \dot{z}_i \cos\alpha_i + R_r\dot{\theta}_{xi} - (-\dot{y}_{bi} \sin\alpha_i + \dot{z}_i \cos\alpha_i + (R_{bi} + \Delta_{ri} - cr)\dot{\theta}_{bxi}) \qquad (27)$$

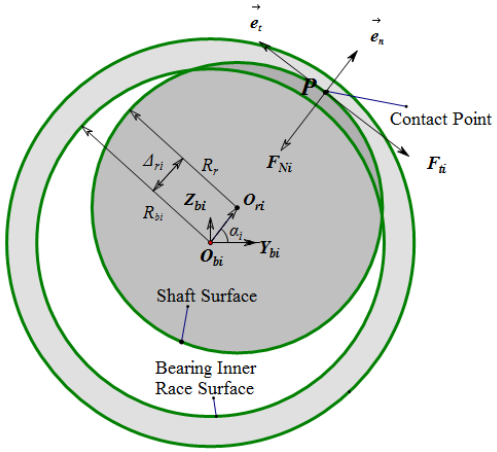

Figure 7. Contact between the rotor and the auxiliary bearing inner race

The Stribeck friction factor model provides a smooth transition between static and sliding friction and is plotted vs. the relative tangential velocity in Figure 8. The parameter values utilized in Figure 8 are ε_f =10000, δ_f =1, μ_s = 0.2 and μ_d = 0.15.

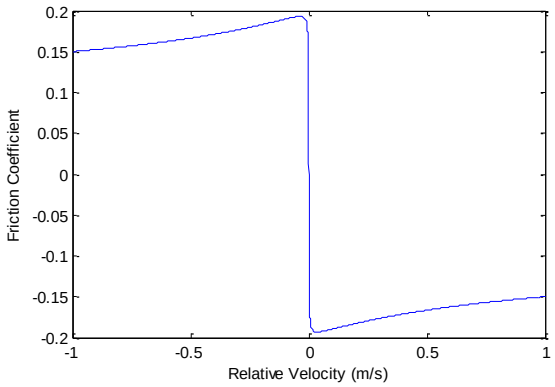

Figure 8 Stribeck model friction coefficient vs. tangential relative velocity

The rotor is modeled with Timoshenko beam finite elements and has the general form

$$M\ddot{X} + [C + \Omega G]\dot{X} + KX = F \tag{28}$$

where M , C , G and K are the mass, damping, gyroscopic and stiffness matrices of the rotor and Ω is its angular velocity. The vector X contains the nodal degree of freedom of the rotor and F is the load vector including the weight, mass imbalance forces and the nonlinear auxiliary bearing contact forces and torques. Each beam node has four degrees of freedom, including two translations, and two rotations. A fourth order Runge-Kutta numerical integration method is used to solve (43) given initial conditions.

2.3 AB Thermal Model

Large amounts of heat may be generated due to friction after the rotor drops onto the AB. This can cause thermal expansion of the bearing inner race, balls, and outer race. Such a process can increase the preload of the bearing and consequently generate more heat, possibly leading to a "thermal runaway" condition. There are four major heat sources that occur when the rotor drops onto the auxiliary bearing:

1) Friction torque due to the external steady loads
2) Viscous friction torque
3) Friction between the rotor and the AB inner race

Heat source (1) results from friction between the ball bearing's components which can be calculated by the drag torque formula

$$T_{dl} = f_1 F_\beta d_m \tag{29}$$

The corresponding thermal power loss is

$$H_p = T_{dl}\, \omega_i \tag{30}$$

where ω_i is the rotational speed of the bearing inner race. Heat source (2) is caused by the friction among bearing components and the lubricant and is expressed by

$$H_v = T_{dv} \omega_i \tag{31}$$

The third heat source is the sliding friction between the shaft surface and the bearing inner race

$$H_s = F_t v_{rel} \tag{32}$$

The heat flux is assumed to be uniformly distributed in the radial direction and is symmetric in the axial direction. This permits use of a computationally efficient one-dimensional, lumped thermal mass, radial heat transfer equation. Thermal resistances are included to account for heat conduction between the lumped thermal masses. Further assumptions for the thermal bearing model include

a) Heat sources are located on the balls, the inner race and outer race.

b) Heat sources are shared evenly between components if occurring at a contact point between the 2 components

c) The ball bearing is modeled with lumped thermal masses

d) Each lumped thermal mass has a uniform temperature

The thermal resistances, which are determined by the geometry and material of each component, are calculated as shown in Table 1.

Table 1 Thermal resistance of heat transfer network

Ball/lubricant	**Inner race/Shaft**	**Outer race**
$R_{Li} \cong \frac{r_b}{k_l(2\pi r_i W_i - \pi n r_b^2)}$	$R_i = \frac{\ln(r_i/r_s)}{2\pi k_i W_i}$	$R_e = \frac{\ln(r_o/r_e)}{2\pi k_e W_e}$
$R_{Le} \cong \frac{r_b}{k_l(2\pi r_e W_e - \pi n r_b^2)}$	$R_i = \frac{1}{\pi k_s W_i}$	$R_h = \frac{R_{hr}R_{ha}}{R_{hr}+R_{ha}}$
$R_b \cong \frac{r_b}{n k_b \pi r_b}$	$R_{sa} = \frac{L_s}{k_s \pi r_s^2} + \frac{1}{h_s \pi r_s^2}$	
Housing	$R_1 = \frac{R_{Le}R_b/2}{R_{Le}+R_b/2}$	$R_2 = \frac{R_{Li}R_b/2}{R_{Li}+R_b/2}$
$R_{hr} = \frac{\ln(r_h/r_o)}{2\pi k_h L_h} + \frac{1}{h_h 2\pi r_h L_h}$		
$R_{ha} = \frac{L_h}{2\pi k_h (r_h^2 - r_o^2)} + \frac{1}{h_h \pi (r_h^2 - r_o^2)}$		

The differential equation of the AB heat transfer model is

$$M_c \dot{T}_c = A_c T_c + H \tag{33}$$

where M_c is the thermal mass matrix, T_c is the nodal temperature vector, A_c is the matrix of thermal resistances, and H is the heat source vector. The thermal expansion of the auxiliary bearing system is included in the AB model based on reference [5]. The radial thermal expansion of the bearing outer race is

$$\varepsilon_e = \frac{\xi_e}{3}\frac{(1+\upsilon_e)r_e}{r_e + r_h}[\Delta T_{Le}(2r_e + r_h) + \Delta T_h(2r_h + r_e)] \tag{34}$$

The radial thermal expansion of the bearing inner race is

$$\varepsilon_i = \frac{\xi_i}{3}(1+\upsilon_i)r_i[\Delta T_s + \Delta T_{Li}] \tag{35}$$

The radial thermal expansion of the bearing balls is

$$\varepsilon_b = \xi_b r_b \Delta T_b \tag{36}$$

2.4 AB life prediction

A possible fatigue failure mechanism for a rolling element bearing is excessive orthogonal shear stress τ_o occurring at a location slightly below a surface that is subjected to a concentrated, perpendicular contact force. This stress is given by

$$\frac{2\tau_0}{\sigma_{\max}} = \frac{\sqrt{2(t-1)}}{t(t+1)} \tag{37}$$

Where t is an auxiliary parameter determined by elliptic contact region as shown in Figure 9.

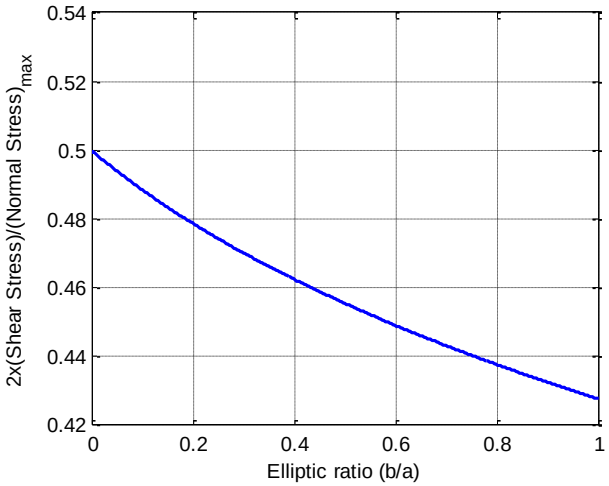

Figure 9. Sub-surface shear stress ratio $\tau_0/\sigma_{\max}$ vs. ellipse axis ratio

The $\sigma_{\max}$ is defined by:

$$\sigma_{\max} = -\frac{3Q}{2\pi ab} \tag{38}$$

where Q is the load between inner race and ball or outer race and ball, a, b are semimajor and semiminor axis of the projected elliptical area. They can be calculated by Hertzian contact theory.

$$\frac{b}{a} = \sqrt{(t^2-1)(2t-1)} \tag{39}$$

Additionally, surface shear stress also contributes much for the fatigue failure of the AB. It is

$$\tau_{surface} = \mu\sigma \tag{40}$$

where μ is the friction coefficient between ball and races and σ is the normal stress. The value of μ is typically 0-0.2, here it set to be 0.2. to [5].

Based on the simulation, the contact stresses on the AB inner race IR are larger than that on the AB outer race. Therefore, here we use the fatigue life of the AB inner race to represent the fatigue life of the AB. To accurately obtain the AB inner race's fatigue life, the AB inner race is separated into several segments in circumferential direction, then the fatigue life of each segment will be calculated and the lowest one will be the fatigue life of the AB inner race. When calculating the shear stress of each segment, the stress is directly obtained from the contact stress between the ABIR and each bearing ball. There is an assumption that the contact stresses acting on each segment are assumed to act on the center point of the segment. The results can be less conservative when the segment number is increased.

Here let θ_{ABIR} be the rotated angle of the ABIR， θ_i be the initial circumferential location of the center point of each segment. n_{seg} to be the total segment number. α_{cage} is the rotated angle of the AB cage, α_j is the initial circumferential location of the jth ball. F_{segi} to be the contact force on the center point of each segment of the ABIR. F_{ballj} to be the contact force between the jth ball and the ABIR. Therefore, the contact force of each segment can be determined as follow:

$$F_{segi} = \begin{cases} F_{ballj}, & if \quad abs(\theta_{ABIR} + \theta_i - \alpha_{cage} - \alpha_j) \le \dfrac{2\pi}{2n_{seg}} \\ 0 & if \quad abs(\theta_{ABIR} + \theta_i - \alpha_{cage} - \alpha_j) \ge \dfrac{2\pi}{2n_{seg}} \end{cases} \tag{41}$$

As described in reference [18], fatigue damage under rolling contact conditions is caused purely by the action of shear stresses, with the mechanism of failure similar to the

torsional fatigue. Therefore, both of the relationship between fatigue cycles and the shear forces are based on the torsional fatigue test data.

The Rainflow counting method is applied to calculate the fatigue life of the auxiliary bearing as presented in reference [5]. The cumulative damage D and number of cycles N to failure are determined using a histogram of cycle ranges and Miner's rule

$$D = \frac{n_1}{N_1} + \frac{n_2}{N_2} + ... = \sum_i \frac{n_i}{N_i} \geq 1 \tag{42}$$

where n_i is the number of applied cycles and N_i is the number of cycles to failure at a certain stress amplitude τ_i. The critical cumulative damage value of D is chosen to be 1. AB life is estimated from

$$life = \frac{1}{\sum_i \frac{n_i}{N_i}} \tag{43}$$

2.5 Transient response of a rotor drop onto a ball bearing type auxiliary bearing

A sample case of a rotor dropping onto a ball bearing type auxiliary bearing with fixed inner race is done here to show the performance of the rotor-auxiliary bearing model. The rotor model is shown in Figure 10.

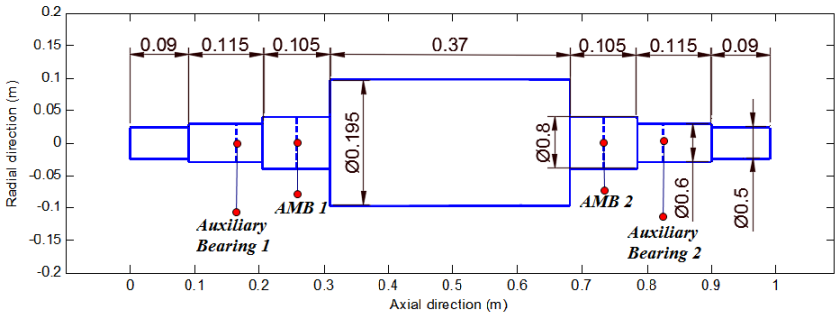

Figure 10 Geometry of the example rotor and finite element mesh (dashed)

The general information of the simulation case is shown in Table 2.

Table 2 General Information for the Simulation Case

Rotor drop spin speed	20,000RPM
Dynamic friction coefficient	0.35
Static friction coefficient	0.45
Air gap	0.3mm
Bearing bore diameter	80.0mm
Bearing outer diameter	125.00mm
Bearing width	22.0mm
Pitch diameter	110.mm
Ball diameter	19.05mm
Number of balls	10
Ambient temperature	25^{o}C
Number of ABIR segments for the fatigue life calculation	100

A grid independent study is performed to determine the number of beam elements required for the rotor modeling to accurately obtain the rotor drop transient response. The maximum normal contact forces and maximum rotor radial penetrations during the first impact when using different number of elements of the rotor are compared, which are shown from Figure 12 to Figure 13.

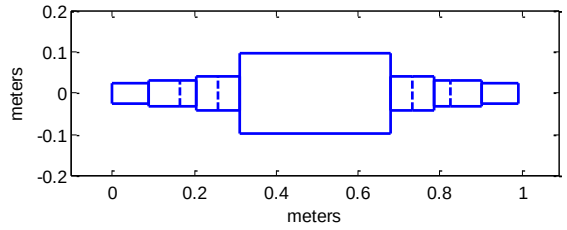

(a) 11 elements

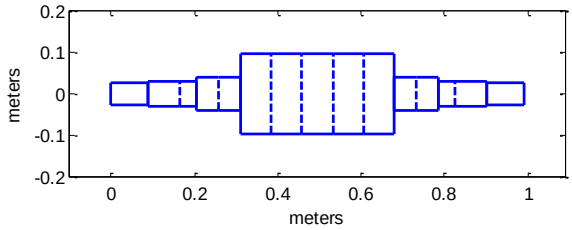

(b) 15 elements

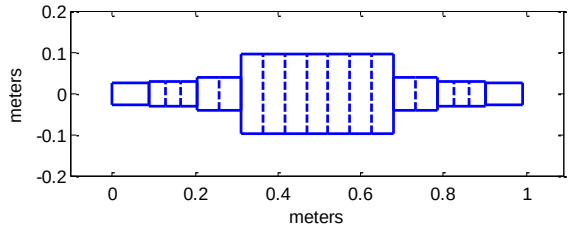

(c) 19 elements

Figure 11 Rotor with different finite element meshes

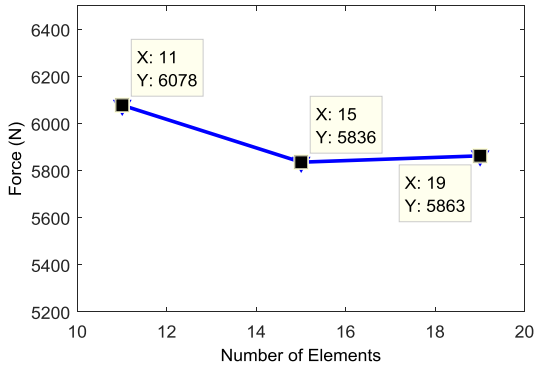

Figure 12. Maximum normal contact forces during the first contact with different number of elements

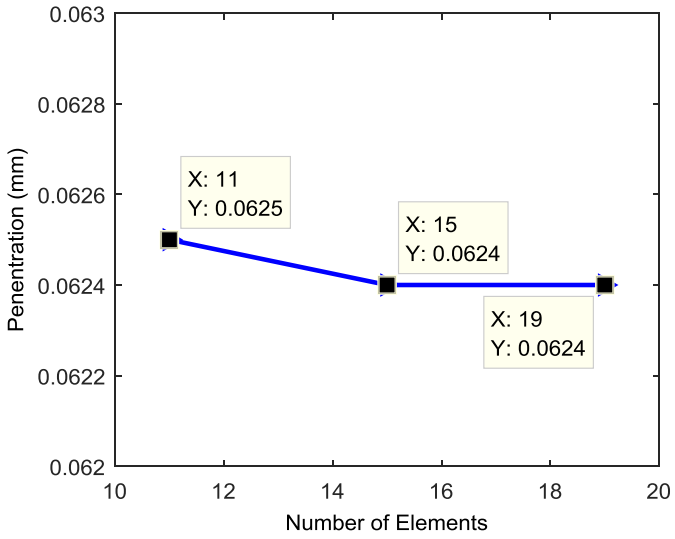

Figure 13. Maximum radial penetration during the first contact with different number of elements

It can be seen that there are 3.6% differences between the contact forces of the 11 elements model and the 19 elements model and 0.16% differences for the penetration, but the calculation time will be greatly reduced when using the 11 element model. Hence, the 11 elements model is selected for the parametric studies in this and the other chapters.

As shown in Table 2, the rotor drop rotational speed is 20,000 RPM. Figure 14 shows the linearized ball bearing stiffness with different rotor's rotational speed. It can be seen that under 20,000RPM, the stiffness of the ball bearing is $2.046\times10^{8}\,N/m$.

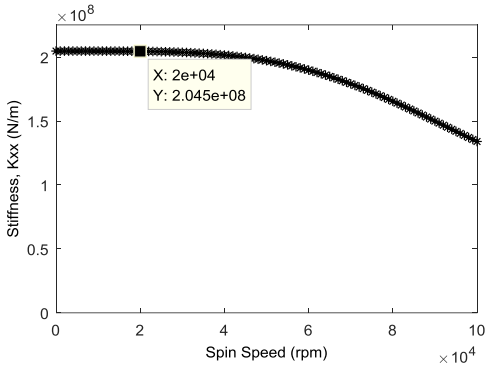

Figure 14. Ball bearing stiffness vs. spin speed

The rotor orbit during rotor drop is shown in Figure 15.

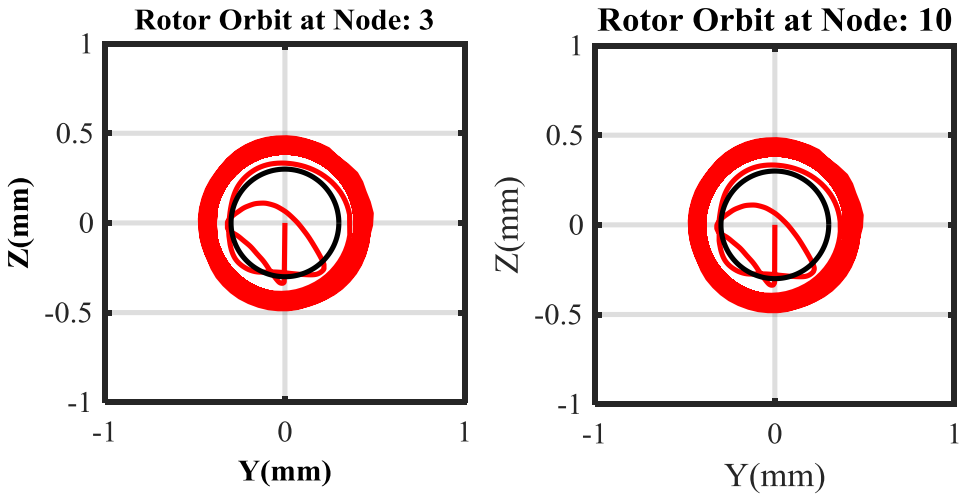

(a) Left AB (b) Right AB

Figure 15 Rotor orbit when the rotor drops onto the AB

It can be seen that when the dynamic friction coefficient reaches 0.35, the reverse whirl occurs, from Figure 16, the whirl frequency of the rotor reaches around 250Hz.

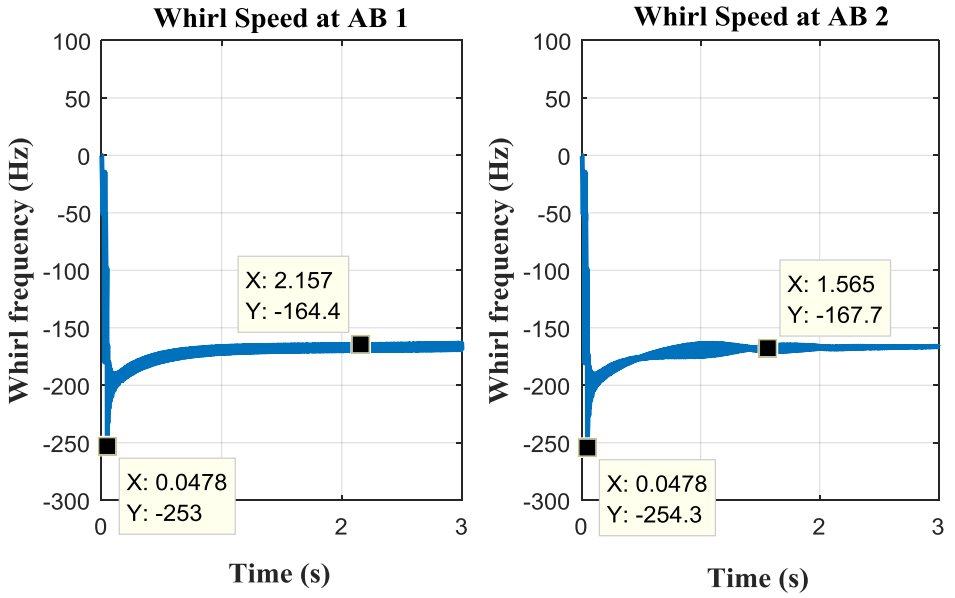

(a) Left AB (b) Right AB

Figure 16. Whirl frequency of the rotor

When the reverse whirl occurs, due to the induced centrifugal force, the contact forces are much larger than the forces caused by the first a few impacts.

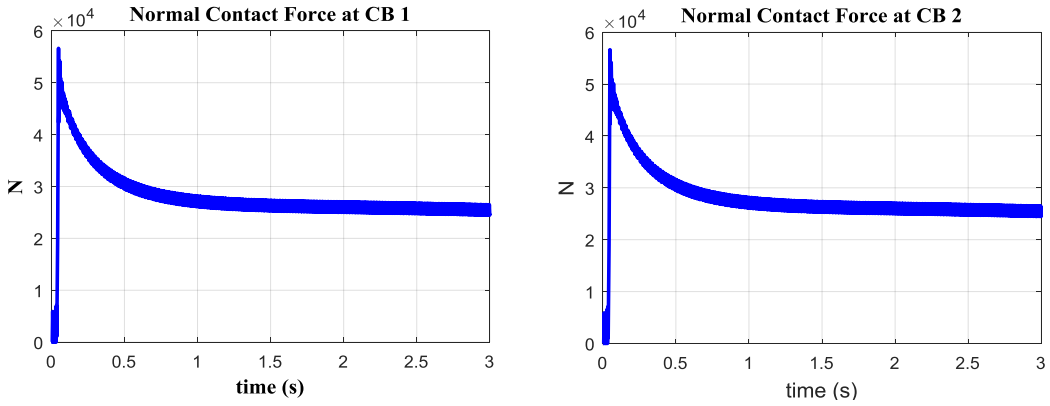

(a) Left AB (b) Right AB

Figure 17 Normal contact force between the rotor and the AB

From Figure 18, it can be seen that it takes about 0.0461s to let the ABIR reaches the similar rotational speed as the rotor. The spin speed of the ABIR is slightly smaller than that of the rotor. It is because the radius of the ABIR is a little bit larger.

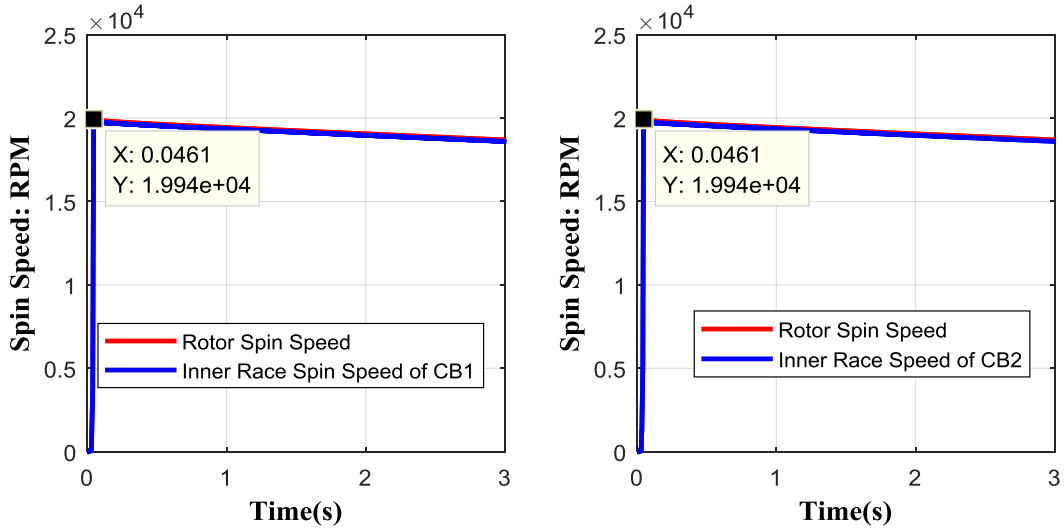

(a) Left AB (b) Right AB

Figure 18 Rotor spin speed between the rotor and the AB

Figure 19 shows the temperature variation of the AB during rotor drops. It can be seen that the temperature of the bearing ball is the highest among the AB components. That is because it has relatively small thermal mass. Additionally, due to the high rotational speed of the rotor and the reverse whirl, the temperature of the AB ball increases from 25^{o}C to 135.6^{o}C in just 3 seconds, which will cause large thermal expansion and results in larger stresses between the balls and the AB races.

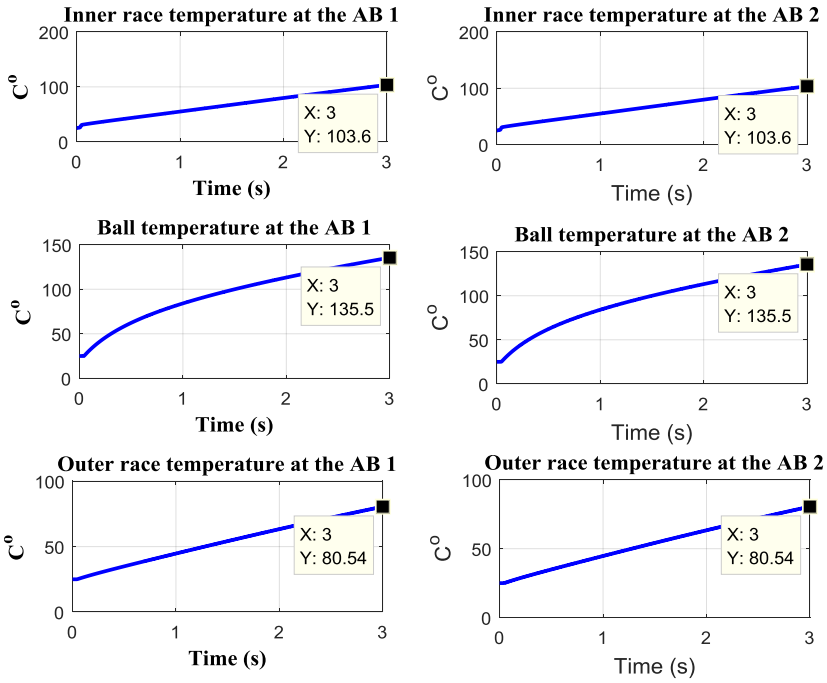

(a) Left AB (b) Right AB

Figure 19 Temperature variation on the Abs

The maximum shear stresses at each time step from the bearing balls on bearing races are shown in Figure 20. It can be seen that the shear stress on the inner race are larger than that on the outer race, which is caused by the different curvatures of the AB inner and outer races. Therefore, as mentioned in the section 2.4, the fatigue life of the AB inner race is used to represent the fatigue life of the AB.

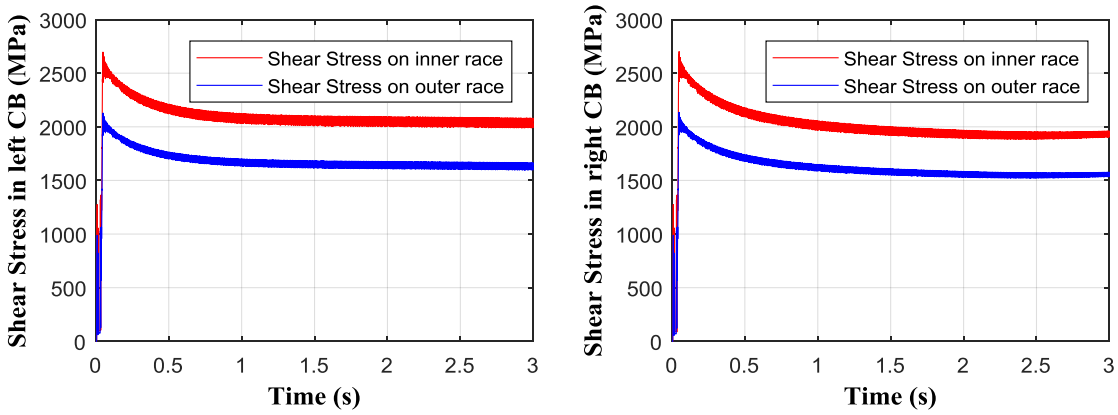

(a) Left AB (b) Right AB

Figure 20 Maximum shear stresses at each time step between the bearing balls and races

The shear stresses on each AB inner race's segments are also recorded to calculate the fatigue life of each segment. Figure 21 shows the shear stress of the segment with the lowest fatigue life. It can be seen unlike the stresses in Figure 20, the stresses on the segment are discrete value. Only when a ball passes, the segment will suffer the stress.

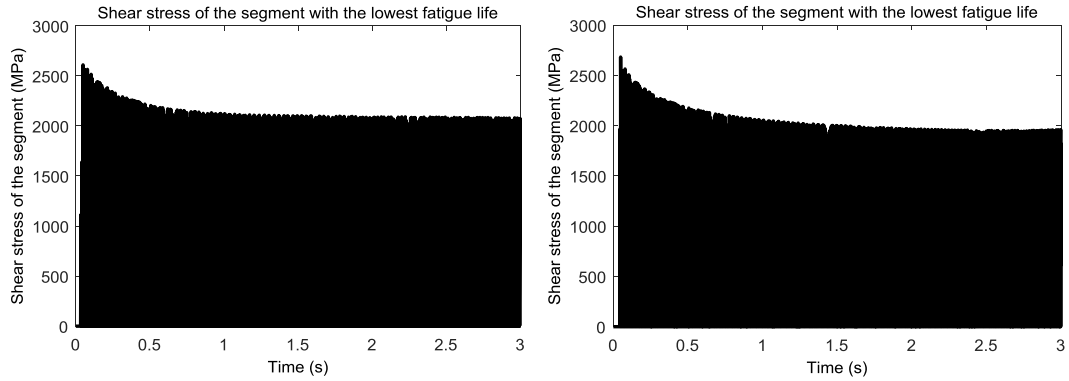

(a) Left AB (b) Right AB

Figure 21 Shear stress of the segment with the lowest fatigue life

The stress cycles are counted based on the rain flow counting method, the stress with the highest number of cycles is about 2100MPa, the highest stress counted is about 2500MPa, which is same as what is shown in Figure 21.

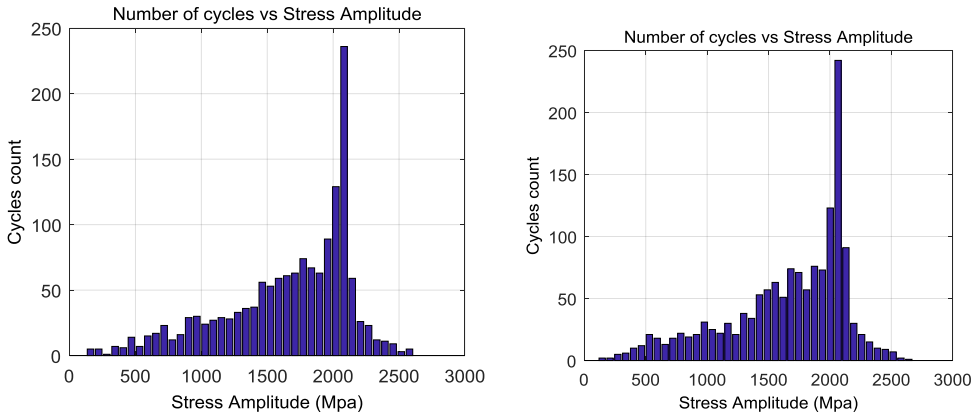

(a) Left AB (b) Right AB

Figure 22 Stress cycles of the segment with the lowest fatigue life

Based on the SN curve and the Miner's rule introduced in the section 2.4, the fatigue lives of the each segment are obtained as shown in Figure 23. It can be seen that the fatigue lives of each segment are in the range between 2 to 5. The results show the AB can only suffer 2 times of drops in this case.

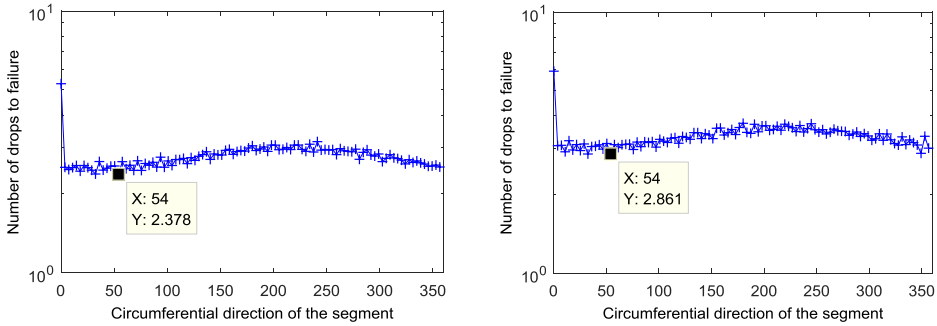

(a) Left AB (b) Right AB

Figure 23 Stress cycles of the segment with the lowest fatigue life

2.6 Conclusion

This part introduces a high fidelity elastic-thermal coupled rotor-auxiliary bearing model and its life prediction. A sample case with reverse whirl is showed to provide an intuitive view of the rotor drop phenomenon. Additionally, this part lays the foundation of the auxiliary bearing damper model development in the following chapters.

CHAPTER III

HIGH FIDELITY GROOVED SQUEEZE FILM DAMPER MODEL CONSIDERING THE TEMPORAL FLUID INERTIA EFFECT

This chapter utilizes a finite element (FEM) solution of Reynold's equation including the inertia force term to model a SFD with a center groove as shown in Figure 1, which is similar with the linear bulk-flow model in [7]. As a preliminary benchmark the SFD force coefficients including the damping and the added mass are correlated with [7]. The SFD model is integrated into the high fidelity nonlinear structural and thermal auxiliary bearing rotor drop model. Hertzian contact forces are applied between each bearing component, including the inner race, outer race, and each ball, in the auxiliary bearing model. Temperature variations and thermal expansions of each bearing component are included in the AB model. The rotor vibration is modeled with Timoshenko beam elements. A transient structural and thermal dynamics simulation of the AB and rotor is conducted for the case of the high speed rotor dropping onto the ball bearing type AB through a clearance space. The AB is supported by a center grooved, squeeze film damper. The fatigue life of the AB is calculated by considering the resulting race stresses and using a rain flow counting method, Lee at al. [5]

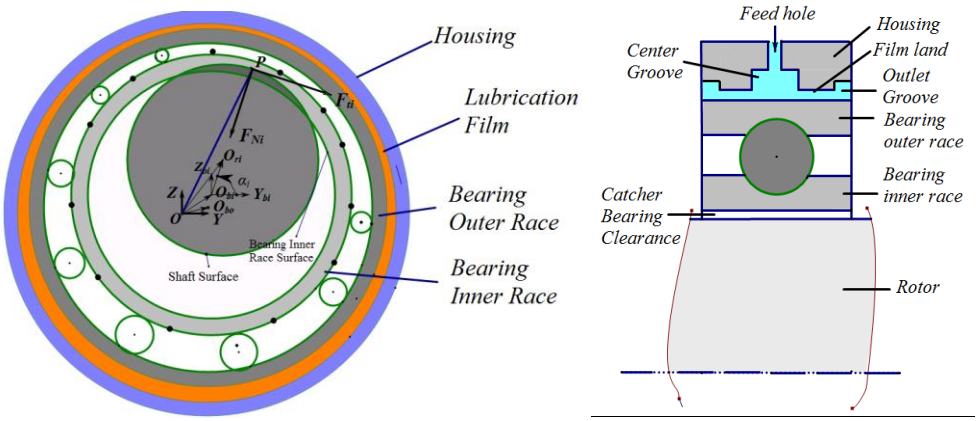

a. Front view b. Cross view

Figure 24. Central Groove SFD integrated into an auxiliary bearing system

This chapter investigates the influence of the added mass and the clearances of the SFD on the rotor drop behavior and provides guidelines for the SFD design in an AB application.

3.1 Center Groove SFD Model

The pressure distribution in the SFD is obtained utilizing a finite element based solution of Reynold's equation using an effective clearance for the groove region, Delgado [7].

The Reynolds equation for the film pressure of an incompressible fluid considering the temporal fluid inertia is

$$\frac{\partial}{\partial x}\left(\frac{h_i^3}{12\mu}\frac{\partial P}{\partial x}\right)+\frac{\partial}{\partial z}\left(\frac{h_i^3}{12\mu}\frac{\partial P}{\partial z}\right)=\frac{\partial h_i}{\partial t}+\frac{R\Omega}{2}\frac{\partial h_i}{\partial x}+\frac{(\rho h_i^2)}{12\mu}\frac{\partial^2 h_i}{\partial t^2} \tag{44}$$

where h_i represents the clearance in the i^{th} section and the term $\frac{R\Omega}{2}\frac{\partial h}{\partial x}$ is zero since the rotational speed of the SFD inner race is zero. The pressure interpolation is

$$p(x,y)=\underline{N}^T\underline{p}_e \tag{45}$$

A linear triangular element is utilized so the shape function and nodal pressure vectors are

$$\underline{N}^T = (N_1 \quad N_2 \quad N_3) \tag{46}$$

$$\underline{P}_e^T = (P_{1e} \quad P_{2e} \quad P_{3e}) \tag{47}$$

Then, the Reynolds equation has the element level form

$$\underline{K}_e \underline{P}_e = \underline{S}_e + \underline{L}_e + \underline{I}_e \tag{48}$$

where

$$(K_e)_{ij} = (\frac{h_e^3}{12\mu}) \int_\Omega (\frac{\partial N_i}{\partial x}\frac{\partial N_j}{\partial x} + \frac{\partial N_i}{\partial y}\frac{\partial N_j}{\partial y}) dxdy \quad i=1,2,3 \; ; \; j=1,2,3 \tag{49}$$

and S_e represents the damping source term

$$(S_e)_i = -\frac{\partial h}{\partial t} * \int_\Omega N_i dxdy \tag{50}$$

The term I_e represents the fluid inertia:

$$(I_e)_i = -[\frac{(\rho h^2)}{12\mu}\frac{\partial^2 h}{\partial t^2}]_e * \int_\Omega N_i dxdy \tag{51}$$

The mesh of the SFD with central groove is shown in 2.

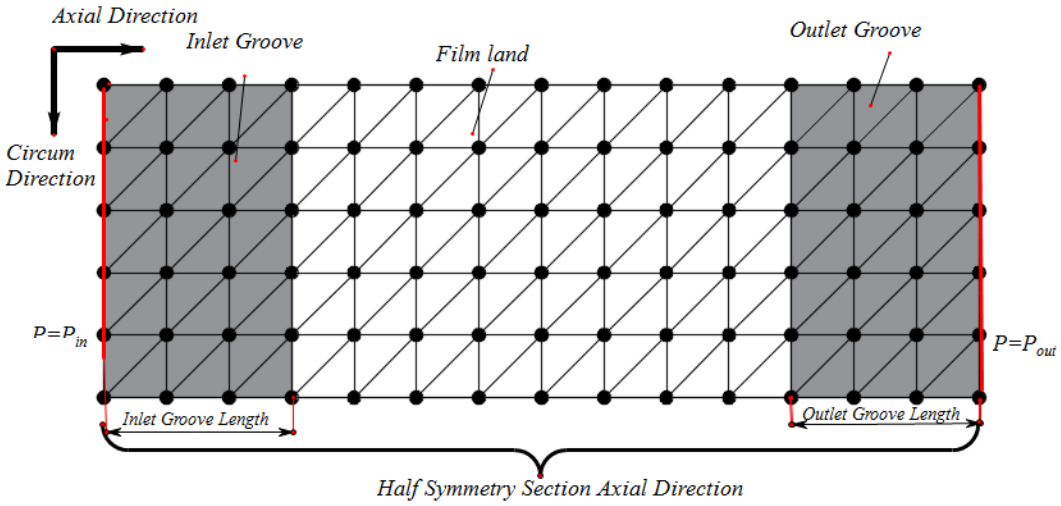

Figure 25. Element mesh and boundary condition of the grooved SFD

A preliminary benchmark case was performed to insure the accuracy of the isolated SFD component model prior to including it in the overall rotor/AB/SFD system model. The benchmark compared the present SFD model results to those of Delgado's end sealed SFD [7] . The parameters of the end seal SFD in [7] are shown in Table 3. The geometry is shown in Figure 26.

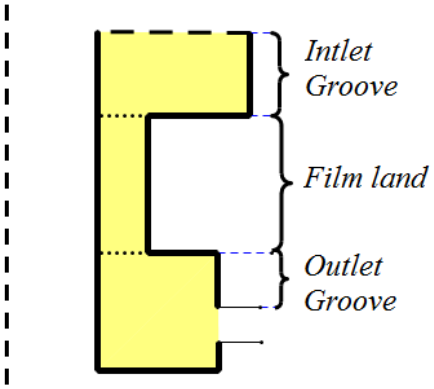

Figure 26. Geometry of the flow region

Table 3. SFD parameters in **[7]**

Radial Clearance in Damper	0.127mm
Whirl Frequency	50 Hz
Damper Diameter	127mm
Whirl Orbit radius	12μm
Absolute Viscosity	2.8-3.1cp
Inlet Groove Length	6.36 mm
Discharge Groove Length	4.1mm
Land Length	25.4mm

The damping coefficient and added mass of the SFD are calculated with different effective clearance ratios of the groove in Figure 27. The results are compared with the results from [7] linear bulk flow model, and show good agreement with a difference of less than 5%.

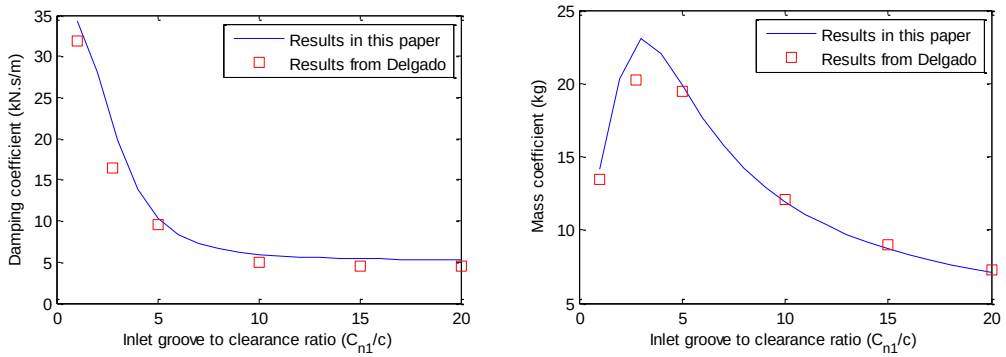

a. Damping coefficient b. Added Mass

Figure 27. Damping coefficient and added mass for different clearance ratios

3.2 Combined AB and Grooved SFD Sub-System

Figure 24 illustrates a rolling element AB with a central groove, open ended SFD. The AB outer race (ABOR) motion relative to the housing in Figure 1 can be relatively large with respect to the clearance, and vary in a transient (non-periodic) manner due to impact or very high intermittent loading. This precludes use of a linear dynamic coefficient model of the SFD forces, and instead requires solution of Reynold's equation for the pressure distribution and resultant forces at each time step in the numerical integration. Inspection of the right hand side of equation (10) shows that the instantaneous forces are attributable to a ABOR damping (velocity) and an ABOR inertia (acceleration) source term hence the total force may be represented as

$$F_{SFD} = F_{Inertia} + F_{Damping} \tag{52}$$

where $F_{Damping}$ is the SFD reaction force caused by the squeeze (velocity) effect and $F_{Inertia}$ is the reaction force only caused by the inertia (acceleration) effect. The inertia $F_{Inertia}$ is proportional to the acceleration of the ABOR, therefore

$$F_{Inertia} = \Lambda\, a_{\mathbf{CBOR}} \tag{53}$$

where Λ is an added mass type term. Note that by (1) Λ varies with the instantaneous film thickness and therefore varies with time, i.e. $\Lambda(t)$ .The equation of motion of the ABOR is

$$\begin{bmatrix} M_{OR} & \\ & M_{OR} \end{bmatrix} \begin{bmatrix} \ddot{y} \\ \ddot{z} \end{bmatrix} = \begin{bmatrix} F_{stiffy} + F_{bally} + F_{dampingy} \\ F_{stiffz} + F_{ballz} + F_{dampingz} \end{bmatrix} + \begin{bmatrix} \Lambda_{yy} & \Lambda_{yz} \\ \Lambda_{zy} & \Lambda_{zz} \end{bmatrix} \begin{bmatrix} \ddot{y} \\ \ddot{z} \end{bmatrix} \tag{54}$$

where F_{stiffy} represents the force acted by the supporting device of the SFD, F_{bally} represents the summation of the forces acted by all the bearing balls, $F_{dampingx}$ is the force purely caused by the damping of the SFD, and Λ_{yy}, etc. are the transient added mass terms. Moving the added mass terms to the left side of the equation (16) forms equation (55), which does not have acceleration terms on its right hand side.

$$\begin{bmatrix} M_{OR}-\Lambda_{yy} & -\Lambda_{yz} \\ -\Lambda_{zy} & M_{OR}-\Lambda_{zz} \end{bmatrix} \begin{bmatrix} \ddot{y} \\ \ddot{z} \end{bmatrix} = \begin{bmatrix} F_{stiffy}+F_{bally}+F_{dampingy} \\ F_{stiffz}+F_{ballz}+F_{dampingz} \end{bmatrix} \tag{55}$$

3.3 Numerical Example: SFD Benefits

This section provides a numerical example to illustrate the preceding analysis and demonstrate the benefits of installing a central groove SFD into the AB system. The SFD model includes fluid inertia effects and utilizes a FEM model of the oil film to calculate the instantaneous forces exerted on the AB housing by the SFD. These forces are utilized in a nonlinear, transient, numerical integration of the system equations of motion.

The nonlinear elastic-thermal coupled ball bearing type auxiliary bearing model is used, which is descripted in chapter 2. A linearized bearing stiffness vs. bearing rotational speed is provided as shown in Figure 14. The only difference is that a damper model is integrated into the AB heat transfer network as shown in Figure 28. The thermal resistance of the squeeze film damper is

$$R_{SFD} = \frac{\ln((r_{sfd}+c_{film})/r_{sfd})}{2\pi k_{sfd} L_{film}} + \frac{\ln((r_{sfd}+c_{groove})/r_{sfd})}{2\pi k_{sfd} L_{groove}} \tag{56}$$

where r_{sfd} is the inner radius of the squeeze film damper, c_{film} is the clearance of the film land, c_{groove} is the clearance of the groove land, k_{sfd} is the thermal conductivity of the fluid film, L_{film} is the length of the film length, L_{groove} is the length of the groove land. Because of the relatively small motion and the low surface velocity on the SFD journal, the heat generated in the SFD is ignored.

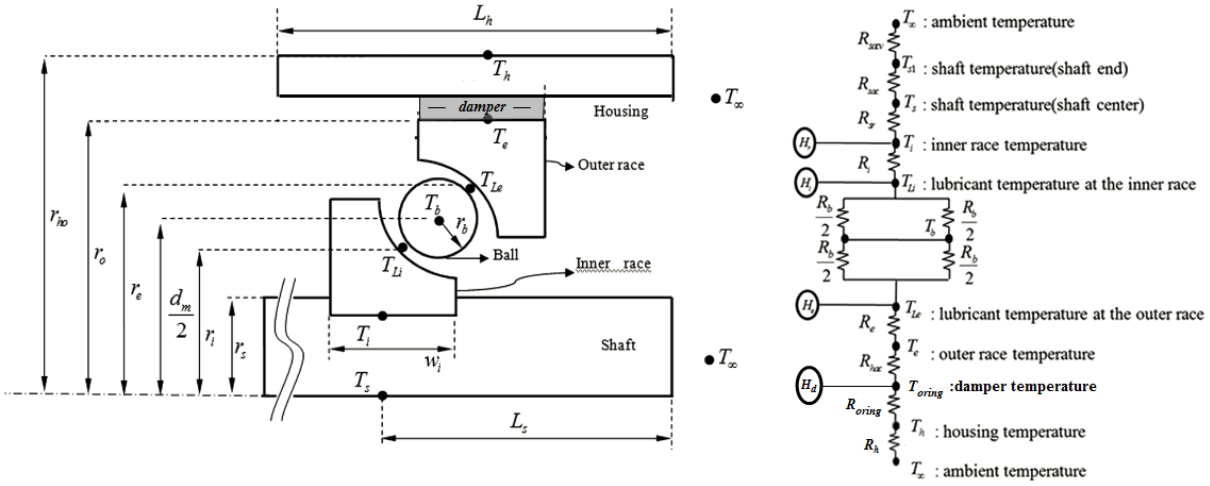

Figure 28. Heat transfer model for AB

Table 5 provides the parameter values for the SFD. The SFD is supported on an anti-rotation spring (squirrel cage) which also provides a radial stiffness of 5e8N/m. All drop tests occur at a rotational speed of 20,000 rpm. By comparison the critical speed of the rotor supported by the squirrel cage stiffness is 1,1690 rpm. The AB clearance for the example is 0.3 mm. The detail simulation parameters about the rotor and the auxiliary bearing are shown in Table 4.The parameters about the squeeze film damper is shown in Table 5.

Table 4 General Information for the Simulation Case

Rotor drop spin speed	20,000RPM
Dynamic friction coefficient	0.35
Static friction coefficient	0.45
Air gap	0.3mm
Bearing bore diameter	80.0mm
Bearing outer diameter	125.00mm
Bearing width	22.0mm
Pitch diameter	110.mm
Ball diameter	19.05mm
Number of balls	10
Ambient temperature	25^{o}C
Number of ABIR segments for the fatigue life calculation	100

Simulations are performed with the AB outer raced fixed, and with it flexibly mounted on a SFD, in order to demonstrate the benefit of the SFD on force and vibration reduction and extension of AB life. A third AB support case is also presented: a soft mounted AB supported by the same squirrel cage stiffness as with the SFD but without the SFD oil film.

Table 5. Squeeze film damper parameters

Radial clearance in damper (mm)	0.254
Absolute viscosity (kg/s)	3.1522kg/s
Damper diameter (mm)	127
Damper total length / damper diameter	0.5
Inlet groove length (mm)	12.7
Fluid density (kg/m^3)	785
Effective groove clearance/film clearance	20

The friction coefficient between the rotor and the AB inner race is 0.35, since this value precipitates backward whirl, and therefore provides a vibration control challenge for the SFD. Figure 29 shows the geometry of the example rotor with the Auxiliary bearing locations.

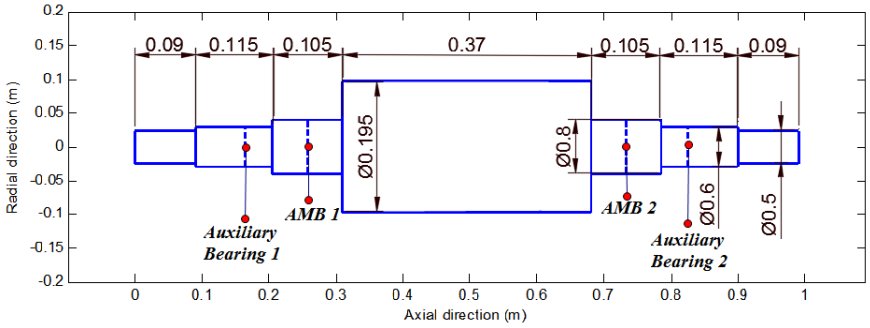

Figure 29. Geometry of the example rotor and FE mesh (dashed)

Rotor orbits with and without the SFD are shown in Figure 30.

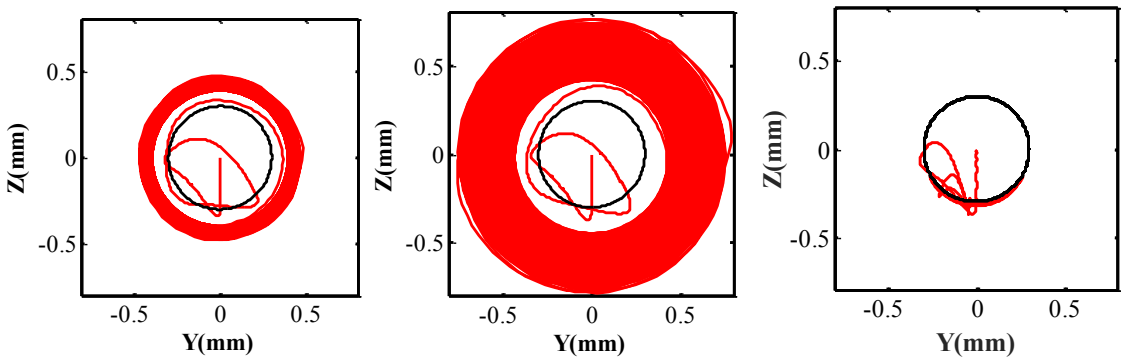

a. Without SFD, fixed ABOR b. Without SFD, soft support c. with SFD

Figure 30. Rotor drop orbit plots

Figure 30 shows that the AB mounted on the squirrel cage stiffness without the SFD results in a severe backward whirl BW. The BW is totally eliminated with the addition of the SFD.

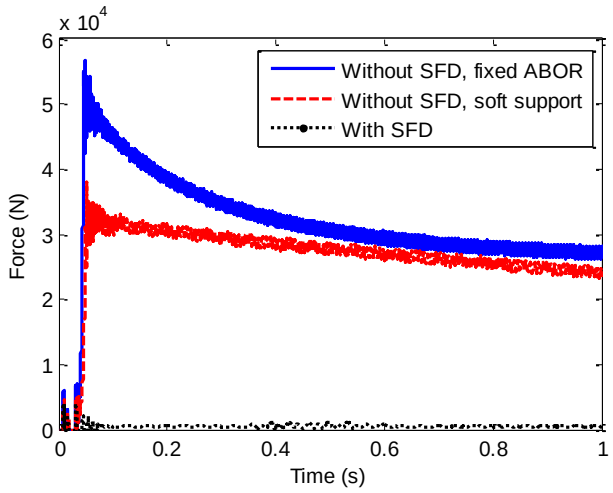

Figure 31. Normal contact forces between the shaft and AB with and without the SFD

Figure 31 shows that the AB mounted on the squirrel cage stiffness without the SFD results in very large contact forces between the shaft and the AB inner race due to the BW. The large sustained contact forces are totally eliminated with the addition of the SFD. Fixing the AB outer race to ground results in larger sustained contact forces but smaller vibration amplitude compared with the case when AB supported with the squirrel cage stiffness. Figure 32 shows the shear stresses on the segment of the ABIR with the lowest fatigue life in different supporting conditions.

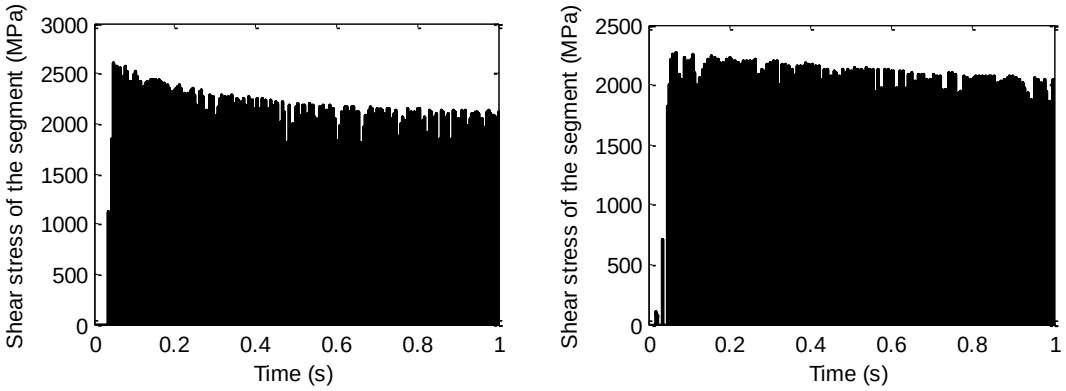

a. Without SFD, fixed ABOR

b. Without SFD, soft support

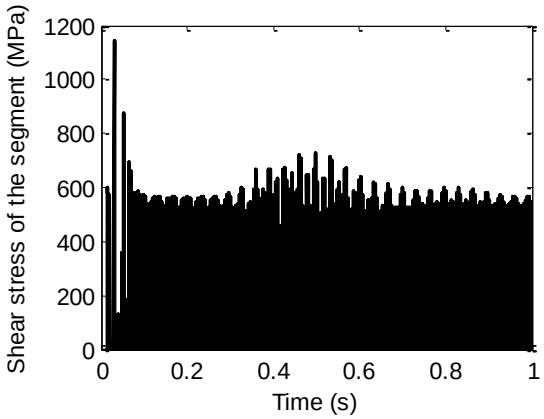

c. with SFD

Figure 32. Contact stress during rotor drop event

The large sustained stresses are totally eliminated with the addition of the SFD. Fixing the AB outer race to ground results in relatively higher stresses compared with the case with softer support. The detail stress cycle counts are shown in Figure 33.

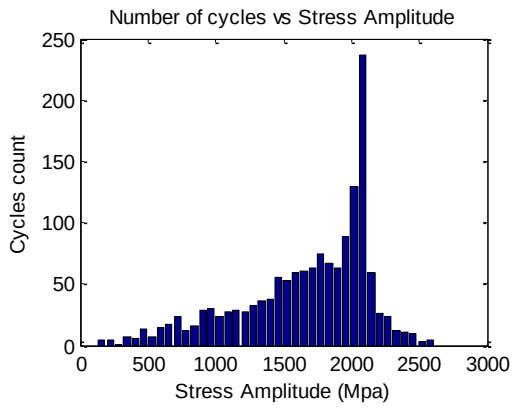

a. Without SFD, fixed ABOR

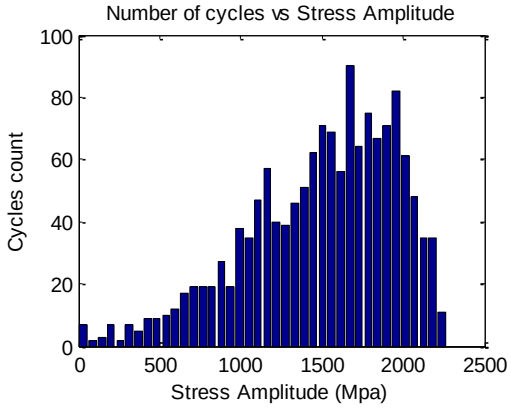

b. Without SFD, soft support

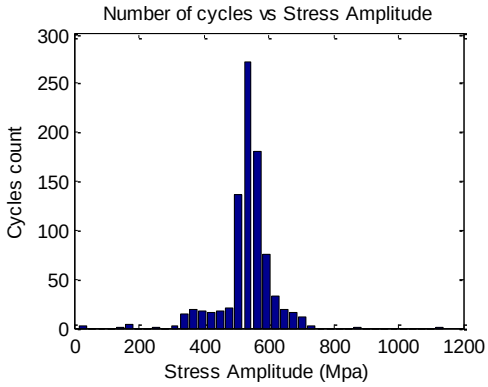

c. with SFD

Figure 33. Stress cycle of the segment of the ABIR with the lowest fatigue life

The fatigue life of the case with fixed ABOR is 2 times of drops; the case without SFD but with the soft support is 5 times of drops; the case including the SFD is 5.01e5 times of drops. It can be seen that the bearing fatigue life is significantly increased after the SFD is involved.

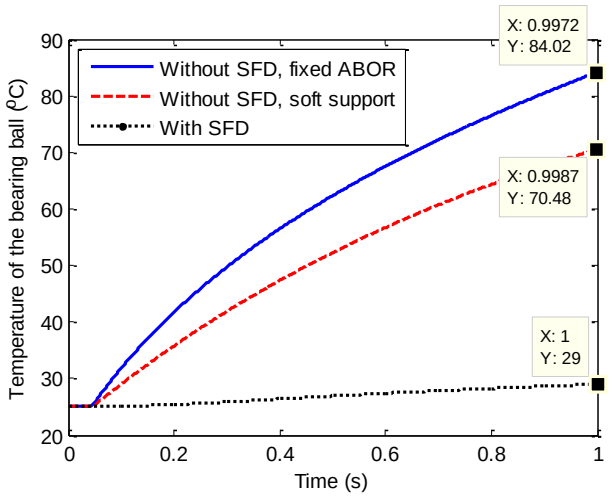

Figure 34 AB ball temperature after drop event

Figure 34 shows the temperature variation of the AB balls with and without the SFD. The results show that the increase in temperature is more than 10 times larger for the without SFD case, compared with the with SFD case. Fixing the AB outer race to ground results in higher temperature compared with the cases with softer support.

In summary, this example shows that including the SFD results in significant reductions in contact stress, contact force, temperature rise and vibration amplitudes. The example also shows that fixing the AB outer race to ground results in higher contact forces and temperature increment.

3.4 Film Clearance Influence on SFD Effectiveness

The preceding example demonstrated the benefits of a properly designed SFD on reducing vibration, contact forces, race stress and ultimately AB fatigue life. This section treats the oil film clearance as a design variable for properly designing the SFD. The clearance of the SFD film land is varied from 5mils to 15mils while the effective groove

clearance ratio between the groove land and the film land is held constant at 20. Figure 35 shows the rotor orbit with various SFD clearances. Fluid inertia is included in the film model and the zero clearance (no SFD) case includes the squirrel gage stiffness as the support for the AB.

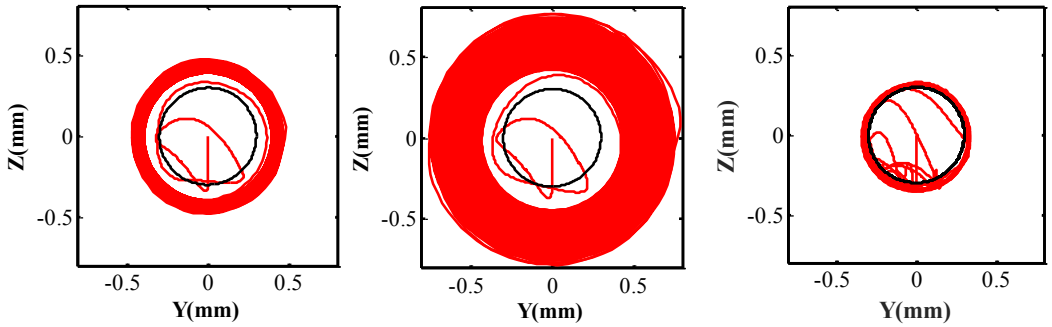

a. Without SFD, fixed ABOR b. Without SFD, soft support c. with SFD, FC 0.127mm

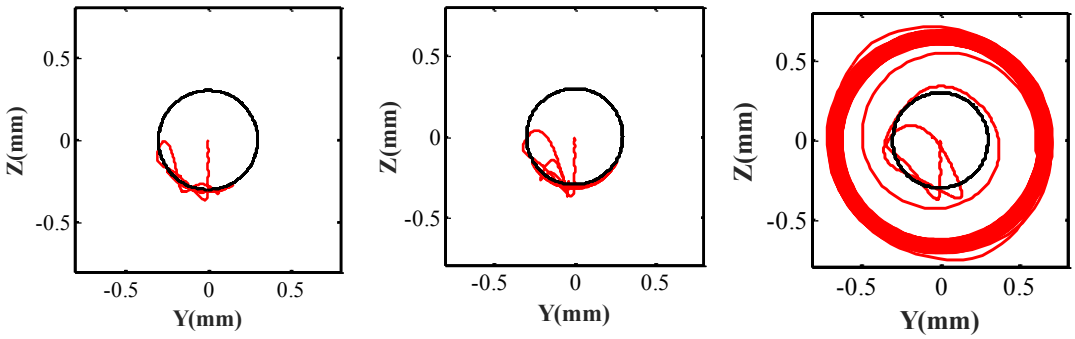

d. with SFD, FC 0.19mm e. with SFD, FC 0.257mm f. with SFD, FC 0.381mm

Figure 35. Rotor orbit with different SFD clearances, considering fluid inertia effect (FC is the film clearance of the SFD)

Figure 35 shows that the BW is eliminated when the SFD clearance is 10 mils, but is strong with a 5 mil clearance and is severe with a 15 mil clearance. This reveals that an

optimal SFD oil film clearance range exists outside of which damaging BW may occur during a drop event.

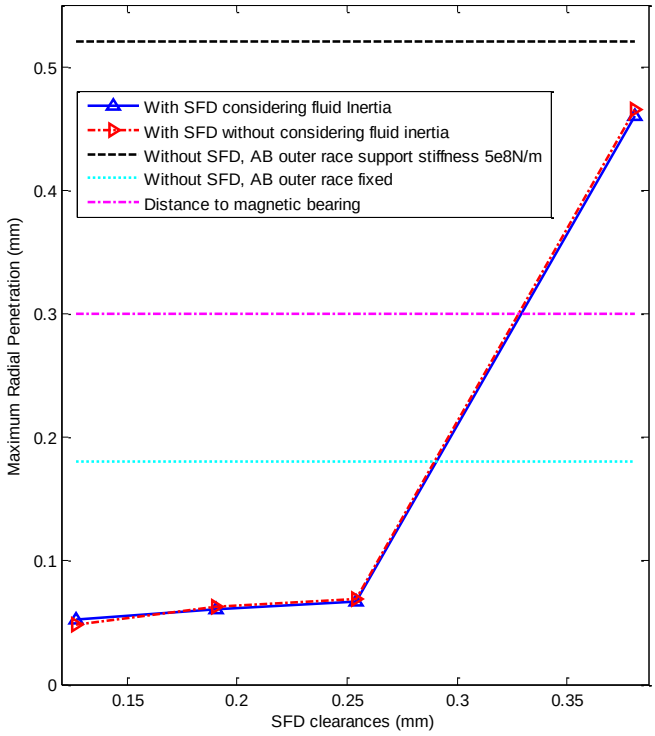

Figure 36. Maximum penetration with different SFD clearances

Figure 36 shows the AB "penetration" vs. SFD oil film clearance. Penetration here refers to the radial excursion of the shaft beyond the unloaded clearance circle of the AB. The maximum penetrations are reduced after including the SFD, however, when the clearance is 0.381mm, the rotor will still impact the AMB due to backward whirl. When the SFD oil film clearance is 0.254 mm and 0.1905mm there is no backward whirl. When the clearances is 0.127mm, the penetration is the smallest.

The normal contact forces with different SFD clearances are shown in Figure 37.

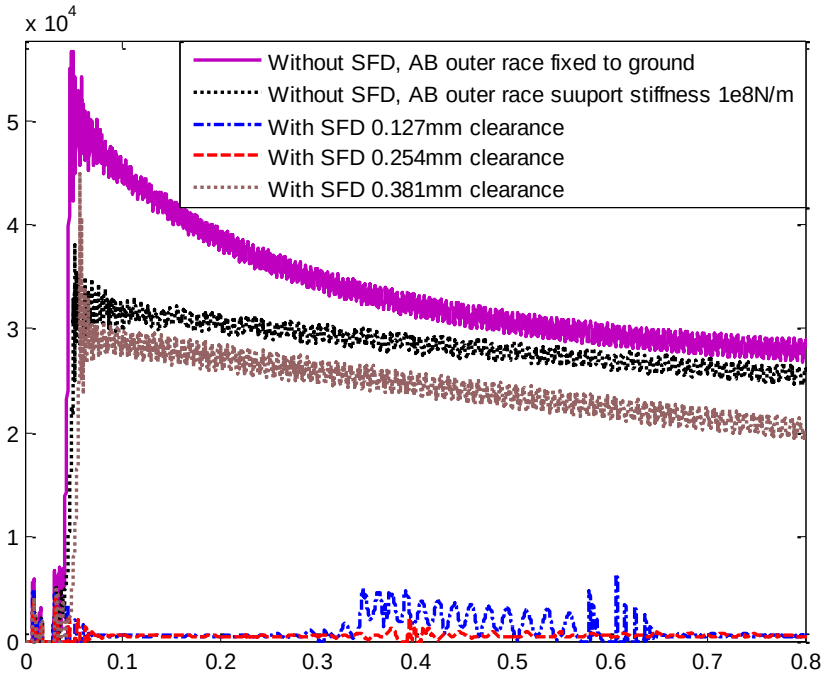

Figure 37. Normal contact force with different SFD clearances and including fluid inertia

The normal contact forces are seen to be much smaller and decay much quicker with the SFD included. The normal contact forces are the smallest when the SFD clearance is 0.254 mm, because of the elimination of backward whirl. Vance's [19] approximate formula for SFD damping coefficients is inversely proportional to the cubic power of the SFD clearance, so that damping will decrease quickly as the clearance is increased. So when the clearance is 0.381mm the damping provided by the SFD is too small to prevent BW. Alternatively the 0.127mm clearance yields too large of damping which tends to increase the contact force and reduce energy dissipation.

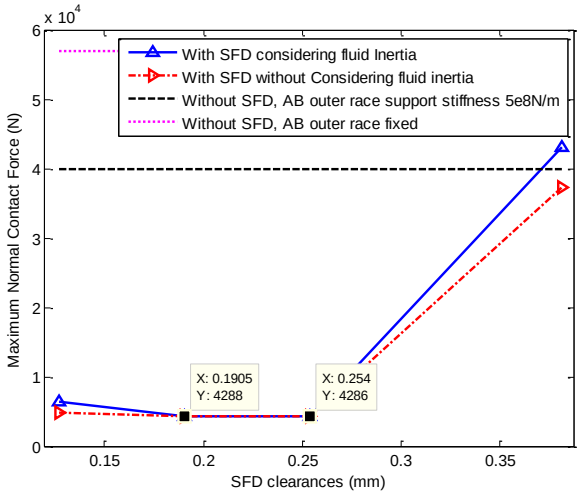

Figure 38. Maximum normal contact forces with different SFD clearances

Figure 39 shows AB has the highest fatigue life value when the clearance is 0.19mm, though the maximum normal contact force of the 0.19mm clearance SFD is smaller than the 0.254mm clearance SFD. The reason can be explained through Figure **40**, which shows the stress cycles of the ABIR segment with the lowest fatigue lives. Though the maximum contact forces are similar, 0.19mm SFD clearance case has a wider range of the stress distribution.

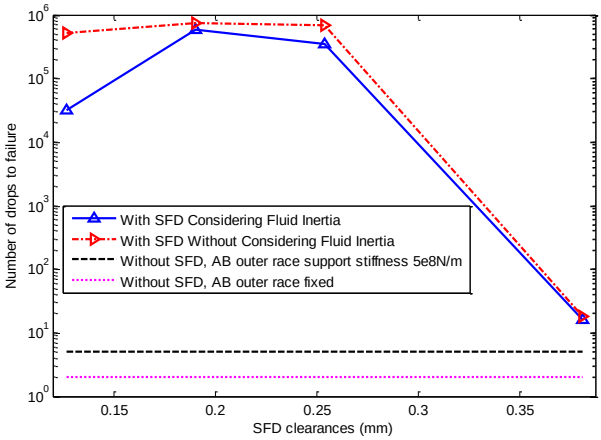

Figure 39. Fatigue lives of the AB with different SFD clearances

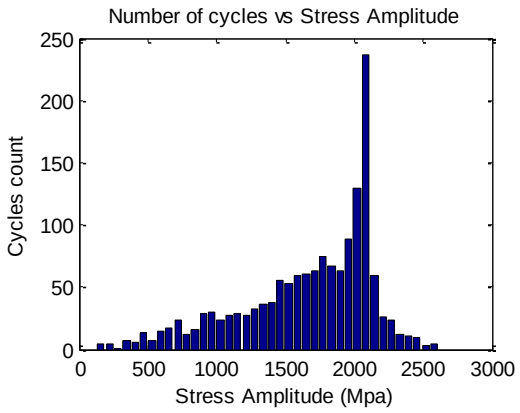

a. Without SFD, fixed ABOR

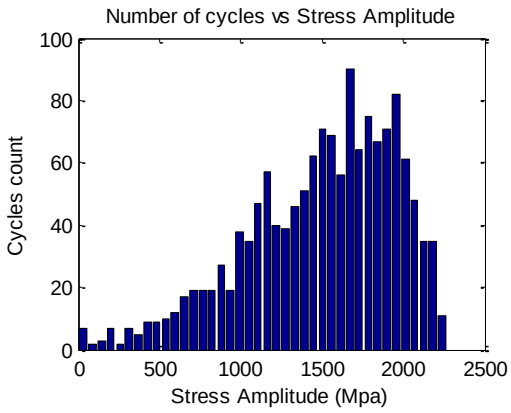

b. Without SFD, soft support

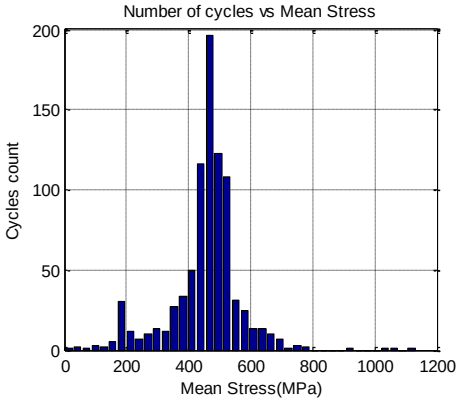

c. with SFD, film clearance 0.127mm

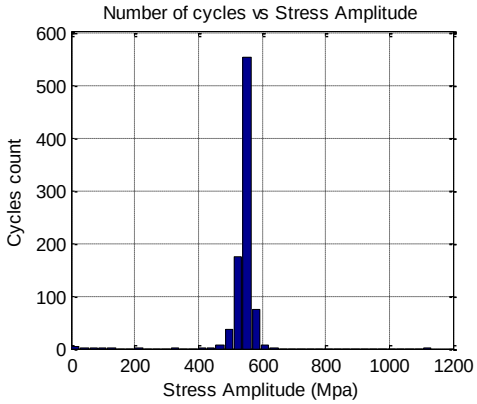

d. with SFD, film clearance 0.19mm

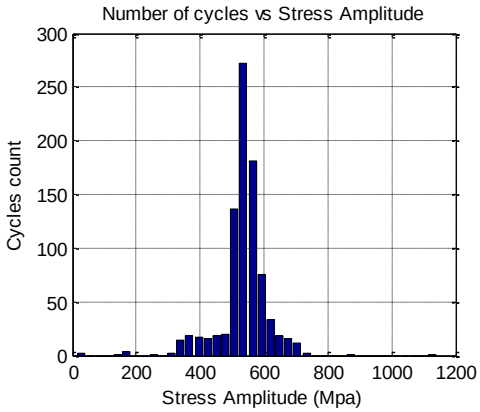

e. with SFD, film clearance 0.254mm

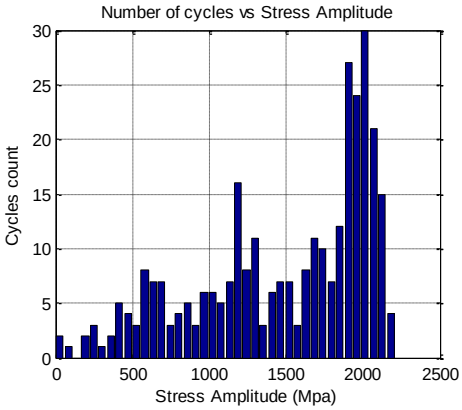

f. with SFD, film clearance 0.381mm

Figure 40. Stress cycle of the segment of the ABIR with the lowest fatigue life

3.5 Conclusion

An optimal SFD clearance occurs for reducing vibrations and contact forces during the drop event and for increasing the AB life. For the 4 SFD clearances considered 0.18mm resulted in the maximum normal contact force reaching its smallest value. An explanation is that according to Vance's [19]approximate formula the SFD damping coefficient is inversely proportional to the cubic power of the SFD clearance. The damping rapidly reduces when the clearance increases so the damping becomes too small to prevent backward whirl when the SFD clearance reaches 15 mils. Conversely, excessively decreasing the clearance will cause the damping to become too large, effectively stiffening the AB support resulting in larger contact forces. The high contact force may still result in backward whirl even though the whirl may decay fast.

Including fluid inertia in the SFD model causes the predicted contact forces. This also causes backward whirl for the 0.127mm clearance case, resulting in high contact forces and reduced fatigue life. Therefore it is important to include fluid inertia in the SFD model to avoid overestimating AB life based on race fatigue.

CHAPTER IV

HIGH FIDELITY WAVY SPRING MODEL CONSIDERING THE COULUMB FRICTION DAMPING

This chapter integrates a high fidelity wavy spring model into the auxiliary bearing system. The wavy spring model includes a mesh of finite element beam element with inertia and a multitude of nodes and degrees of freedom. The practicality of this approach is supported by the use of Guyan reduction for the wavy spring elements which significantly reduces computation time. Lee et al. [5] utilized a FEM wavy spring type model for an air foil bearing however the geometry and application differ from the AB case presented here. A gap is provided between the ends of the WFS to allow for additional sliding and friction based energy dissipation, and more accurately represent actual practice. Coulomb friction forces, occurring on the AB outer race, the wavy spring and the bearing housing are modeled with FEM determined local normal forces and with a more realistic Stribeck friction model. The Stribeck model has better numerical stability and includes a continuous transition from static to dynamic friction as a function of the sliding velocity. The WFS model is coupled into the detailed ball bearing model presented in chapter 2, to form an integrated AB sub system model. Transient response simulations of the high speed rotor dropping onto the AB with the WFS are performed to quantitatively examine the effects of AB outer race, WFS and the AB housing Coulomb friction forces on vibration, stress and fatigue life.

4.1 Wavy Friction Spring (WFS) Model

Prior wavy spring models, as described in chapter 1, either assumed uncoupled deformation between bumps, massless spring material or damping and/or spring constant values that needed to be empirically or analytically derived by unspecified means. In reality the wavy spring has inertia and deforms in a manner that is highly coupled between bumps and influenced by boundary conditions specific to each application. This impresses a need for a high fidelity model of the WFS that includes spatially varying dry friction forces, actual boundary conditions, spring inertia, etc. In response a 2D finite element beam with nonlinear dry friction model was developed as depicted in Figure 13. The wavy spring is divided up into a series of integrally connected bumps, with each bump segment modeled with 6 beam elements as shown.

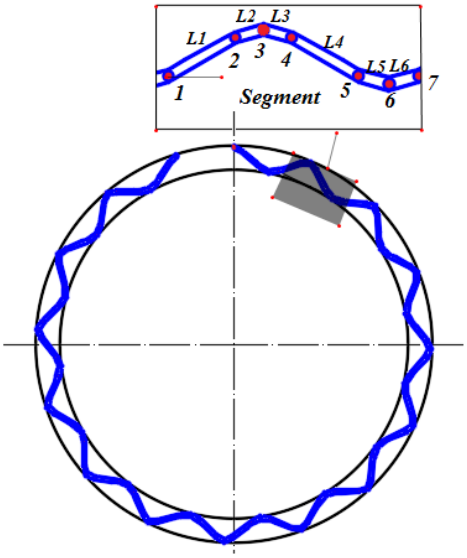

Figure 41 WFS model with bump segments discretized as beam elements

Equation (7) provides the 2D Euler beam element stiffness matrix with the term $1/(1-v^2)$ employed for modeling shell like behavior in foil bearings [20]

$$K_{beam}=\begin{bmatrix} \frac{EA}{L} & 0 & 0 & -\frac{EA}{L} & 0 & 0 \\ 0 & \frac{12EI}{L^3(1-v^2)} & \frac{6EI}{L^2(1-v^2)} & 0 & -\frac{12EI}{L^3(1-v^2)} & \frac{6EI}{L^2(1-v^2)} \\ 0 & \frac{6EI}{L^2(1-v^2)} & \frac{4EI}{L(1-v^2)} & 0 & -\frac{6EI}{L^2(1-v^2)} & \frac{2EI}{L(1-v^2)} \\ -\frac{EA}{L} & 0 & 0 & \frac{EA}{L} & 0 & 0 \\ 0 & -\frac{12EI}{L^3(1-v^2)} & -\frac{6EI}{L^2(1-v^2)} & 0 & \frac{12EI}{L^3(1-v^2)} & -\frac{6EI}{L^2(1-v^2)} \\ 0 & \frac{6EI}{L^2(1-v^2)} & \frac{2EI}{L(1-v^2)} & 0 & -\frac{6EI}{L^2(1-v^2)} & \frac{4EI}{L(1-v^2)} \end{bmatrix} \quad (57)$$

Each segment of the wavy spring is approximated by 6 Euler beam elements that vary in length and orientation angle α as shown in Figure 14. Equation (7) is the element stiffness matrix in local coordinates and corresponds with the element degree of freedom vector

$$\mathbf{X}_{tl}=\begin{bmatrix} y' & x' & \theta_{x'} \end{bmatrix}^T$$

Each element stiffness matrix is transformed into global coordinates prior to assembly into the system stiffness matrix.

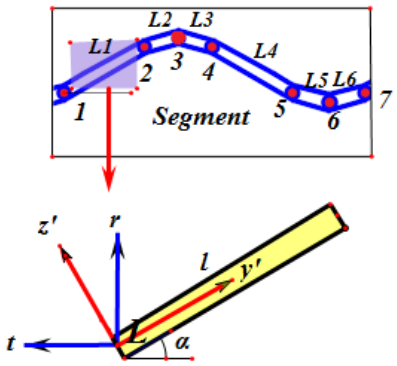

Figure 42 Typical beam element in the WFS model

The global form of the element stiffness matrix is obtained from the standard transformation

$$K_{BeamGlobal} = C^T K_{beam} C \tag{58}$$

where the coordinate transformation matrix is given by

$$\mathbf{C} = \begin{bmatrix} \sin\alpha & -\cos\alpha & 0 & 0 & 0 & 0 \\ \cos\alpha & \sin\alpha & 0 & 0 & 0 & 0 \\ 0 & 0 & 1 & 0 & 0 & 0 \\ 0 & 0 & 0 & \sin\alpha & -\cos\alpha & 0 \\ 0 & 0 & 0 & \cos\alpha & \sin\alpha & 0 \\ 0 & 0 & 0 & 0 & 0 & 1 \end{bmatrix} \tag{59}$$

Specific nodes of the WFS are located at its interfaces with the outer race of the ball bearing and with the inner bore of the stationary housing. Contact forces are evaluated at the contact points by employing an interface stiffness 10000 times larger than the maximum value in the WFS stiffness matrix. The contact force equals the interface

stiffness times its net deflection. The tangent friction force equals the coefficient of friction for the interface multiplied by the contact force if sliding is occurring.

4.2 Wavy Friction Spring (WFS) Contact Model

Figure 43 illustrates the components of the AB including the rolling element bearing, WFS and housing. Note that unlike the tolerance ring shown in Figure 5, the WFS has an angular separation arc that allows the WFS to slide circumferentially and dissipate energy through friction damping. The details of the mathematical model for obtaining the contact forces and friction forces at the wavy spring, AB outer race and housing interfaces are discussed here. Penalty springs are placed on each contact node with the stiffness 10000 times larger than the maximum value in the wavy spring's stiffness matrix [20] in order to solve for the contact forces between the auxiliary bearing outer race ABOR and the wavy spring. The radial penetrations between the ABOR surface and the correspondent wavy spring contact nodes are calculated from the previous time step, and multiplied by the penalty spring's stiffness to obtain the contact force. This occurs each time step if a logic test confirms that the surfaces are in contact at the interface node.

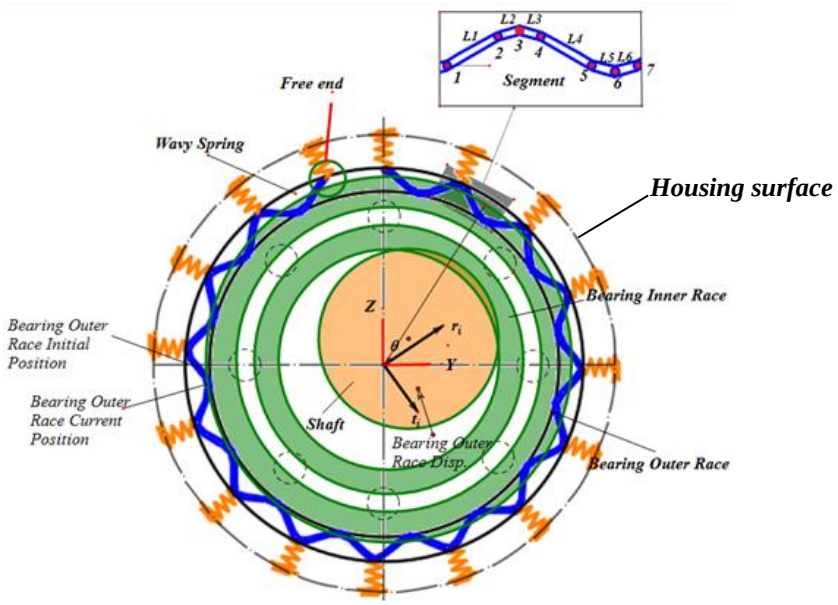

Figure 43. Contact points and penalty springs along the AB outer race, wavy spring,and housing interfaces

Radial penetration at an interface node is determined by transforming its global (system) coordinate displacement values to local coordinates, and the displacements of the ABOR at the contact point into the beam node's local coordinates. The ABOR displacement transformation is expressed as

$$\begin{bmatrix} t_i \\ r_i \end{bmatrix} = \begin{bmatrix} \cos(\theta) & -\sin(\theta) \\ \sin(\theta) & \cos(\theta) \end{bmatrix} \begin{bmatrix} Y \\ Z \end{bmatrix} \tag{60}$$

where t_i, r_i are the ABOR's displacement in the local coordinate respect to the ith contact node of the wavy spring, and Y and Z are the displacements of the ABOR in the global coordinate. Then the radial reaction forces on the ith contact node becomes

$$F_{rbi} = \begin{cases} k_{ws}(r_i - r_{nbi}), & if\ r_i - r_{ni} > 0 \\ 0, & if\ r_i - r_{nbi} \le 0 \end{cases} \tag{61}$$

where k_{ws} is the stiffness of the penalty spring between the ABOR and the wavy spring, r_{nbi} is the radial displacement of the ith contact node of the wavy spring, and F_{rbi} is the radial contact force on the ith contact node. The friction force on the ith contact node can then be obtained as.

$$F_{tj} = -\mu F_{rbj} \tag{62}$$

The following Stribeck friction model is utilized in (23)

$$\mu = \frac{2}{\pi} arc\tan(10^4 v_{rel})(\frac{\mu_s - \mu_d}{1+|v_{rel}|} + \mu_d) \tag{63}$$

The contact forces are determined in local coordinates of the beam elements but are then transformed back into global coordinates

$$\begin{bmatrix} F_{Yj} \\ F_{Zj} \end{bmatrix} = \begin{bmatrix} \cos\theta & \sin\theta \\ -\sin\theta & \cos\theta \end{bmatrix} \begin{bmatrix} F_{tj} \\ F_{rj} \end{bmatrix} \tag{64}$$

to enter into the force vector of the governing system equations of motion for the WFS. The x and y resultant of the contact forces are applied to the rigid body, AB outer race equations of motion.

The method for determining the contact forces between the WFS and the bearing housing is similar to the contact between the wavy spring and the AB outer race. The

fictitious springs are also placed at the contact nodes between the WFS and the housing to calculate the contact and friction forces between the WFS and the housing. The stiffness of the fictitious springs are obtained based on the housing stiffness. If the housing is assumed to be rigid, its stiffness value is selected as 10000 times larger than the maximum value of the stiffness matrix of the wavy spring. The local coordinate contact and friction forces are obtained and then transferred back to the global coordinate to calculate the dynamic response of the system.

4.3 Guyan Reduction Technique

As with most contact type problems involving stiff differential equations, the transient response simulation requires very small time steps to convergence, resulting in a long simulation time. This problem becomes more acute as the size of the system grows due to inclusion of the states in the finite element mesh of the WFS. Guyan reduction [21] is applied to the wavy spring model degrees of freedom for reducing the number or retained degrees of freedom to alleviate excessive computation time.

Figure 16 shows that only two nodes (segment local nodes 3 and 6) contact the AB outer race and housing within each WFS segment. The translational degrees of freedom at these nodes are retained and the remaining degrees of freedom in the segment are Guyan reduced. This ignores the inertia at the non-retained nodes which is a reasonable assumption since the spring is very thin and lightweight.

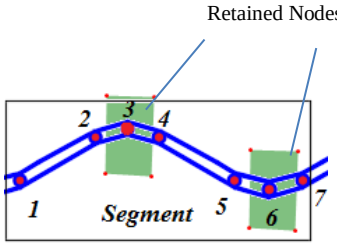

Figure 44. Retained nodes in the WFS model

Guyan reduction is applied by first reordering the degree of freedom and corresponding matrix and vector quantities to correspond with the regrouped retained and eliminated degrees of freedom in the WFS model [21]. This is represented by

$$\begin{bmatrix} q_1 \\ q_2 \\ \cdots \\ q_{n-1} \\ q_n \end{bmatrix} = \underline{T}_{(n\times n)} \begin{bmatrix} \underline{q}_r \\ \underline{q}_c \end{bmatrix}_{(n\times 1)} \tag{65}$$

where the matrix $\underline{T}$ is the reordering matrix. Then the reordered wavy spring mass M and stiffness K matrices become

$$M = T^T \hat{M} T = \begin{bmatrix} \underline{m}_{rr} & \underline{m}_{rc} \\ \underline{m}_{cr} & \underline{m}_{cc} \end{bmatrix}; \quad K = T^T \hat{K} T = \begin{bmatrix} \underline{k}_{rr} & \underline{k}_{rc} \\ \underline{k}_{cr} & \underline{k}_{cc} \end{bmatrix} \tag{66}$$

The Guyan reduced differential equations for the WFS are

$$\begin{bmatrix} \underline{m}_{rr} & \underline{0} \\ \underline{0} & \underline{0} \end{bmatrix} \begin{bmatrix} \ddot{\underline{q}}_r \\ \ddot{\underline{q}}_c \end{bmatrix} + \begin{bmatrix} \underline{k}_{rr} & \underline{k}_{rc} \\ \underline{k}_{cr} & \underline{k}_{cc} \end{bmatrix} \begin{bmatrix} \underline{q}_r \\ \underline{q}_c \end{bmatrix} = \begin{bmatrix} \underline{f}_r \\ \underline{0} \end{bmatrix} \tag{67}$$

$$\underline{m}_{rr} \ddot{\underline{q}}_r + (\underline{k}_{rr} - \underline{k}_{rc} \underline{k}_{cc}^{-1} \underline{k}_{cr}) \underline{q}_r = \underline{f}_r \tag{68}$$

Thus the WFS is represented by only its retained degrees of freedom in the system's transient simulation. The eliminated (condensed) degree of freedom displacements can be recovered from the retained degree of freedom displacements via the Guyan step [21]

$$\begin{bmatrix} q_1 \\ q_2 \\ \cdots \\ q_{n-1} \\ q_n \end{bmatrix} = \underline{T}' \underline{T}_{GY} [\underline{q}_r]_{(n_r \times 1)} \tag{69}$$

where

$$\underline{T}_{GY} = \begin{bmatrix} I_{(n_r \times n_r)} \\ -\underline{k}_{cc}^{-1} \underline{k}_{cr} \end{bmatrix}_{(n \times n_r)} \tag{70}$$

4.4 WFS Model

The wavy spring structure is shown in

Figure 45 and the related parameters are shown in Table 6. Note that the WFS only covers an angular extent of $\varphi=310$ *degrees* and is not a closed loop.

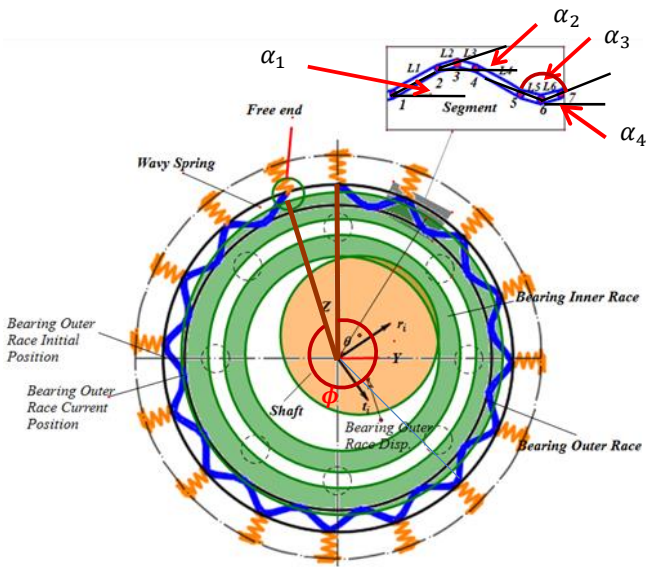

Figure 45. WFS geometry

Figure 46 shows that the wavy spring is constrained radially by elastic springs with a stiffness of 5e8N/m. The model is also meshed with 3D solid elements in Solid Works to verify the accuracy of the 2D beam model used in the system dynamics model. The benchmark consists of applying a concentrated static load at the node shown in Figure 46, and then comparing displacements of the 2D beam and 3D solid element models.

Table 6. WFS geometrical and material properties

Number of Segments	12
Young's Modulus	2.00E+11
Poison Ratio	0.3
Density (kg/m^3)	7.80E+03
Thickness (m)	5.00E-04
Width (m)	1.60E-02
Support Stiffness	2.00E+07
α_1 (degree)	25
α_2 (degree)	14
α_3 (degree)	14
α_4 (degree)	25
φ(degree)	310
L1 (m)	9.87E-03
L2 (m)	3.25E-03
L3 (m)	3.25E-03
L4 (m)	9.87E-03
L5 (m)	3.25E-03
L6 (m)	3.25E-03

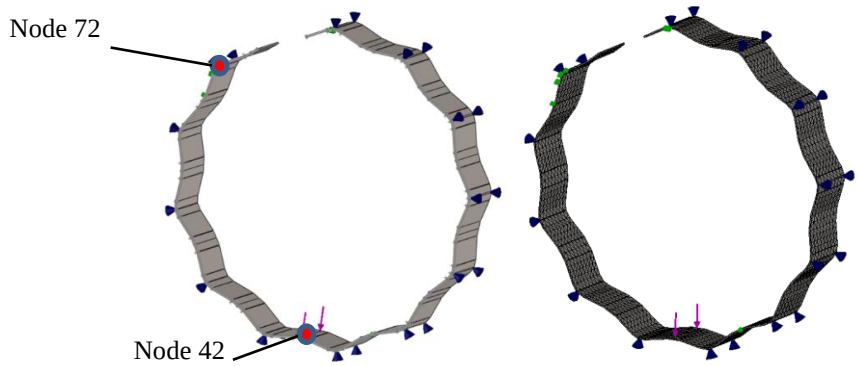

a. Beam Model: Constraint and applied force b. 3D mesh in Solid Works

Figure 46 Structure models of the wavy spring

Figure 46 shows the displacements of the 2 models at node 42, where the load is applied, and at node 72 which is located at the end of the wavy spring. The maximum difference between displacements from the 2D beam and Solid Works 3D solid element models is 10% for node 42 and 13% for node 72. These differences were judged to be acceptable for utilizing the 2D beam model in the system nonlinear dynamics study, in order to reduce computation time.

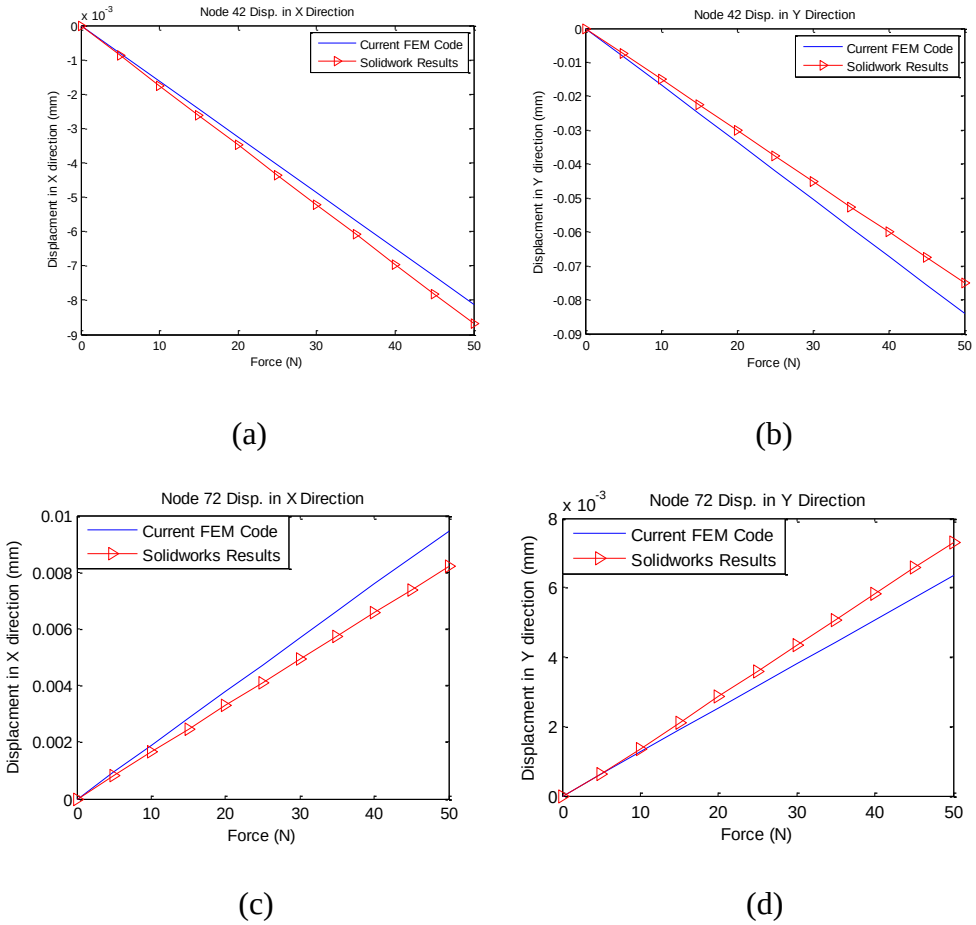

Figure 47 Comparison between FEM Wavy spring code and Solidworks

4.5 WFS Effectiveness for Reducing Vibration and Extending Race Life

This section provides a numerical example to demonstrate the effectiveness of a WFS in suppressing vibration and extending AB race life for repeated, high speed rotor drops. Figure 29 shows the rotor geometry and the location of the auxiliary bearings for the transient, rotor drop simulation. The friction coefficient between the rotor and the AB inner race is set the lowest value (0.35) for which backward whirl occurs when the AB ball bearing is hard mounted, i.e. the WFS is not utilized. The geometry of the wavy spring is illustrated in

Figure 45, and the WFS parameters are given inTable 6. Table 7 provides other parameter values utilized in the transient rotor drop simulation.

Table 7. Rotor drop transient simulation parameters

Rotor material	Steel
Auxiliary Bearing Clearance (mm)	0.3
Rotor drop spin speed (RPM)	10000
Magnetic bearing clearance (mm)	0.6
Auxiliary ball bearing type	6016

Figure 48 shows vibration response orbits during a drop event for the case that the friction coefficient between the rotor and AB inner race is 0.35. Here the static friction is treated to be the same as the dynamic friction coefficient.

Figure 48a shows severe vibration due to backward whirl occurring for the no WFS arrangement, in which case the AB outer race is fixed to ground. The remaining figures in Figure 48 shows the orbit response including the WFS with a range of friction coefficient μ_w values. This is the friction coefficient value between the wavy spring and housing and between the wavy spring and AB outer race.

Insertion of the WFS stops the backwards whirl, even with zero friction $\mu_w = 0$, due to its support softening effect and ensuing reduction of the normal and friction forces between the rotor and the AB inner race. Increasing μ_w causes a further decrease in the vibration severity.

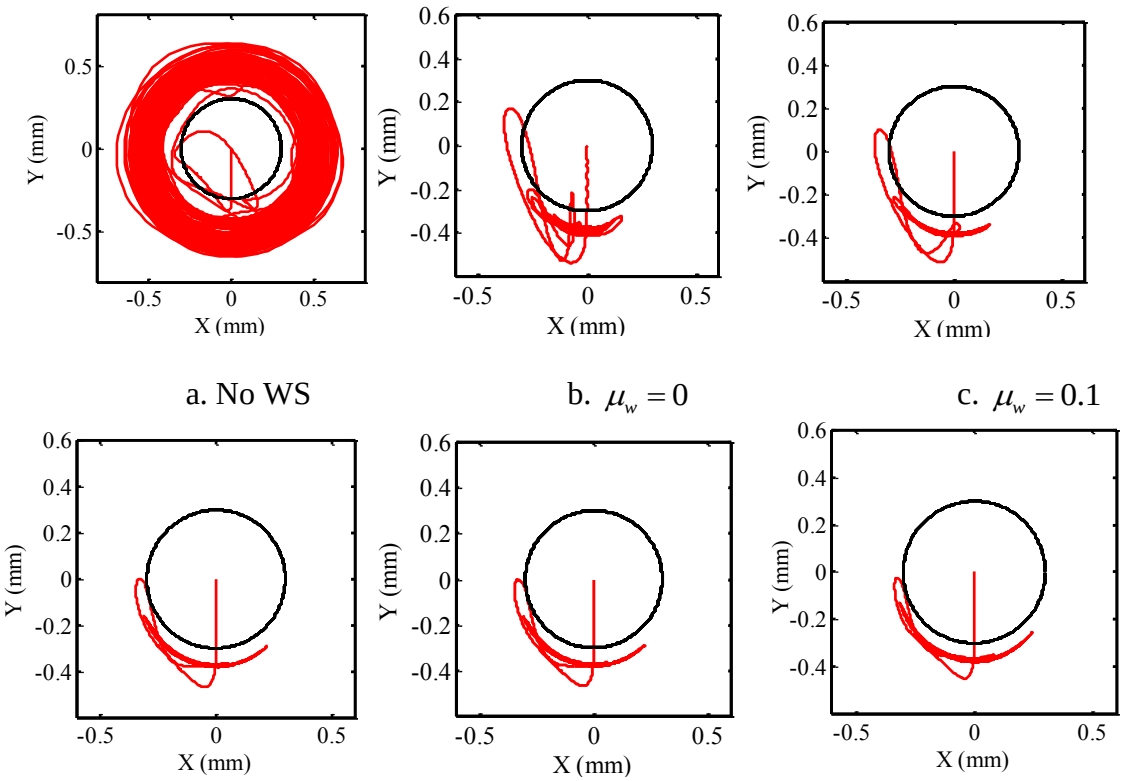

a. No WS b. $\mu_w = 0$ c. $\mu_w = 0.1$

d. $\mu_w = 0.2$ e. $\mu_w = 0.3$ f. $\mu_w = 0.4$

Figure 48. Rotor orbit at node 3 vs. friction coefficient μ_w with a rotor –inner race friction coefficient μ_r = 0.35

Figure 49 shows vibration response orbits during a drop event for the case that the friction coefficient between the rotor and AB inner race is 0.40. Figure 49a shows severe vibration due to backward whirl occurring for the no WFS arrangement, in which case the AB outer race is fixed to ground. The backward whirl persists with the WFS inserted for no or very light $\mu_w = 0.1$ wavy spring friction.

The backward whirl is totally suppressed with the WFS and $\mu_w \geq 0.2$, and the rotor drop vibrations continue to decrease with increasing μ_w.

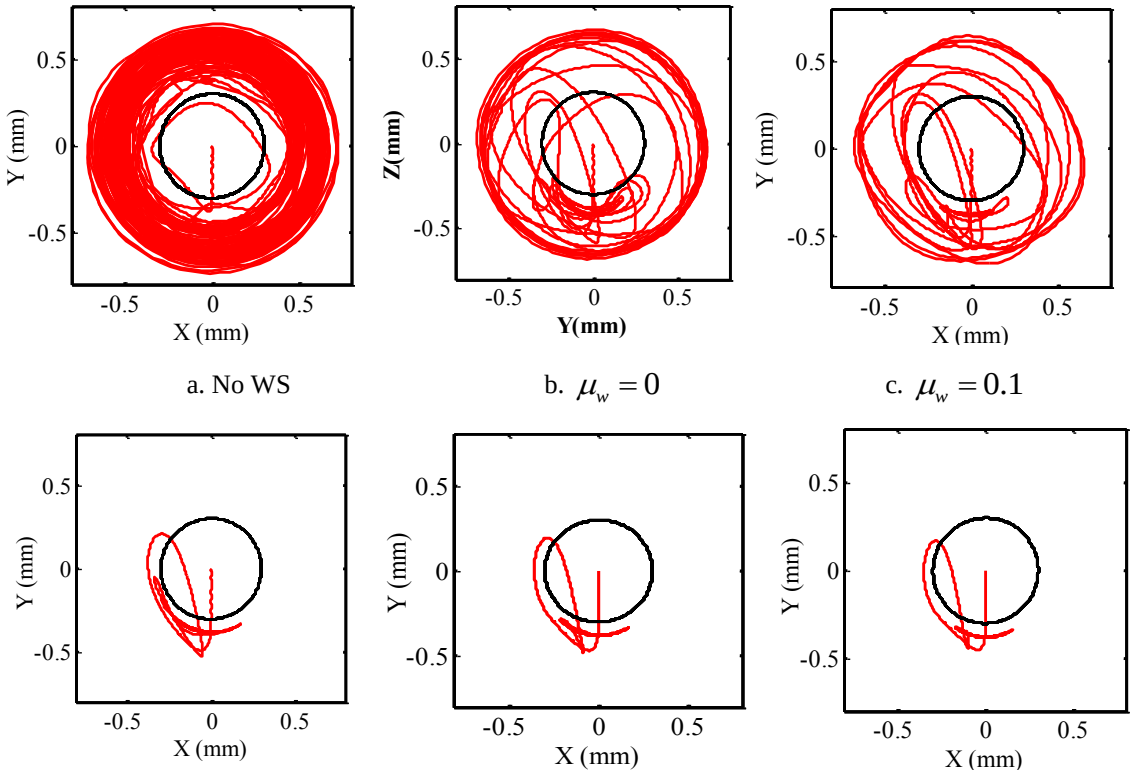

a. No WS b. $\mu_w = 0$ c. $\mu_w = 0.1$

d. $\mu_w = 0.2$ e. $\mu_w = 0.3$ f. $\mu_w = 0.4$

Figure 49. Rotor orbit at node 3 vs. friction coefficient μ_w with arotor –inner race friction coefficient μ_r = 0.40

Although backwards whirl occurs with the WFS installed, if $\mu_w = 0.1$ or lower, the duration of the backward whirl is significantly reduced relative to the no WFS case, as

shown in Figure 50. Increasing the wavy spring friction from 0 to 0.1 decreases the duration of backward whirl from 0.35 to 0.25 seconds.

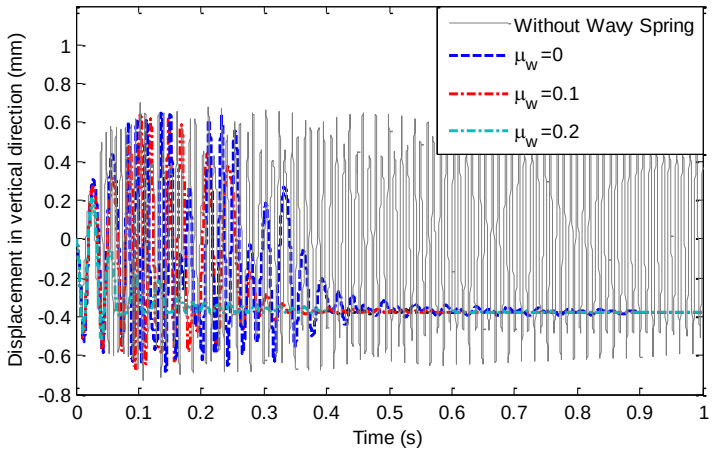

Figure 50. Rotor vertical displacement at node 3 when the friction coefficient between the rotor and AB is μ_r =0.4

The rotor's vibration whirl frequency is determined from the equation

$$f_w = \frac{\dot{y}y + \dot{z}z}{2\pi d_r} \tag{71}$$

The reaction force varies approximately as proportional to the square of the whirl frequency so high whirl frequencies imply greater forces and stresses acting on the AB. Figure 51 shows the rotor whirl frequencies at node 3 with different AB support conditions and μ_r = 0.4. The negative values indicate the occurrence of backward whirl, which is seen to vary in severity and duration depending on the AB support conditions. Clearly the WFS is seen to significantly mitigate backward whirl, which occurs at the high value of -169 Hz without a WFS. Including a frictionless wavy spring reduces the whirl frequency to -149 Hz and decreases the total duration to 1s. The whirl frequency reduces to -79 Hz and its duration decreases to 0.8 seconds when a small amount of wavy spring

friction $\mu_w = 0.1$ is included in the model. Backward whirl is entirely eliminated when $\mu_w \geq 0.2$ as shown in Figure 50. Figure 51 also shows that the DBWs reduces after implementing the wavy spring and considering the friction damping.

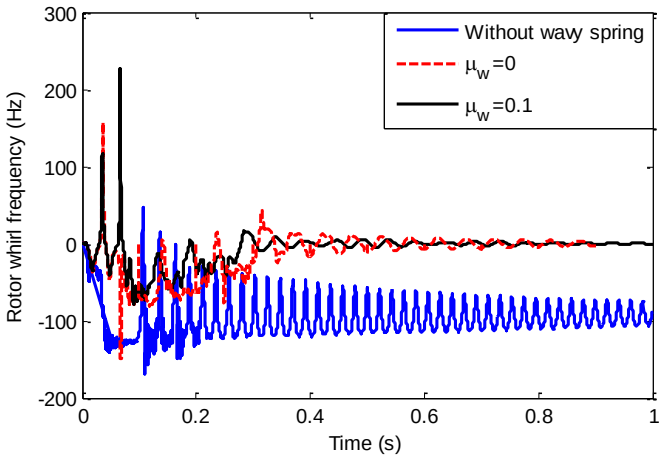

Figure 51. Rotor whirl frequency without wavy spring, and with frictionless and $\mu_w = 0.1$ wavy springs

The rotor will penetrate through the unloaded AB's clearance circle following the drop event. Excessive penetration will lead to contact between the spinning rotor and the fixed magnetic bearing stator, potentially causing severe damage.

Figure 52 shows the rotor's maximum radial penetration MRP during the drop event, vs. wavy spring friction coefficient μ_w and rotor-inner race friction coefficient μ_r. An increase in rotor –race friction μ_r is seen to cause an increase in maximum radial penetration, similar to the O ring damper results in Figure 58. The MRP is significantly attenuated with the WFS installed and with MRP decreasing monotonically with μ_w Both increased energy dissipation and increased stiffness act to reduce MRP with the increasing

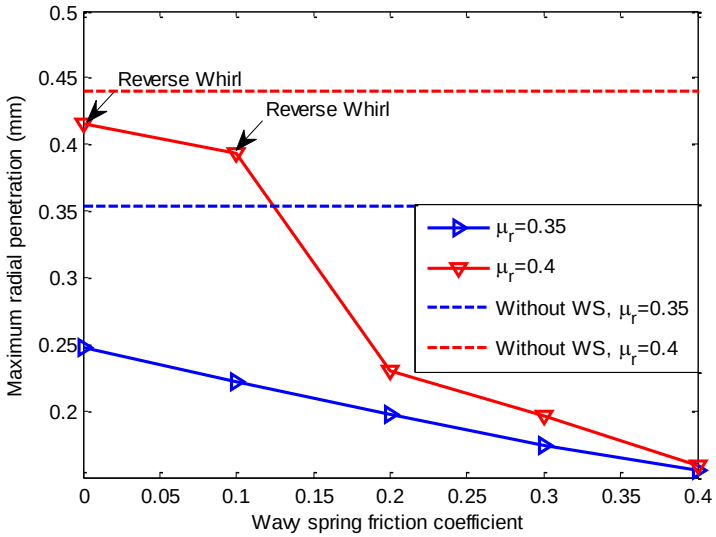

Figure 52. Maximum radial penetration at node 3 vs. μ_w with different support conditions

The maximum normal contact force MNCF shows an approximate 10 fold decrease with implementation of the WFS with reasonable wavy spring friction values in Figure 53. Increasing the rotor-race friction coefficient μ_r causes a large increase in the MNCF, with the exception that the sensitivity to increasing μ_r is minor, if a WFS is installed and the $\mu_w \geq 0.2$.

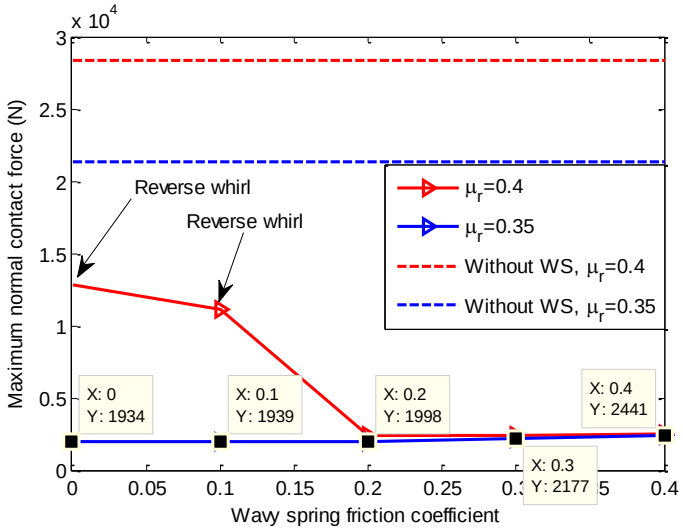

Figure 53. Maximum normal contact force at node 3 vs. μ_w with different support conditions

Figure 55 and Figure 55 shows histograms of the no. of cycles vs. inner race stress amplitude at the left AB during the rotor drop event as determined utilizing the rainflow counting and accompanying methods provided in **[5]**. The rotor – AB inner race friction coefficient was held fixed at $\mu_r = 0.35$ in Figure 54. Consistent with Figure 48 installing the WFS greatly decreases the cyclic shear stress levels and the frequencies of occurrence. Increasing the wavy spring friction coefficient further reduces the cyclic shear stress levels and frequencies of occurrence. This is consistent with the reduction and elimination of backward whirl and decreased response in general shown in Figure 48.

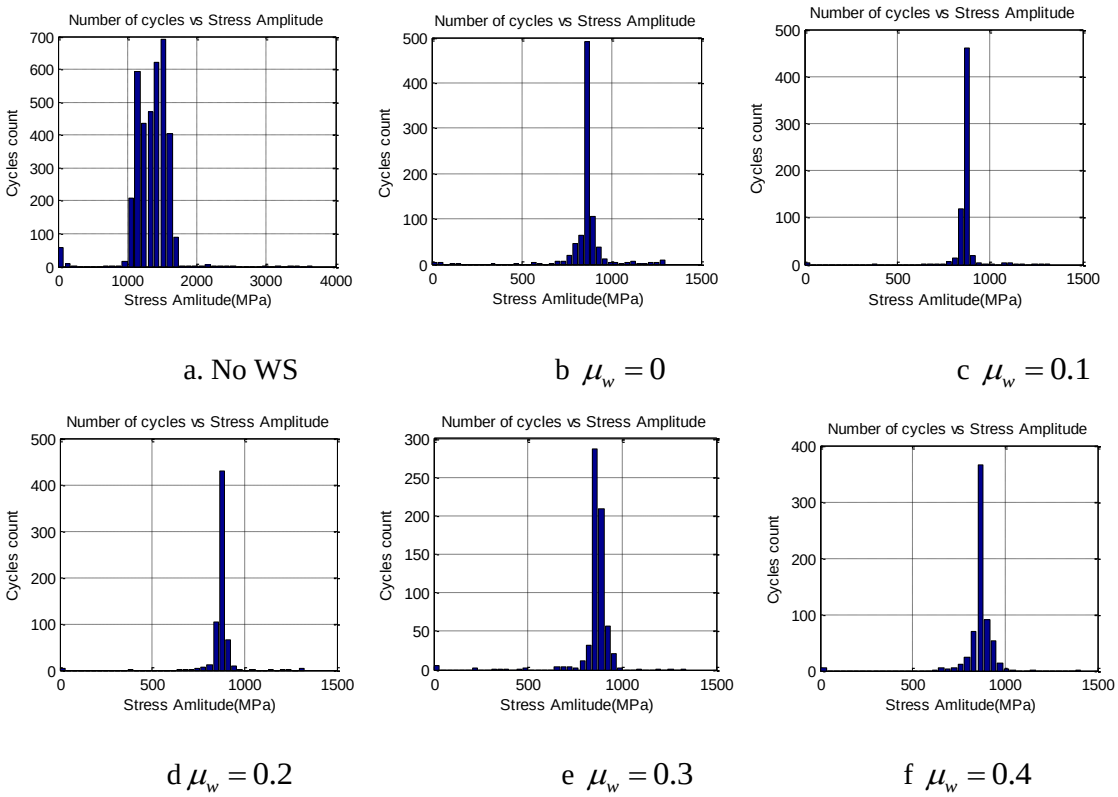

Figure 54. Histograms of cycle count vs. stress amplitude during drop events for with and without the WFS, varying wavy spring friction coefficient μ_w, and $\mu_r = 0.35$

Figure 55 corresponds to identical conditions as in Figure 54 except that the rotor-AB inner race friction coefficient has been increased to $\mu_r = 0.40$. This change increases the stress levels and frequencies, but the general stress and frequency response trends are the same as in Figure 48.

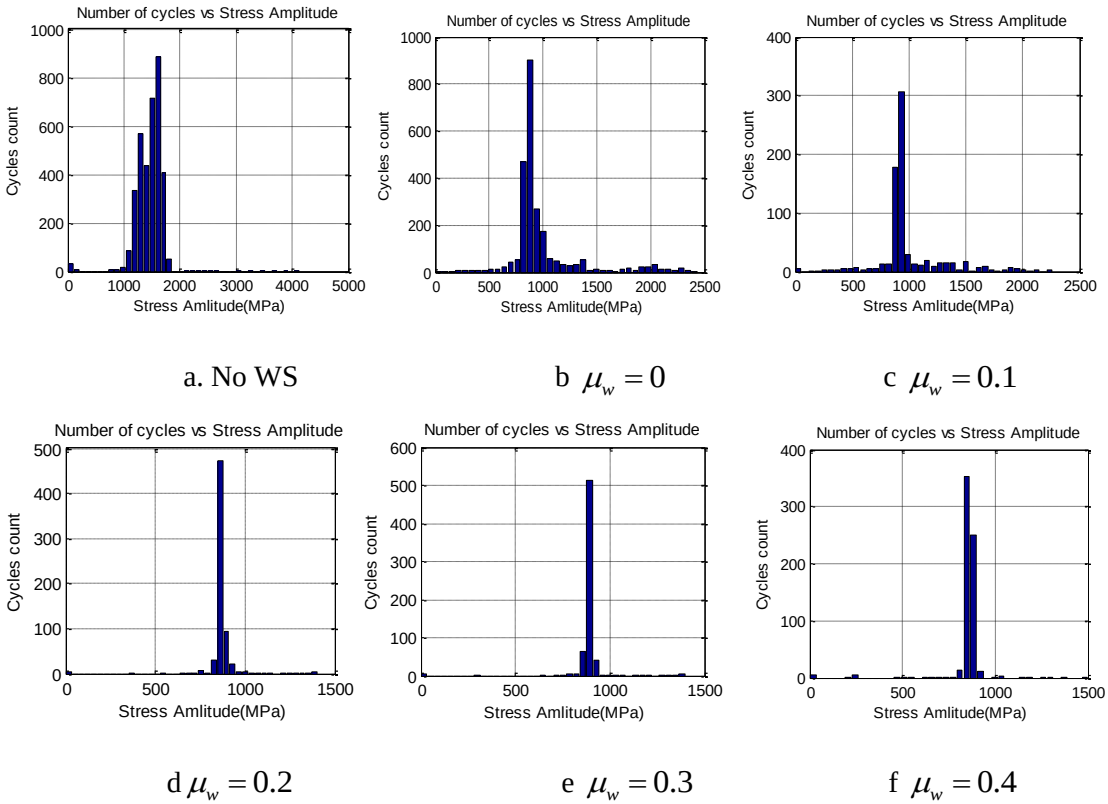

Figure 55. Histograms of cycle count vs. stress amplitude during drop events for with and without the WFS, varying wavy spring friction coefficient μ_w, and $\mu_r = 0.40$

Figure 56 and Table 8 show the auxiliary bearing inner race fatigue life vs. wavy spring friction coefficient μ_w, varying rotor-race friction μ_r, and with and without WFS. Life is defined here as the number of drop events that can occur before the inner race experiences fatigue failure **[5]**.The general trend indicates that a significant increase in inner race life is obtained by incorporating a WFS into the AB. This is most apparent for the higher value of inner race-rotor friction $\mu_r = 0.40$. The general trend also indicates increasing inner race life with increasing wavy spring friction. μ_w. This results mainly

from the reduction or elimination of backward whirl as a result of the wavy spring's compliance and friction damping.

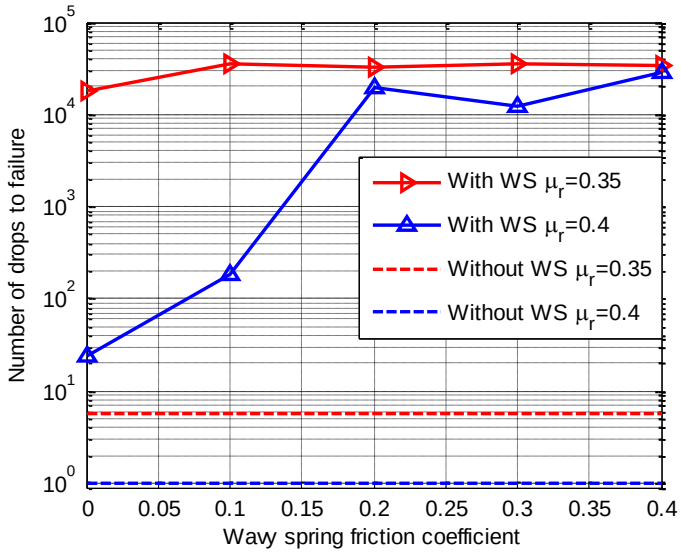

Figure 56 AB inner race fatigue life vs. wavy spring friction coefficient μ_w, varying rotor-race friction μ_r, and with and without WFS

Table 8. Number of rotor drop events before failure

Friction coefficient between rotor and ABIR	Without a wavy spring	$\mu_w = 0$	$\mu_w = 0.1$	$\mu_w = 0.2$	$\mu_w = 0.3$	$\mu_w = 0.4$
$\mu_r = 0.35$	5	17633	36092	32575	35065	24300
$\mu_r = 0.4$	1	23	183	19593	12482	29005

4.6 Conclusion

1. The relatively low stiffness and friction characteristics of the wavy friction spring provide means to mitigate destructive backward whirl, reduce post initial contact vibration, contact force and whirl frequency, and extend AB inner race fatigue life.

2. Increasing wavy spring friction coefficient reduces backward whirl frequency and durations, inner race contact force and stress, and the number of fatigue stress cycles, to increase inner race fatigue life.

3. A high wavy spring friction coefficient can increase the “first hit” peak rotor drop contact force in the absence of backward whirl, which results from the reduction in wavy spring compliance due to the increased friction.

CHAPTER V

AUXILIARY BEARING WITH ELASTOMOR O-RING

OR and other elastomer dampers are widely used to provide damping to rolling element bearing because of their simplicity, inherent combination of stiffness and damping and lack of need for seals or an oil supply. In 1978, Smalley et al. [10] experimentally investigated the dynamic characteristics of OR and obtained their frequency-dependent-stiffness and loss coefficients with different materials, temperatures, squeeze ratios, stretch ratios etc. This reference contains much valuable design information for incorporating OR into SFD and ball bearings. The present paper integrates the OR characteristics measured in [10] into the high fidelity AB ball bearing model provided in Part 1. An approach for converting the frequency dependent stiffness and loss coefficient data provided in reference [10] to a transfer function representation is presented below. This latter representation provides a form that is readily integrated into the total system model for transient response simulation. Figure 1 illustrates the integration of OR in the overall ball bearing – AB design.

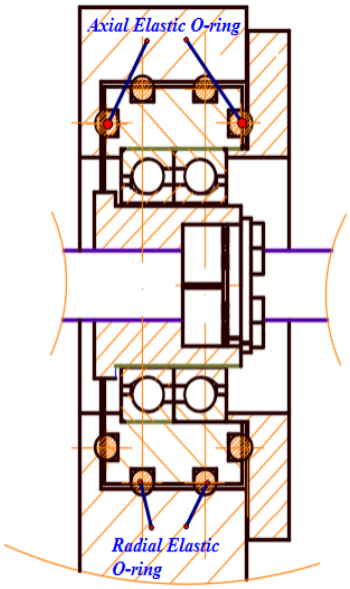

Figure 57. Ball Bearing Type AB with OR Supports

O-Rings are inserted in grooves machined into a steel cartridge assembled between the AB and the housing in Figure 57. The groove depths can be adjusted by inserting shims to change the squeeze ratio of the O-Ring. The influence of the different squeeze ratios on the dynamic and thermal behavior after a rotor drop is studied, and the optimal squeeze ratio is selected.

5.1 O-Ring (OR) Model

The O-ring model utilizes test data from [10] which provided frequency dependent stiffness and loss coefficients for O-rings with a variety of materials and squeeze ratios. The dynamic stiffness of the O ring provided by [10] is given by

$$K_{seq} = K_s(1+i\gamma) \tag{72}$$

where K_{seq} is the dynamic stiffness, $K_s(\omega)$ is frequency dependent OR stiffness and γ is the frequency dependent OR loss coefficient. The force due to the OR is expressed as

$$F_s = K_s r_s + C_s \dot{r}_s \tag{73}$$

r_s is the radial penetration of the O-ring by the AB outer race cartridge and $C_s(\omega)$ is the frequency dependent OR damping. The measurements in [10] are made under steady state harmonic conditions so in this case (73) has the form

$$\hat{F}_s e^{i\omega t} = K_s \hat{r}_s e^{i\omega t} + C_s i\omega \hat{r}_s e^{i\omega t} \tag{74}$$

where ω is the excitation frequency. Eq. (74)may be written

$$\hat{F}_s = (K_s + i\omega C_s)\hat{r}_s = K_{seq}\hat{r}_s \tag{75}$$

Matching terms in (72)and (75) yields

$$\gamma(\omega) = C_s(\omega)\ \omega / K_s(\omega) \tag{76}$$

The frequency dependence of the OR stiffness and damping may be incorporated in the transient rotor drop simulation utilizing the state space (canonical) form of the transfer function that has the frequency response:

$$T(s = i\omega) = \frac{F_s(s = i\omega)}{r_s(s = i\omega)} = K_s(\omega) + iK_s(\omega)\gamma(\omega))\ = K_{seq} \tag{77}$$

The frequency response function in (5) is utilized to obtain the coefficients for the corresponding transfer function

$$T(s) = \frac{b(s)}{a(s)} = \frac{b_0 s^m + b_1 s^{m-1} + ... + b_{m-1} s + b_m}{s^n + a_1 s^{n-1} + ... + a_{n-1} s + a_n} \quad (78)$$

The equation above can be written into a state space form and solved along with other differential equations of the rotor-auxiliary bearing system.

5.2 Parameter Effects for Rotor Drop on AB with OR

This section provides a numerical example to illustrate the influence of rotor-inner race friction coefficient and OR radial squeeze ratio. Viton-70 is selected as the O-ring material for its relatively low stiffness and high loss coefficients. The rotor-bearing system is illustrated in. The OR are inserted in circumferential grooves of a cartridge as illustrated in Figure 57. Each AB is supported by two O-rings in the radial directions. Figure 29 shows the rotor geometry and the location of the auxiliary bearings for the transient, rotor drop simulation. The parameters for the transient simulation are listed in Table 9.

Table 9. Parameter Values for Rotor Drop Transient Simulation

Rotor material	Steel
Auxiliary Bearing Clearance (mm) (Drop Height)	0.3
Rotor drop spin speed (RPM)	10000
O-ring material	Viton-70
Number O-rings for each AB	2
Magnetic bearing clearance (mm)	0.6
Auxiliary ball bearing type	6016

Figure 58 shows vibration orbit responses for ranges of shaft – inner race contact friction coefficient and OR squeeze ratio. Destructive backward whirl occurs in the absence of the OR damper for friction coefficient values exceeding 0.3. The OR penetration in this case is seen to exceed 0.3 indicating contact between the spinning shaft and the magnetic bearing stator will occur for the values listed in Table 9. The OR damper prevents backward whirl for squeeze ratios less than or equal to 20%. However, destructive backward whirl occurs for an OR squeeze ratio of 30% and friction coefficient of 0.35. Figure 59 shows the maximum normal contact force MNCF occurring during the transient simulation vs. OR squeeze ratio and shaft-inner race friction coefficient. The OR damper greatly reduces the MNCF especially for squeeze ratios less than 30%. The MNCF is unaffected by friction coefficient value until backward whirl begins and then significantly increase with increased coefficient of friction. The MNCF increases slightly with squeeze ratio for friction coefficient less than 0.35, and increases greatly with squeeze ratio for friction coefficient equal to 0.35 and squeeze ratio equal to 30%. AB life is evaluated based on race stress using the rainflow cycle counting method as outlined in chapter 2 and [13]. Table 10 shows the calculated AB fatigue life in number of rotor drop events before failure vs. OR squeeze ratio and shaft-inner race friction coefficient. The fatigue life for the case without the OR damper is also included in the table.

Table 10. Fatigue life in number of rotor drop events before failure vs. OR squeeze ratio and shaft – inner race friction coefficient

Squeeze Ratio	Dynamic friction coefficient			
	0.1	0.2	0.3	0.35
5%	3.44E+04	2.39E+04	2.09E+04	2.02E+04
10%	1.91E+04	1.71E+04	1.62E+04	1.41E+04
20%	1.68E+04	1.32E+04	1.36E+04	1.26E+04
30%	1.40E+04	9.00E+03	8.37E+03	6
No O-ring	6.52E+03	3.91E+03	1	0.18

Figure 60 and Table 10 show that the including the OR damper significantly increases the AB race life, and that the life varies inversely with OR squeeze ratio. The life also decreases with increasing shaft-inner race friction coefficient, and greatly decreases when backward whirl occurs. A comparison of Figure 61 and Figure 62 and Table 10 shows that the OR damper is seen to significantly increase AB race life even if backward whirl is not present. For the highest coefficient of friction (0.35) case the AB's life is expended only after 1 drop, however including the OR damper extends the life to 6 drops even for the high squeeze ratio value 30%.

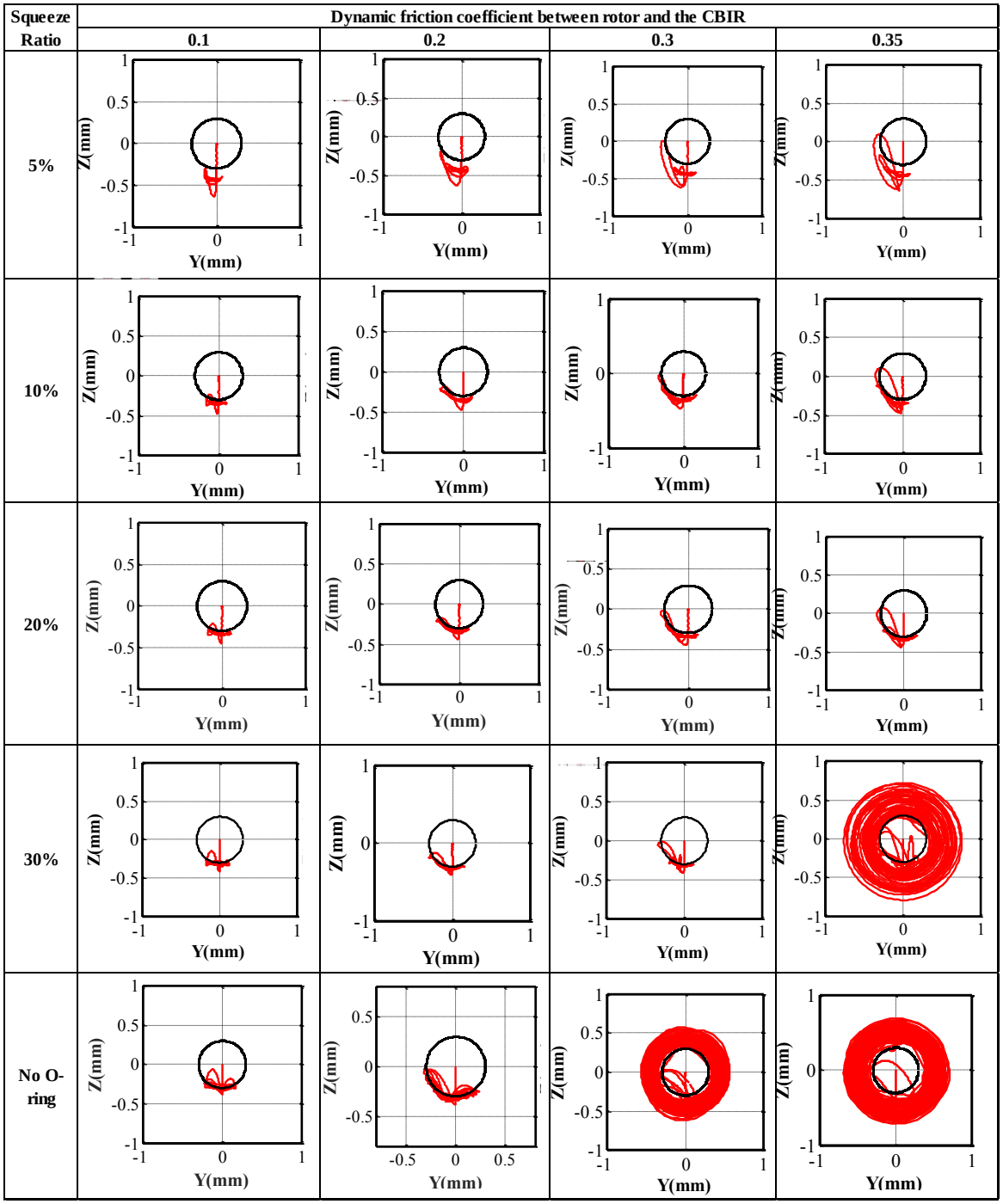

Figure 58. Rotor Orbits vs. OR Squeeze Ratio and Shaft-Inner Race Friction Coefficient

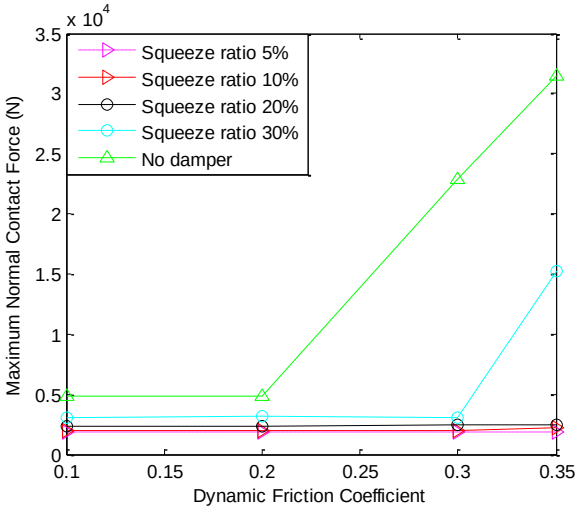

Figure 59 Maximum normal contact force vs. friction coefficient

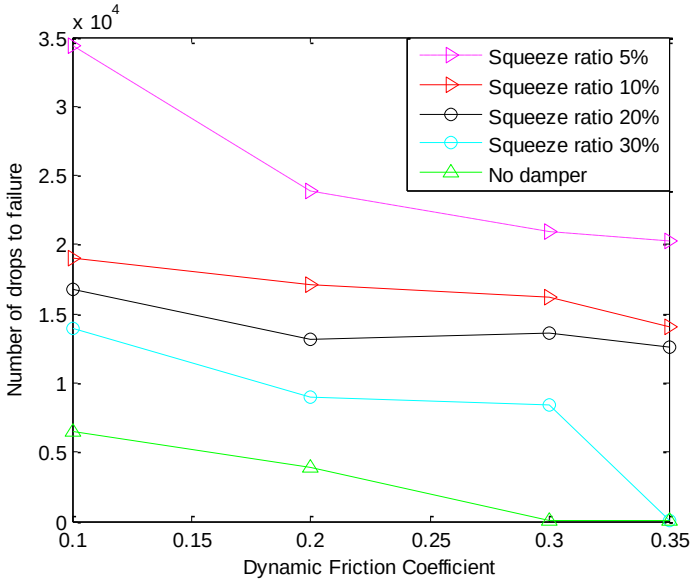

Figure 60 Number of Rotor Drops to Failure vs. OR squeeze ratio and friction coefficient.

The above discussion centers on extending the AB race life by reducing stresses and contact forces. A second mode of failure is contact between the high speed spinning rotor and the magnetic bearing stator. The AB is mounted in series with the OR so

excessive flexibility of the OR may render the AB ineffective in preventing the rotor from striking the magnetic bearing stator. Define the rotor deflection ratio as

$$r_{deflect} = \frac{d_r - C_{CB}}{C_{AMB} - C_{CB}} \tag{79}$$

where d_r is the radial displacement of the rotor, C_{CB} is the auxiliary bearing clearance and C_{AMB} is the magnetic bearing clearance. The rotor will hit the magnetic bearing if $r_{deflect}$ exceeds 1. Figure 61 shows the maximum deflection ratio over the drop event vs. dynamic friction coefficient and OR squeeze ratio. It is interesting to note that magnetic bearing-shaft impact will occur for an infinitely stiff OR (no damper) and friction coefficient greater than 0.28, and for an overly flexible OR (squeeze ratio 5%) for all friction coefficient values. The latter case emphasizes the need for a greater squeeze ratio to stiffen the OR and prevent stator-rotor impact. Too high of an OR squeeze ratio also causes impact if the friction coefficient exceeds 0.33 and squeeze ratio is 30%.

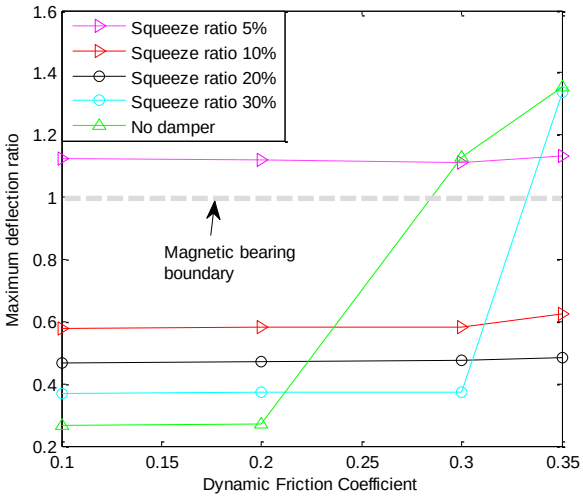

Figure 61 Maximum deflection ratios vs. OR squeeze ratio and friction coefficient

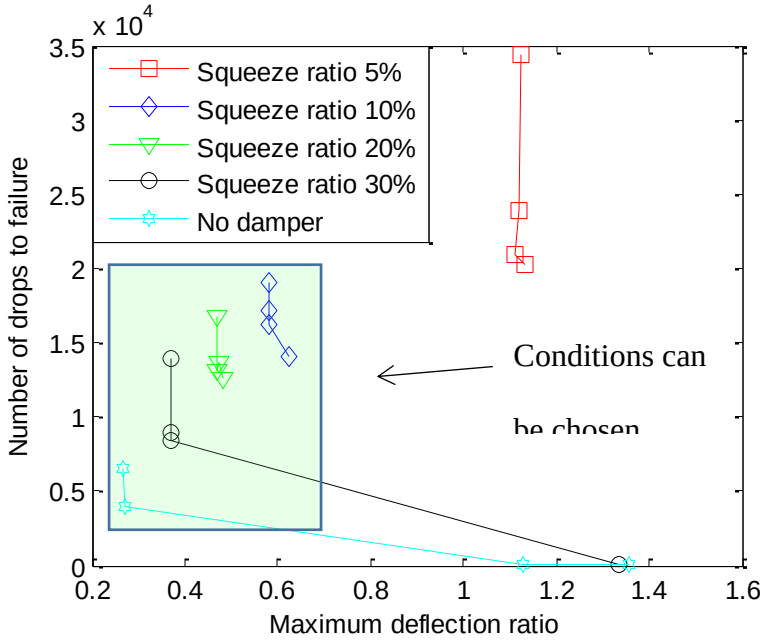

Figure 62. Co-plot of both maximum deflection ratio and life failure criteria

Figure 62 displays both life and maximum deflection ratio failure variables. This tool allows the analyst to identify designs (friction coefficient and OR squeeze ratio) that satisfy both failure criteria, i.e. cases in the green shaded block. The figure shows that designs may have similar maximum deflection ratio but significantly different fatigue life. Figure 63 shows the maximum temperature rise in the AB for various friction coefficients and OR squeeze ratios. The results show minimal temperature rise for all cases employing an OR except for the .35 friction coefficient and 30% squeeze ratio case. The determining factor for incurring a large temperature rise is the occurrence of backward whirl. The friction coefficient 0.35 – without OR case shows a temperature rise of 15^{o}C in only 1 second. The OR lessens the severity of the temperature rise for the same value of coefficient of friction.

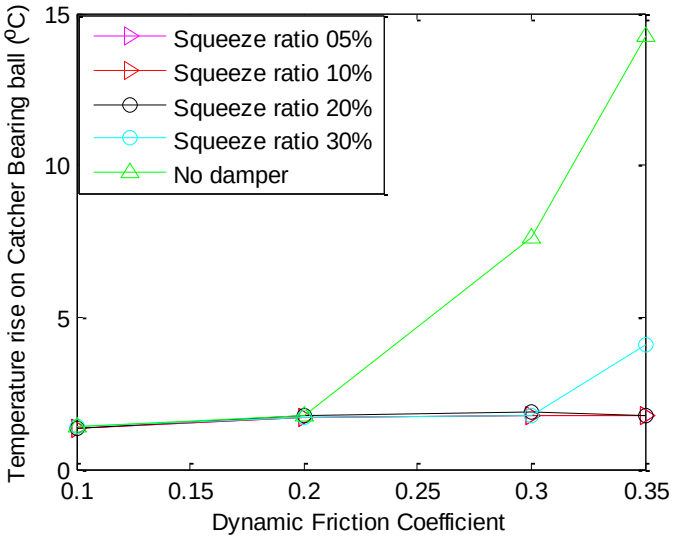

Figure 63. Temperature rise with different dynamic friction coefficients and OR squeeze ratios

5.3 Conclusion

The O-ring can successfully prevent backward whirl, thereby reducing the rotor drop contact forces, temperature rise and vibration, and increasing the auxiliary bearing inner race fatigue life. The O ring is in series with the AB ball bearing yielding a net softening of the support system. This could lead to contact of the spinning rotor with the stationary magnetic bearing. Adjustment of the squeeze ratio can stiffen the O ring providing a means to prevent rotor – magnetic bearing impact, while also mitigating backward whirl.

CHAPTER VI

HIGH FIDELITY TWO-DIMENSIONAL PLANE STRAIN SLEEVE TYPE AUXILIARY BEARING MODEL*

This chapter develops a coupled 2 dimensional elastic deformation – heat transfer finite element model of the sleeve bearing acting as a AB. A coulomb friction model is used to model the friction force between the rotor and the sleeve bearing. The contact force and 2-D temperature distribution of the sleeve bearing are obtained by numerical integration. To validate the FEM code developed by the author, firstly, the mechanical and thermal static analysis results of the sleeve bearing model are compared with the results calculated by the commercial software, "SolidWorks Simulation". Secondly, the transient analysis numerical results are compared with the rotor drop test results in reference. Additionally, this chapter explores the influences of different surface lubrication conditions, different materials on rotor-sleeve bearing's dynamic and thermal behavior. This chapter lays the foundation of the fatigue life calculation of the sleeve bearing and provides the guideline for the sleeve type AB design.

---

*This chapter has been granted the permission of using all or any part of the ASME paper "Dynamic and Thermal Analysis of Rotor Drop on Sleeve Type Catcher Bearings in Magnetic Bearing Systems" by Xiao Kang; Alan Palazzolo, J. Eng. Gas Turbines Power. 2017; 140(2) to be published by Texas A&M University Libraries/ProQuest Information and Learning Company.

6.1 Sleeve Bearing Thermal and Dynamic Finite Element Model

6.1.1 Sleeve Bearing Finite Element Model

The sleeve type Auxiliary bearing is modeled by the plane strain model. The variation in axial direction is ignored. The deformation in the cross section is analyzed. The four-node quadrilateral element is used to model the sleeve bearing. Figure 64 shows the mesh of the sleeve bearing's cross section. The nodes located outside of the surface of the sleeve bearing are supported by the radial and tangential springs as shown in Figure 64.

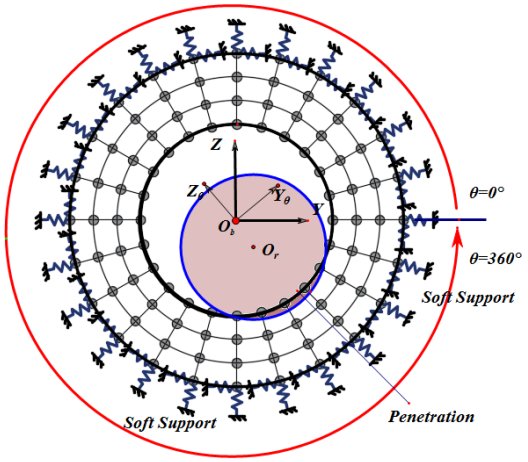

Figure 64. Plane strain model of the sleeve bearing

In the plane strain model, the relationship between strain and stress is as shown in equation (80) [21].

$$\underline{\sigma} = \underline{E}\,\underline{\varepsilon} \tag{80}$$

where $\underline{\sigma} = [\sigma_{11} \quad \alpha_{22} \quad \sigma_{12}]^T$, $\underline{\varepsilon} = [\varepsilon_{11} \quad \varepsilon_{22} \quad \varepsilon_{12}]^T$.

The material matrix in plane strain model is shown by the equation (81).

$$\underline{E}^e = \frac{E}{(1+\nu)(1-2\nu)}\begin{bmatrix} 1-\nu & \nu & 0 \\ \nu & 1-\nu & 0 \\ 0 & 0 & \frac{1-2\nu}{2} \end{bmatrix} \tag{81}$$

Since the four node quadrilateral element is used, the element stiffness matrix can be obtained as equation (82). [21]

$$K^e = t^e \int_{\Omega_e} (B^e)^T E^e B^e d\Omega_e \tag{82}$$

where $\underline{B}^e$ is the matrix in $\underline{\varepsilon}^e = \underline{B}^e \underline{u}^e$, $\underline{u}^e$ is the nodal displacement of the element, and $\underline{\varepsilon}^e$ is the strain of the element. The mass matrix is as equation (83).

$$\underline{M}^e = t^e \int_{\Omega_e} \rho (N_e)^T N_e d\Omega_e \tag{83}$$

where $\underline{N}_e$ is the shape function matrix of the four-node quadrilateral element.

The geometry of the element is mapped from its actual shape into a square. By using the Gauss Quadrature (GQ) method, the element stiffness matrix can be obtained as equation (84).

$$\underline{K}^e \approx \hat{t}^e \sum_{s=1}^{n_G} \sum_{t=1}^{n_G} w_s w_t B_e^T E_e B_w \det(J_e) \tag{84}$$

The element mass matrix can also be obtained as equation (85) :

$$\underline{M}^{e} \approx \hat{t}^{e} \sum_{s=1}^{n_G} \sum_{t=1}^{n_G} w_s w_t \rho N_s{}^{T} N_w \det(J_e) \tag{85}$$

where $\hat{t}^{e}$ is the thickness of the sleeve bearing in the axial direction. After constructing the nodal connectivity matrix, the mesh plot can be obtained as shown in Figure 65.

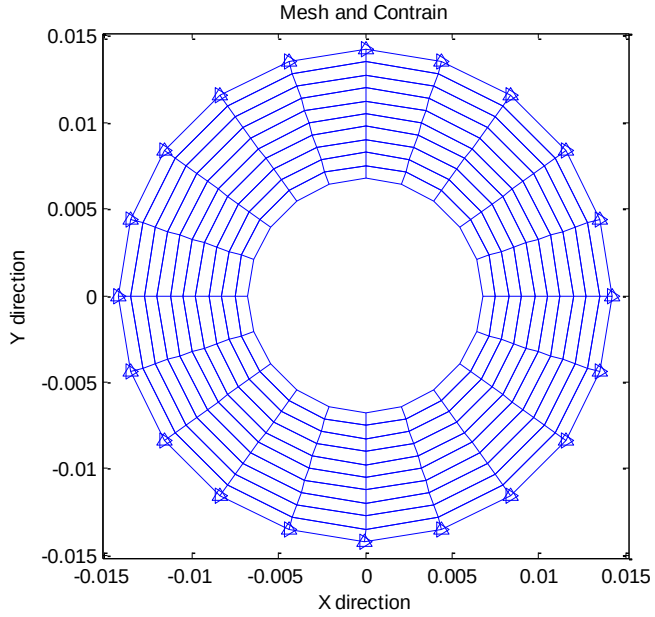

Figure 65. Mesh check in Matlab for the PS model of the sleeve bearing

The global stiffness and mass matrix are assembled based on the nodal connectivity and the nodal constraint. The proportional damping is added to the sleeve bearing model. The coefficients respect to mass matrix and stiffness matrix are calculated based on the measured damping coefficient at two different frequencies. The two frequencies are the upper bound and lower bound of its operation frequencies to guarantee the calculated damping is a conservative value [21].

$$\underline{C} = \alpha_M \underline{M} + \alpha_K \underline{K} \tag{86}$$

where the coefficients α_M and α_K can be calculated as equation (87).

$$\begin{bmatrix} \alpha_M \\ \alpha_K \end{bmatrix} = \begin{bmatrix} 1 & \omega_1^2 \\ 1 & \omega_2^2 \end{bmatrix}^{-1} \begin{bmatrix} 2\omega_1\zeta_1 \\ 2\omega_2\zeta_2 \end{bmatrix} \tag{87}$$

6.1.2 Sleeve Bearing Thermal Model

The governing equation for the transient heat transfer in the plane system is as equation (88),

$$C_T \rho \frac{dT}{dt} - \frac{\partial}{\partial x}(k_x \frac{\partial T}{\partial x}) - \frac{\partial}{\partial y}(k_y \frac{\partial T}{\partial y}) + \beta(T - T_\infty) = \hat{q}_n \tag{88}$$

where k_x and k_y are thermal conductivities [in W/(m.^{o}C)] along the x and y directions. β is the convective heat transfer coefficient. After obtaining the weak form, substitute the finite element approximation as equation (89).

$$T = \sum_{j=1}^{n} T_j^e N_j^e \tag{89}$$

The finite element model is obtained as equation (90).

$$\sum_{j=1}^{n} C_T M_{ij} \dot{T}_j^e + \sum_{j=1}^{n} (K_{ij}^e + H_{ij}^e) T_j^e = F_i^e + P_i^e \tag{90}$$

The element stiffness matrix can be formed as equation (91).

$$K^e_{ij} = \int_{\Omega_e} (k_x \frac{\partial N_i^e}{\partial x} \frac{\partial N_j^e}{\partial x} + k_y \frac{\partial N_i^e}{\partial y} \frac{\partial N_j^e}{\partial y}) dxdy \tag{91}$$

The thermal source vector is described as equation (92),

$$F_i^e = \int_{\Omega_e} fN_i^e dxdy + \oint_{\Gamma_e} q_n^e N_i^e ds = f_i^e + Q_i^e \tag{92}$$

P_i and H_{ij} are the terms related to the heat convection.

$$H_{ij} = \beta^e \int_{\Gamma} \psi_i^e \psi_j^e ds \tag{93}$$

$$P_i^e = \beta^e \int_{\Gamma_e} \psi_i^e T_\infty ds \tag{94}$$

When using the 4-node iso. quadrilateral element, the element stiffness matrix is changed as equation (95).

$$K^e_{ij} = \int_{-1}^{1}\int_{-1}^{1} (k_x \frac{\partial N_i^e}{\partial x} \frac{\partial N_j^e}{\partial x} + k_y \frac{\partial N_i^e}{\partial y} \frac{\partial N_j^e}{\partial y}) \det(\mathbf{J}) d\zeta d\eta \tag{95}$$

Thus, the element stiffness matrix can be obtained as equation (96).

$$\mathbf{K}^e = \int_{-1}^{1}\int_{-1}^{1} (k_x \mathbf{H}_x{}^T \mathbf{H}_x + k_y \mathbf{H}_y{}^T \mathbf{H}_y) \det(\mathbf{J}) d\zeta d\eta \tag{96}$$

Here $\mathbf{H}_x$ and $\mathbf{H}_y$ can be found in the appendix.

Then use the "Gauss Quadrature" method to conduct the numerical integration as equation (97).

$$\mathbf{K}^e = \sum_{s=1}^{n_G}\sum_{s=1}^{n_G} (k_x \mathbf{H}_x{}^T(\zeta_s,\eta_s)\mathbf{H}_x(\zeta_s,\eta_s) + k_y \mathbf{H}_y(\zeta_s,\eta_s)^T \mathbf{H}_y(\zeta_s,\eta_s)) \det(\mathbf{J}) \tag{97}$$

The thermal mass is solved as equation (98).

$$\mathbf{M}^e = \int_{-1}^{1}\int_{-1}^{1} C_T \rho \mathbf{N}^T \mathbf{N} \det(\mathbf{J}) d\zeta d\eta \tag{98}$$

Here, $\mathbf{N}$ is the shape function matrix; C_T is the specific heat; ρ is the material density.

In the current model, only edge 4-1 (node 4 to node 1 in the local element) in the first layer of the element in radial direction has the heat convection boundary conditions. For those elements, the detailed boundary conditions are as equation (99),

$$H_{41}^e = \frac{\beta_{41}^e h_{41}^2}{6}\begin{bmatrix} 2 & 0 & 0 & 1 \\ 0 & 0 & 0 & 0 \\ 0 & 0 & 0 & 0 \\ 1 & 0 & 0 & 2 \end{bmatrix} \tag{99}$$

which will be assembled in the global thermal stiffness matrix. Also, P_i^e, expressed as equation (100), will be assembled into the global thermal load vectors.

$$P_i^e = \frac{\beta_{41}^e T_\infty h_{41}^e}{2}\begin{bmatrix} 1 \\ 0 \\ 0 \\ 1 \end{bmatrix} \tag{100}$$

The heat power generated by the friction between the surfaces of the rotor and the sleeve bearing will be explained in the section "contact model between rotor and sleeve bearing".

6.1.3 Thermal Expansion Calculation

The procedure described in this section calculates the thermal load caused by thermal expansion. Those thermal loads will be applied on the nodes of each element. Ignoring the axial deformation, the thermal stress in the plane strain (PE) model can be evaluated as equation (101).

$$\underline{\sigma}_0 = \frac{-E\alpha\Delta T}{1-2\nu}\begin{bmatrix}1 & 1 & 0\end{bmatrix}^T \tag{101}$$

In plane strain model, the material matrix is shown as equation (81).

Assuming the bearing is under uniform expansion and without angular distortions, the thermal stress is as equation (102).

$$\underline{\sigma}_0 = \frac{-E\alpha\Delta T}{1-2\nu}\begin{bmatrix}1 & 1 & 0\end{bmatrix}^T \tag{102}$$

The equation of motion of the sleeve bearing can be derived as equation (103).

$$\underline{M}_B\ddot{\underline{X}}_B + \underline{K}_B\underline{X}_B + \underline{C}_B\dot{\underline{X}}_B = \underline{F}_{Thermal} + \underline{F}_Q \tag{103}$$

where $\underline{F}_Q$ is the contact load from the rotor.

The thermal load $\underline{F}_{Thermal}$ caused by the thermal expansion is calculated as equation (104).

$$\underline{F}_{Thermal} = \int_\Omega \underline{B}_e{}^T \underline{E}_e \underline{\varepsilon}_0 d\Omega = \int_\Omega \underline{\sigma}_0 \underline{B}_e d\Omega = \int_\Omega \underline{\sigma}_0 \underline{D}_e \underline{N}_e d\Omega \tag{104}$$

Using the Guess Quadrature integration, the thermal load can be derived as equation (105),

$$\underline{F}_{Thermal} = t^e \sum_{s=1}^{n_G}\sum_{t=1}^{nG} w_s w_t \underline{\sigma}_0 \underline{B}_e(\zeta_{1s},\zeta_{2t})\det(\underline{J}_e(\zeta_{1s},\zeta_{2t})) \tag{105}$$

which is updated at each time step based on the temperature variation.

6.1.4 Contact Between Rotor and Sleeve Bearing

The key thing for the rotor drop analysis is to model the contact between the rotor and the sleeve bearing as shown in Figure 64.

Here the rotor is built by the Timoshenko beam model. The equation of motion of the rotor is shown as equation (106),

$$\underline{M}_r \ddot{\underline{X}}_r + [\underline{C}_r + \Omega \underline{G}]\dot{X}_r + \underline{K}_r \underline{X}_r = \underline{F}_r \tag{106}$$

where $\underline{M}_r$ is the mass matrix of the rotor, C_r is the damping matrix, G is the gyroscopic matrix and K_r is the shaft stiffness matrix. The vector $\underline{X}_r$ contains the information of the nodal degree of freedom. F_r is the load vector including the imbalance force and the nonlinear Auxiliary bearing forces. Ω is the angular velocity of the rotor. Each beam node has six degree of freedoms.

The rotor surface is regarded to be rigid. The local radial and tangential penetration of each surface node can be calculated by the coordinate transformation. When contact occurs, the penalty spring is connected between the rotor and surface nodes of the sleeve bearing. The stiffness of the penalty spring is set as 10000 times larger than the maximum element of the stiffness matrix of the sleeve bearing [22]. The total contact force is the summation of the total force at each node. The local normal contact force for each surface node is as equation (107). Please note that the contact force can only be calculated when the value of the local radial penetration δ_i is positive, otherwise they are zero.

$$F_{ni} = K_p \delta_i \tag{107}$$

$$F_{ti} = \mu_{sb} F_{ni} \tag{108}$$

The μ_{sb} can be calculated by the Stribeck friction model as shown in equation (109)

.

$$\mu_{sb} = -\frac{2}{\pi}\arctan(\varepsilon_f v_{rel})[\frac{\mu_s - \mu_d}{1+\delta_f |v_{rel}|} + \mu_d] \tag{109}$$

where v_{rel} is the relative tangential velocity between node *i* of the sleeve bearing surface and the corresponding rotor contact surface. The parameter ε_f determines the slope of the approximation function. The parameter δ is a positive number that determines the rate at which the static friction coefficient approaches by the dynamic friction coefficient with respect to relative velocity. The term '$-2/\pi \arctan(\varepsilon f v_{rel})$' has the same function as the "sign" function. But this term, according to reference 6, has better performance for the numerical stability, and can agree well with the experimental data as well.

The total force act on the rotor can be calculated as equation (110).

$$\underline{F}_{total} = \sum_{i=1}^{n} \underline{T}_i \underline{F}_i \tag{110}$$

Where:

$$\underline{F}_{total} = \begin{bmatrix} F_y \\ F_z \end{bmatrix};\ \underline{T}_i = \begin{bmatrix} \cos\theta_i & \sin\theta_i \\ -\sin\theta_i & \cos\theta_i \end{bmatrix};\ \underline{F}_i = \begin{bmatrix} F_{ni} \\ F_{ti} \end{bmatrix}$$

The penetration value δ_i correspond to each surface node of AB can be calculated as equation (111)

$$\begin{aligned} \delta_i = {} & y_{rotor}\cos\theta_i + z_{rotor}\sin\theta_i \\ & - clearance - (y_i \cos\theta_i + z_i \sin\theta_i) \end{aligned} \tag{111}$$

The heat power generated from the friction between the rotor and the Auxiliary bearing surface is obtained as equation (112) .

$$P_{fi} = F_{ti} v_{irel} \tag{112}$$

The heat power in equation (112) will be assembled in the global thermal load vector.

6.2 Validation of the Mechanical and Thermal Model

To validate the plane strain FEM model in this paper, the static analysis results calculated by the author are compared with the results from the SolidWorks mechanical, a widely used commercial software. In the SolidWorks model, the sleeve bearing is constructed as a 3D model which is meshed by the 3D element. Here the basic geometry and material information of the sleeve bearing is as Table 11.

Table 11: Material and geometry parameters for sleeve bearing [9]

Young's modulus (GPa)	110
Poisson ratio	0.33
Density (kg/m^3)	8300
Inner diameter (m)	0.08
Outer diameter (m)	0.15
Mesh in radial direction	10
Mesh in circumferential direction	50

In the static analysis, for the plane strain model, a nodal force is applied in the horizontal direction of node 1 as shown in Figure 66. For the SolidWorks model, the force

(with the same direction) is a linear distributed force whose summation is same as the nodal force in the plane strain model as shown in Figure 66.

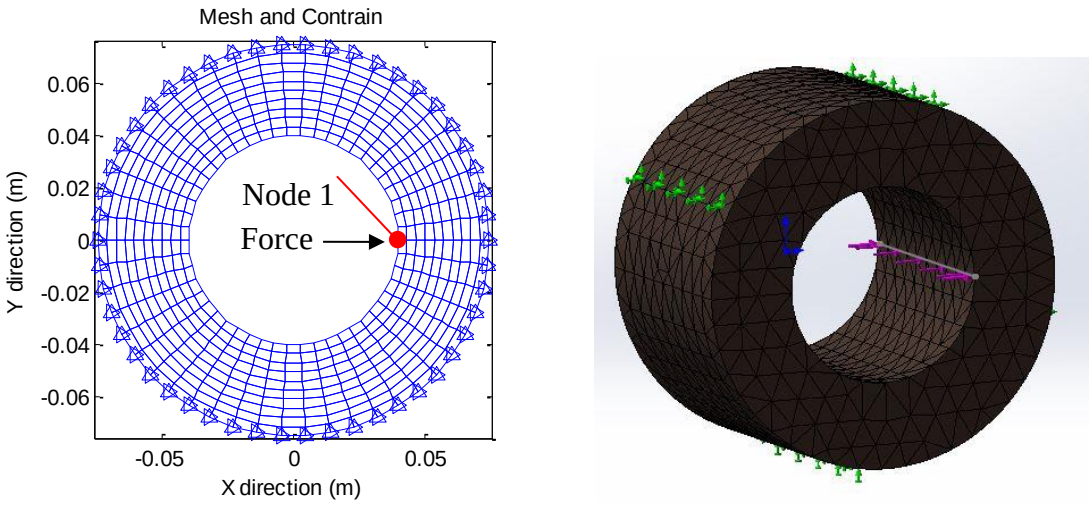

a.Plane strain model by author b. SolidWorks 3D element model
Figure 66. Mesh, constrain and force direction

Figure 67 shows the curve about the displacment of the node 1 vs. the value of applied force. The red line represents the results from author's plane strain model. The dash line represents the results from the SolidWorks. The results in Y direction are very close, the maximum difference is about 3%. It indicates the direct stiffness of the plane strain model is reliable. There are some difference between the displacement in Z direction, which maybe caused by the difference in mesh geometry. Such difference may be reduced by finer mesh. But due to the relative small value of the displacement, it will not influence much for the dynamic response.

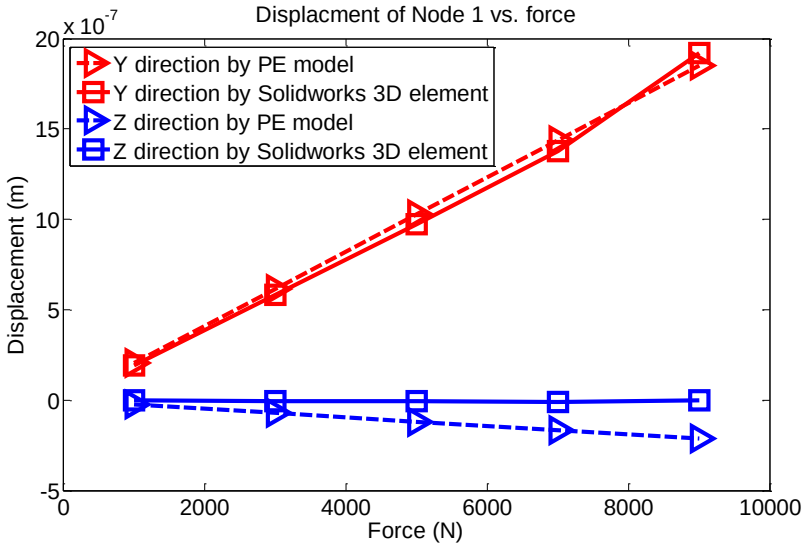

Figure 67. Displacements of Node 1 vs. applied force

To validate the thermal model of the sleeve bearing, the static analysis results obtained by the 2D thermal code in this paper are compared with the results calculated by SolidWorks. The thermal conductivity and convection coefficients are shown in Table 12.

Table 12. Thermal property for the bronze sleeve bearing [9]

Specific heat ($J/kg\cdot^{o}C$)	380
Thermal conductivity ($W/(m.^{o}C)$)	47
Thermal expansion ratio ($1/^{o}C$)	1.80E-05
Heat convection coefficient ($W/(m^{2}\cdot^{o}C)$)	20
Ambient temperature (^{o}C)	25

A heat source is applied on a node as shown in Figure 66. A similar linear distributed heat source with the same sum value is applied on the edge of the SolidWorks' 3D model as shown in Figure 68.

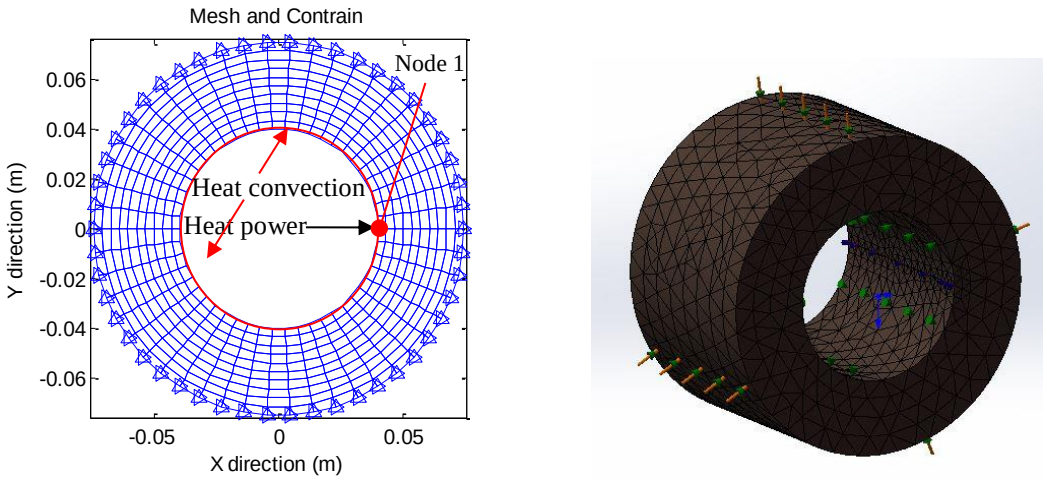

a.2D thermal model by author b. SolidWorks 3D element model

Figure 68. Mesh, constrain and heat source

In this validation model, the temperature of the outside boundary is prescribed as the ambient temperature 25°C. The inner boundary is applied heat convection boundary condition with the convection coefficient of $20\,W/(m^2\cdot^{O}C)$. Here the temperature of node 1 in FEM model in this paper is compared with the temperature of the node locate the middle of the edge of applied heat source in the SolidWorks 3D model. The results are shown in

Figure 69.

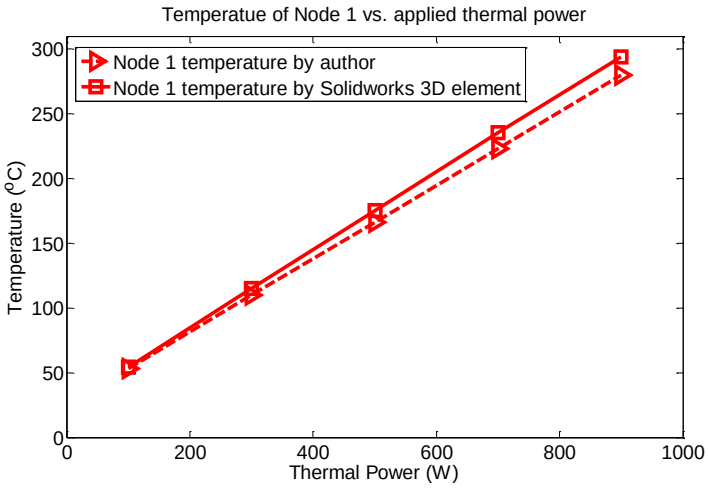

Figure 69. Temperature of Node 1 vs. applied heat

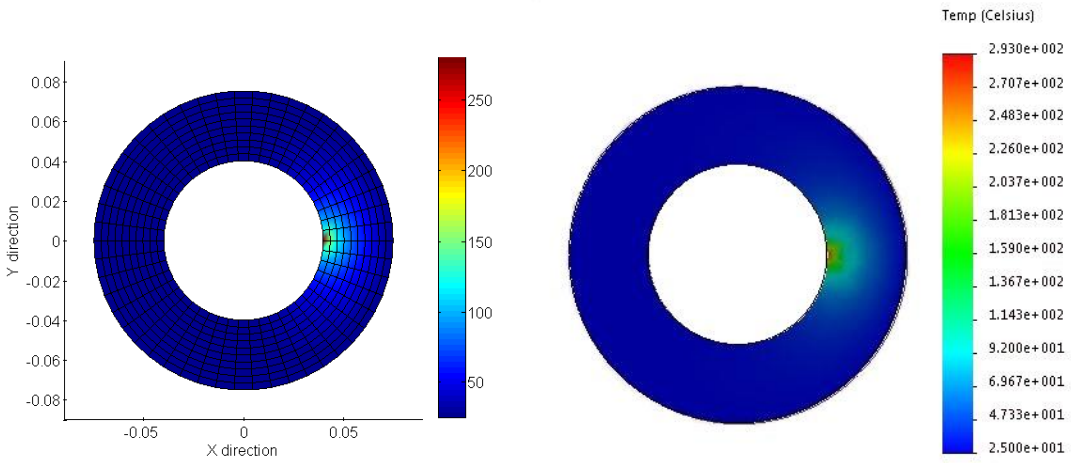

(a) (b)

Figure 70. Temperature distribution when the applied heat power is 900W, (a). 2D FEM thermal model by author. (b). 3D FEM model by SolidWorks Simulation

Figure 69 shows that the plot about maximum temperature vs. sum heat power. The red line represent the 2D temperature model in the paper, the blue line shows the results in SolidWorks. The results appear quite similar. Figure 70 shows under the same

total heat power, the temperature distribution are similar. The comparison in this section shows that the 2D thermal model in this section is reliable.

6.3 Experiment Validation

The simulation results using the sleeve bearing model in this paper are compared with the experiment data in reference [14]. In reference [14], Swanson et al carried out a drop test using the test rig which initially aims to simulate a gas turbine compressor section [14]. In this rig, the rotor is supported by two AMBs which are located at node 2 and node 12 as shown in Figure 71. During the drop test, only the drive end AMB is de-energized while the AMB at the non-drive end is still working.

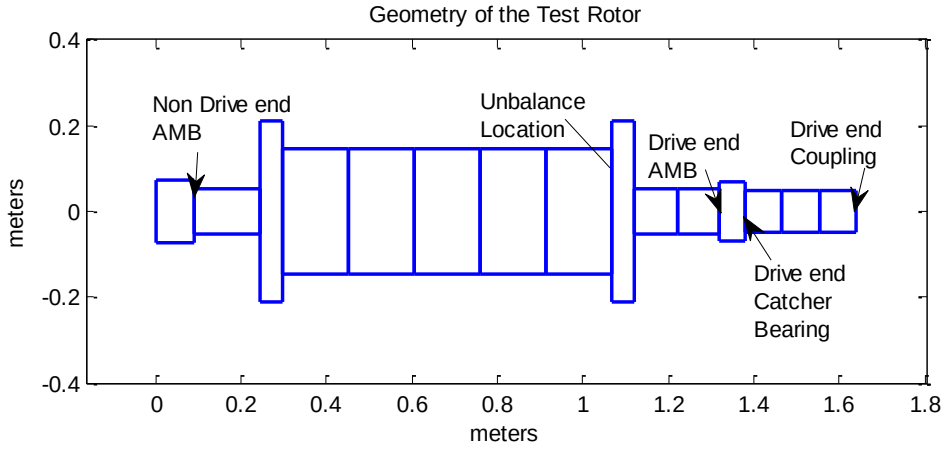

Figure 71. Rotor geometry in reference [13]

According to the reference 13, the magnetic bearing stiffness is 7.15e6N/m and the damping is 1e4N-s/m, which are obtained by the frequency dependent stiffness and damping curves provided by the manufacture [14]. The imbalance of the rotor is added at the node 9 as shown in Figure 71. Swanson et al. tested rotor drop onto lubricated and

unlubricated bronze type sleeve bearing. He also did drop tests with or without rotor imbalance. The rotor's rotational direction in the test is clock-wise [14].

To compare the test results in reference [14], the author builds a dynamic-thermal coupled 2D numerical model based on the test rig information provided by the reference [14]. The results of the numerical model are compared with the reference's test data. The parameters in the simulation model are shown in Table 13.

Table 13. Parameters in the 2D numerical model

AB Young's modulus (GPa)	110
AB Poisson ratio	0.33
AB Density (kg/m^3)	8300
AB Inner diameter (m)	0.15
AB Outer diameter (m)	0.19
AB Mesh in radial direction	2
AB Mesh in circumferential direction	28
Auxiliary Bearing Clearance (mm)	0.25
AMB Stiffness (N/m)	7.15e6N/m
AMB Damping (N.s/m)	1.0e4N.s/m
Rotor drop spin speed (RPM)	4000
Auxiliary Bearing Proportional Damping Coefficient	0.01

For the rotor dropping onto the lubricated bronze sleeve bearing, the dynamic friction coefficient is chosen as 0.15 according to reference 13. The imbalance value is 0.25kg-mm which is placed on the node 9 of the rotor. The numerical and test results are as shown in Figure 72.

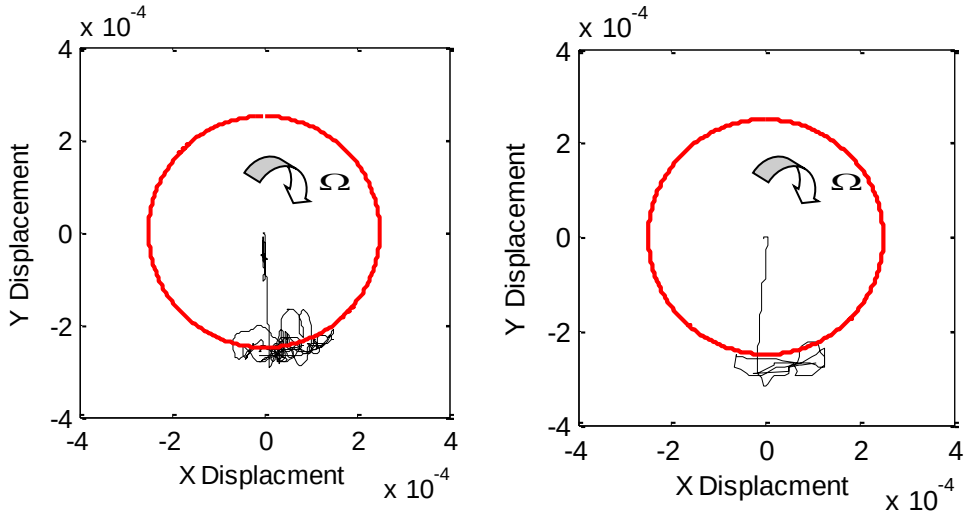

(a) Simulation results (b) Test results

Figure 72. Rotor drop onto lubricated bronze type sleeve bearing with low imbalance

As shown in Figure 72, the simulation results and the experiment results have the similar trend that both of the rotors slide on the right side of the bottom of the sleeve bearing after a few bounces. Additionally, there is no reverse or forward whirl occurring.

For the rotor dropping onto the unlubricated bronze sleeve bearing, the dynamic friction coefficient is chosen as 0.3 based on reference 13. The imbalance value is 0.25kg-mm which is placed at node 9. The numerical and test results are presented in Figure 73.

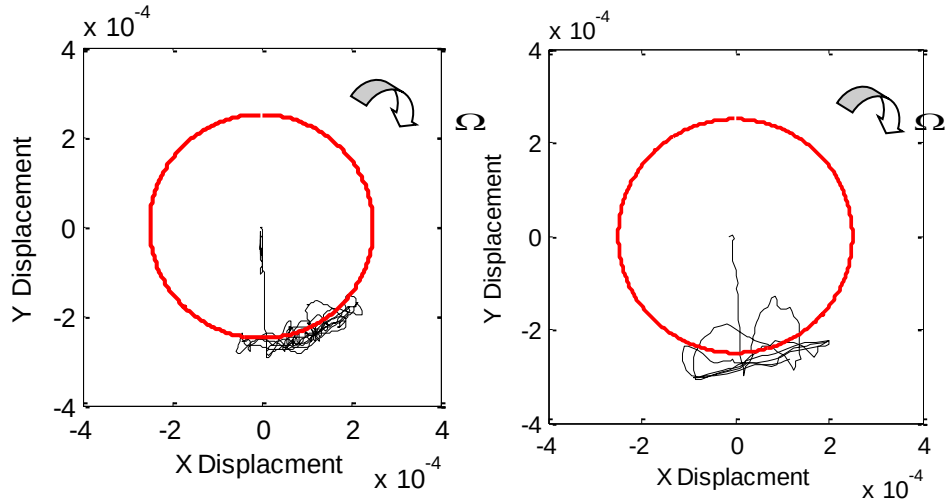

(a) Simulation results (b) Test results

Figure 73. Rotor drop onto unlubricated bronze type sleeve bearing with low imbalance

According to Figure 73, when the sleeve bearing is not lubricated, both the simulation and experiment results show that the rotor has larger vibration compared with the case with lubricated sleeve bearing.

For the rotor dropping onto the unlubricated bronze sleeve bearing with high imbalance value, the dynamic friction coefficient is chosen as 0.3 according to reference 13. The imbalance value is 2.73kg-mm which is placed at node 9. The numerical and test results are as Figure 74.

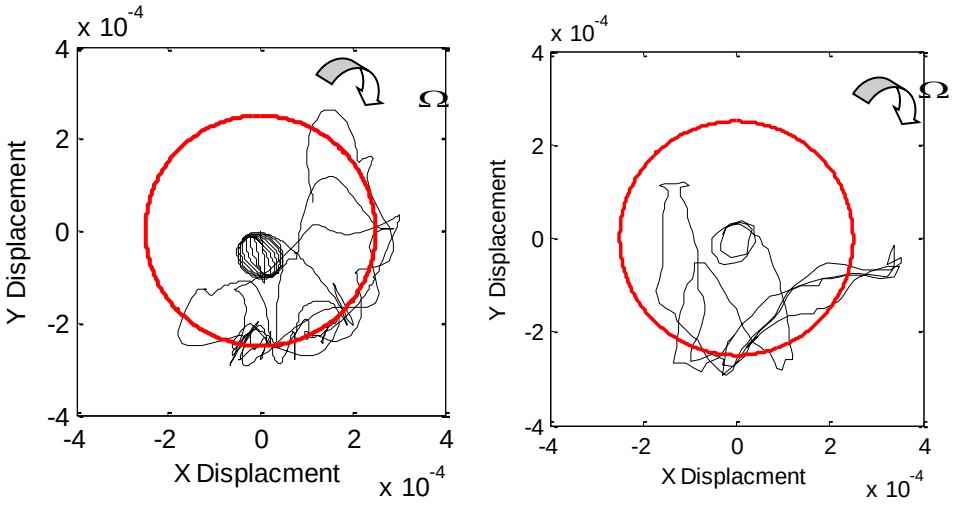

(a) Simulation results (b) Test results

Figure 74. Rotor drop onto unlubricated bronze type sleeve bearing with high imbalance

In the simulation, the rotor has the trend of resulting in the reverse whirl. While there is no reverse whirl occurring in the experiment. The difference may be caused by the difficulty in accurately estimating the housing stiffness and the exact friction coefficient.

For the rotor dropping onto the lubricated bronze sleeve bearing with high imbalance value, the dynamic friction coefficient is chosen as 0.15 according to the reference 13. The imbalance, with the value of 2.73kg-mm, is placed at node 9. The numerical and test results are as Figure 75.

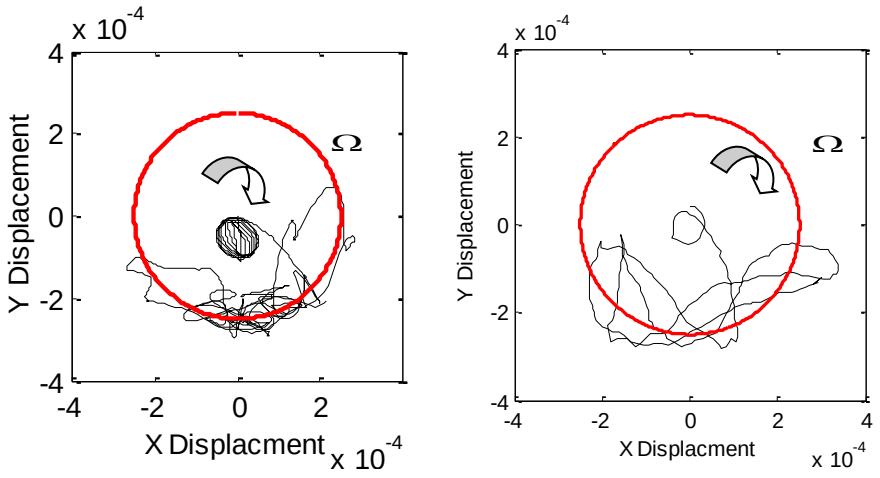

(a) Simulation results (b) Test results

Figure 75. Rotor drop onto lubricated bronze type sleeve bearing with high imbalance

Generally speaking, the simulation results qualitatively agree with the experiment data from Swanson's paper. Some reasons that may explain the discrepancy include: (1) the friction coefficients that are used are the recommended values by Swanson et al [34] and have uncertainty, (2) though the sleeve bearing is hard mounted, the housing's flexibility will still influence the penetration and contact force, (3) the test sensor may not have been exactly located at the Auxiliary bearing's location. Because only one AMB is de-energized, the rotor will have conical motion which will make the penetration looks different if the sensor was not located at the same position as the AB. Swanson et al provided an excellent benchmark for vibration correlation but did not include contact force and the temperature. Thus, other experiments with the capability of measuring the forces and the temperatures are required for the further validation of the current dynamic-thermal coupled FEM model.

6.4 Influence of Dynamic Friction Coefficient of the Sleeve Bearing Contact Surface

The influence of the dynamic friction coefficient of the sleeve bearing surface on the rotor drop event is analyzed. Different from the former validation sections, because the transient calculation will spend much simulation time, the mesh density is reduced to 24 in circumferential direction and 2 in radial direction to increase the calculation efficiency. Additionally, the rotor is replaced by a symmetric rotor so as to further reduce the calculation time. The rotor is same as the rotor in [5]. According to the sensitivity analysis of the mesh density, there will be about 10% difference with the results from SolidWorks in mechanical static analysis. However, it is enough to see the trend of the influences by the friction coefficient. The geometry, material and thermal parameters of the sleeve bearing are shown in Table 11. The stiffness is selected as 4.6e7N/m for each support spring, while the damping for each support spring is chosen as 278N.s/m. The Auxiliary bearing clearance is set to be 0.3mm in this section. The material of the rotor is steel and its geometry is shown in Figure 76. The rotor is 1 meter long. The largest diameter is 0.2m. When the rotor drops, the rotational speed is 10,000 rpm.

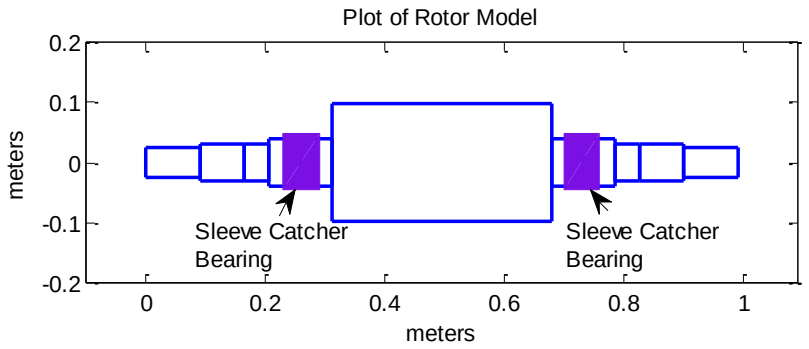

Figure 76. Rotor geometry and Auxiliary bearing location

The transient simulation period in this simulation is 0.2s. Let the friction coefficient vary from 0.15 to 0.4. Figure 77 shows the rotor orbits with different friction coefficients. It can be seen that when the friction coefficient rises to 0.4, the rotor starts to have reverse whirl. Then the penetration becomes very large (0.3mm).

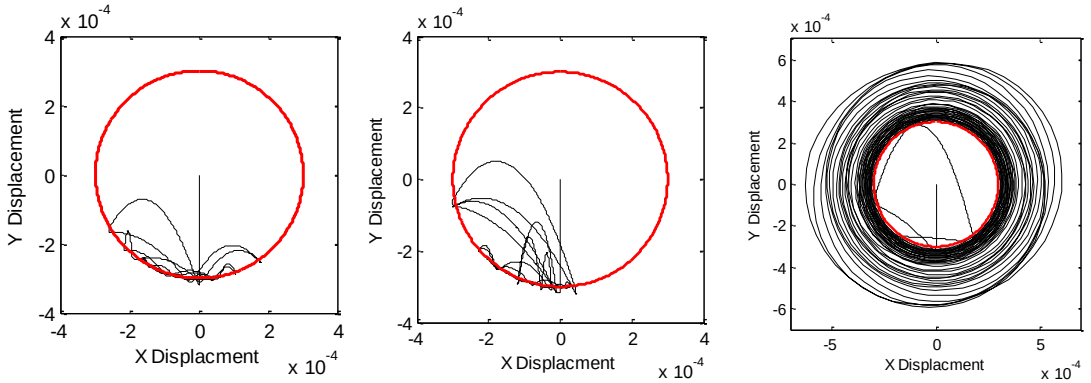

(a). $\mu_d = 0.15$ (b). $\mu_d = 0.3$ (c). $\mu_d = 0.4$

Figure 77. Rotor orbit with different dynamic friction coefficients

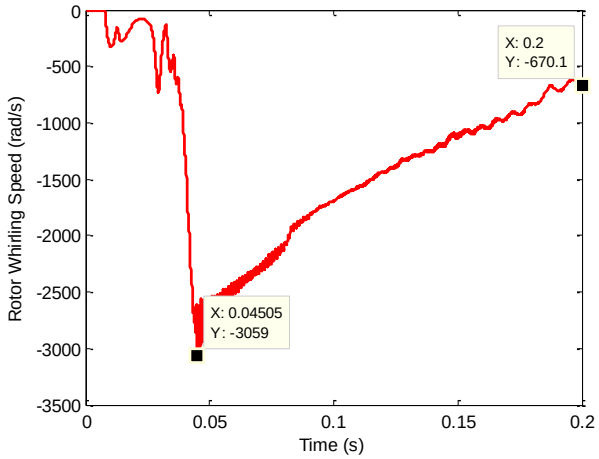

Figure 78. Rotor whirling speed when the friction coefficient is 0.4

Figure 78 shows reverse whirl with a coefficient of friction of 0.4. The whirling speed initially reaches about -3059 rad/s and then decays to about -670 rad/s at 0.2s.

Figure 79 shows the time histories of the normal contact forces and the tangential forces with different friction coefficients. When the reverse whirl occurs, the normal contact forces are greatly increased, which can reach more than 10 times of the cases without reverse whirl. The contact force greatly decays when the rotor whirling speed decays for the reverse whirl case. So the high contact forces are caused mainly by the large whirling speed.

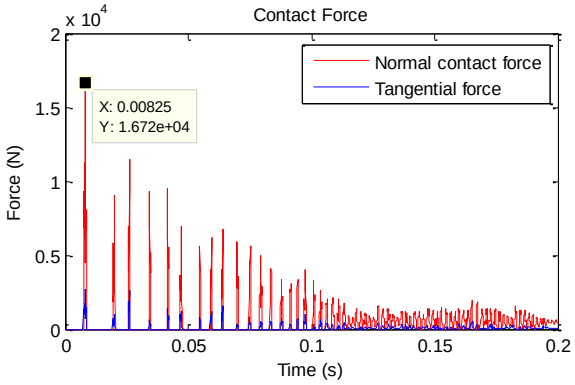

(a). $\mu_d = 0.15$

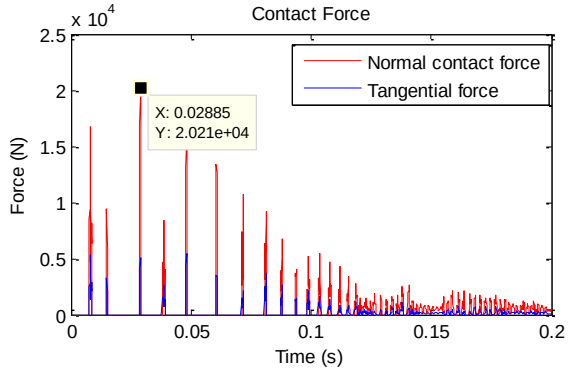

(b). $\mu_d = 0.3$

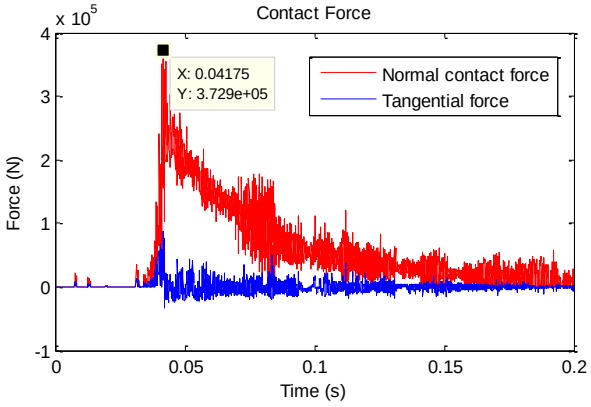

(c). $\mu_d = 0.4$

Figure 79. Contact force with different friction coefficients

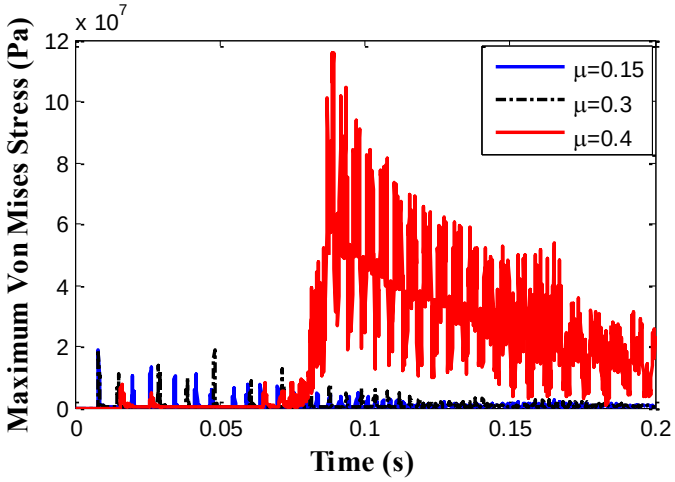

Figure 80. Maximum Von-Mises stress time history with different friction coefficients

Figure 80 shows the time history of the maximum Von Mises stress with different friction coefficients. Figure 81 shows the Von Mises stress distributions when the peak Von Mises stress occurs during the time span. The maximum Von Mises stress is seen to dramatically increase when the increased friction coefficient becomes sufficient to induce reverse whirl. The reverse whirl state stress is about 120MPa, which is near the yield stress of the material (144Mpa) [23]. Note the rotor and the AB clearances are the same as those in reference 5. For the sleeve bearing, the maximum Von Mises stresses are about 18.98Mpa, 18.96Mpa and 120Mpa, which are much smaller than the stress value (more than 1000Mpa) in reference 5 when using ball bearing type AB and under similar lubrication conditions.

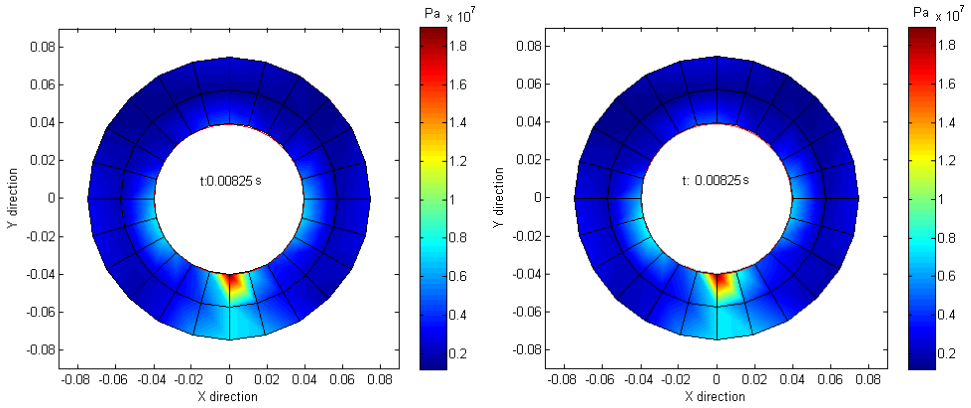

(a). $\mu_d = 0.15$ (b). $\mu_d = 0.3$

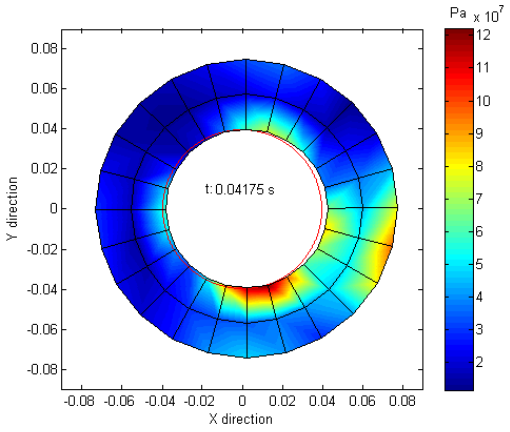

(c). $\mu_d = 0.4$

Figure 81. Von Mises Stress distribution when the largest Von Mises Stress occurs

Figure 82 shows the time histories of the peak temperature with different friction coefficients. It shows that the temperature increases quickly as the coefficient of friction increases, especially when there is reverse whirl. However, for the reverse whirl case, the sleeve bearing quickly reaches a peak temperature, and then the temperature starts to decay. It is possible that the rotor's rotational speed drops fast and the rotor starts rolling and the friction force will be small when the rolling occurs. For the cases without reverse whirl,

the rotor's spin speed decays slowly and the rotor is sliding on the sleeve bearing surface. This will generate more heat than the rolling condition. It can be seen in Figure 19 that the temperatures for the sleeve bearings without reverse whirl continue growing and gradually getting exceeds the peak temperature of the case with reverse whirl.

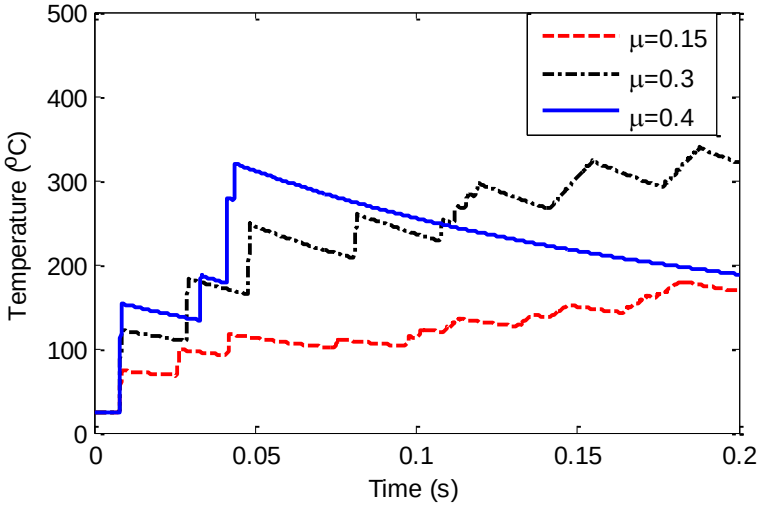

Figure 82 Time histories of peak temperature with different friction coefficients

Figure 83 shows the temperature distribution when the sleeve bearing reaches to the peak temperature during the first 0.2 second transient period under different lubrication conditions. It can be seen that when there is no reverse whirl, the peak temperature increases with the friction coefficient and the highest temperature occurs around the contact zone. When reverse whirl happens, the temperature is almost evenly distributed.

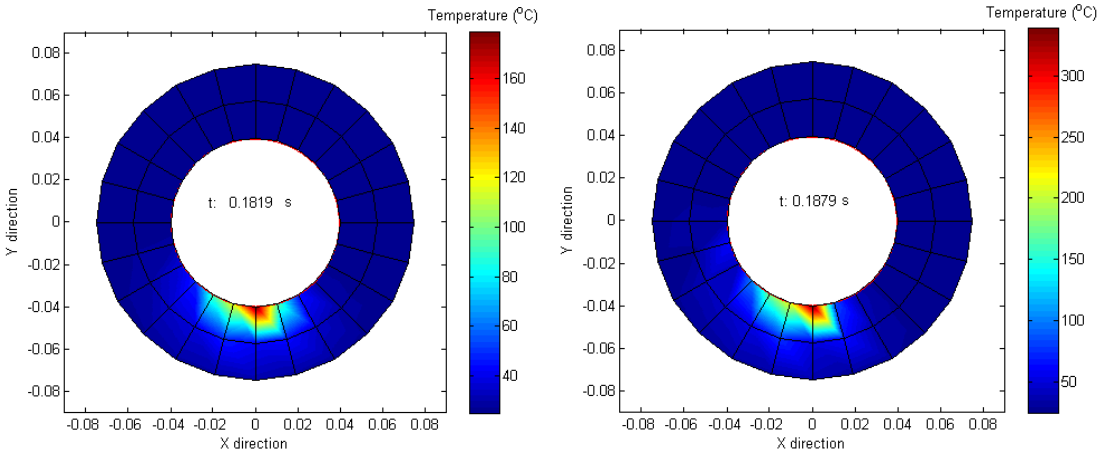

(a). $\mu_d = 0.15$ (b). $\mu_d = 0.3$

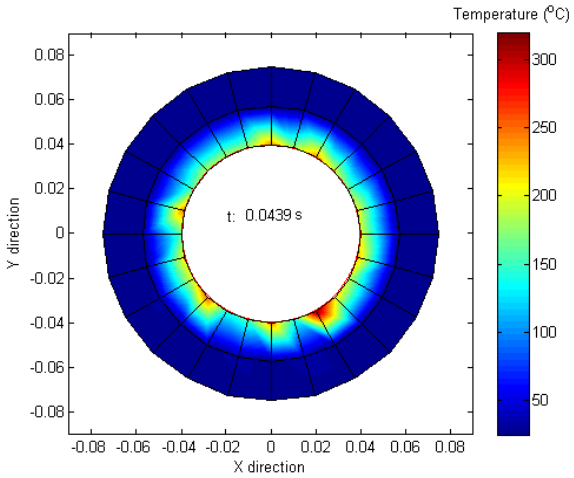

(c). $\mu_d = 0.4$

Figure 83. Temperature distribution with different friction coefficients

6.5 Influence of Sleeve Bearing Material

Three types of commonly used materials are simulated to investigate their influences on the rotor drop event. These materials include stainless steel, bronze and aluminum. Their mechanical and thermal properties are shown in Table 14. Here the dynamic friction coefficients are selected based on [23] and [24]. All the materials are

assumed to be unlubricated. Here the friction coefficient of the aluminum AB is 0.61, while the friction coefficients of the steel AB and the bronze AB are 0.5 and 0.3 [23] and [24] respectively.

Table 14. Material Properties

Material properties	**Bronze**	**Stainless Steel**	**Aluminum**
Young's modulus (GPa)	110	189.6	71.7
Poisson ratio	0.33	0.28	0.34
Density (kg/m^3)	8300	7800	2800
Specific heat ($J/kg \cdot K$)	380	477	875
Thermal conductivity ($W/(m.K)$)	47	14.9	177
Thermal expansion ratio ($1/K$)	1.80E-05	3.91E-05	7.30E-04
Friction coefficient (unlubricated)	0.3[13]	0.5[10]	0.61[10]
Support Spring Stiffness (N/m)	4.6e7	4.6e7	4.6e7
Support Spring Damping (N.s/m)	278	278	278

Figure 84 shows the rotor orbits with three different Auxiliary bearing materials. It can be seen that reverse whirl occurs for the aluminum and steel type sleeve bearings, due to their relatively large friction coefficients. Figure 84 shows that aluminum has the largest maximum penetration which is 0.338mm while for bronze the maximum penetration is only 0.0187mm.

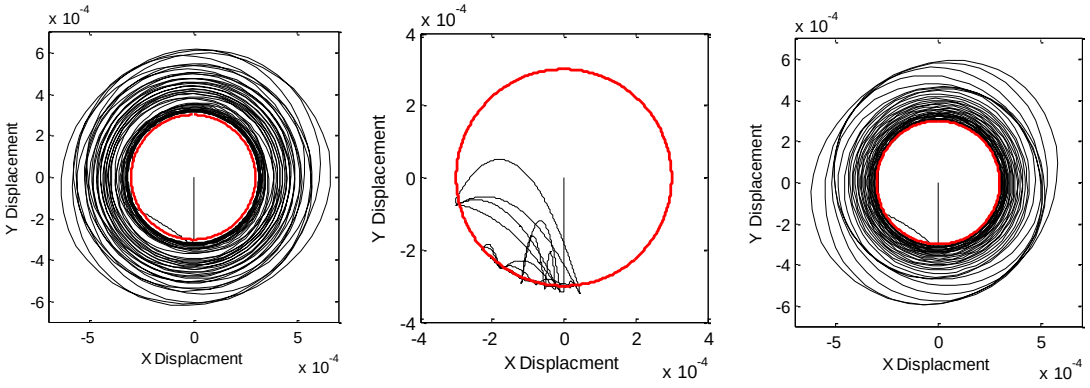

(a)Aluminum (b) Bronze (c) Steel

Figure 84. Rotor orbits with different materials

Figure 85 shows the variations of the whirling speeds of the aluminum and steel. It can be seen that both of them have negative whirling speeds. They first reach a very high peak value and then start to decay, with the peak whirling speed of the steel (3342rad/s) is being higher than the aluminum (3035rad/s). Note such whirling speeds are much larger than the rotor's rotational spin speed.

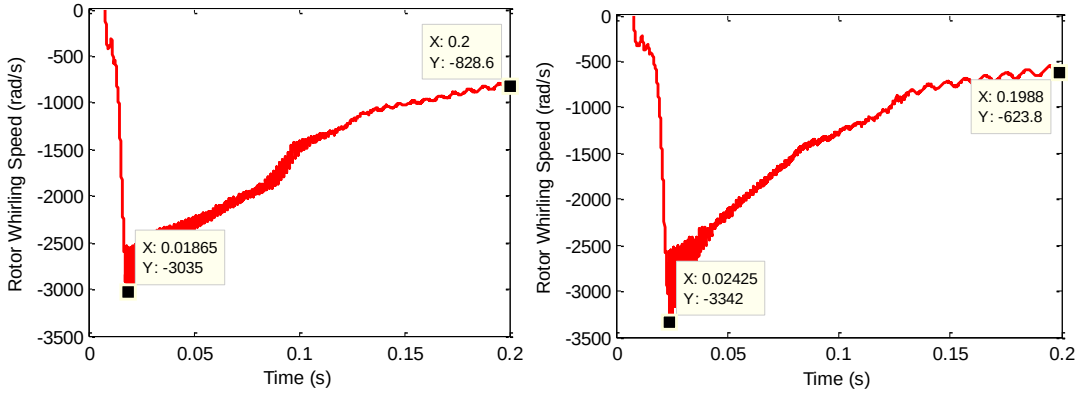

(a) Aluminum (b) Steel

Figure 85 Rotor whiling speed

Figure 86 shows the normal contact force with different Auxiliary bearing materials. It shows that the steel type AB has the largest maximum normal contact force

which is 1.905e6N while the maximum normal contact forces of the aluminum and the bronze type AB are 3.854e5N and 2.021e4N respectively.

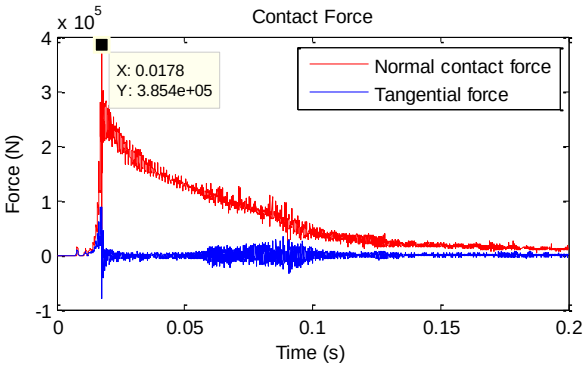

(a) Aluminum

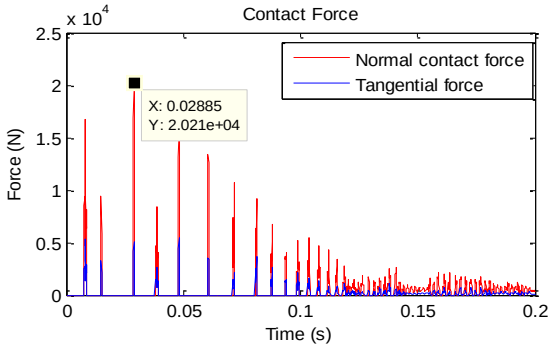

(b) Bronze

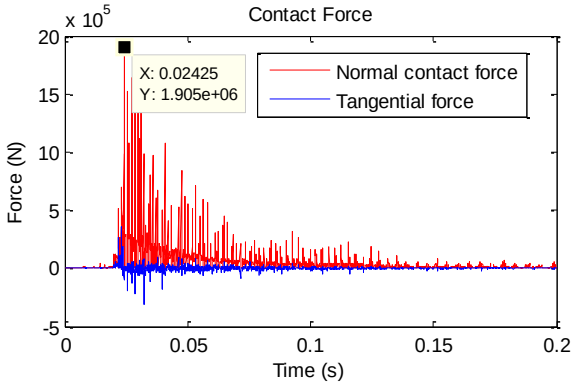

(c)Steel

Figure 86. Normal contact force with different materials

The time histories of the Von Mises stresses with different materials are shown as Figure 87. It can be seen that, similar as the contact force, the steel AB has the highest peak Von Mises stress during the simulation transient time period, and the bronze type AB has the lowest Von Mises stress because it doesn't generate the reverse whirl. The maximum Von Mises stresses of the aluminum and the steel AB are 150Mpa and 250Mpa. Both of them surpass their yield stresses, 137Mpa and 206Mpa respectively [23]

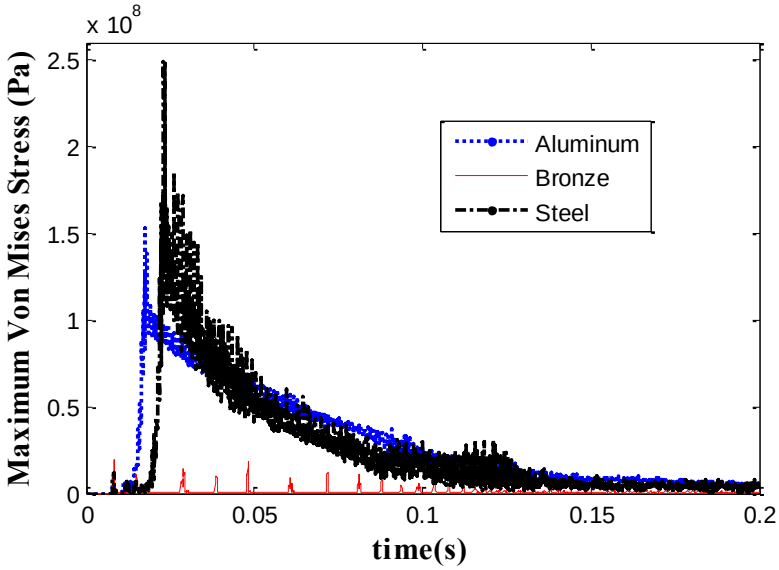

Figure 87. Maximum Von-Mises stress time history with different materials

Figure 88 shows the Von Mises stress distribution when the maximum Von Mises stress is occurring. It can be seen that the steel has the largest Von Mises stress. The bronze AB has the lowest Von Mises stress because there is no reverse whirl. It shows that the higher Von Mises stress levels extend beyond the immediate contact area due to vibration and deformation of the sleeve bearing.

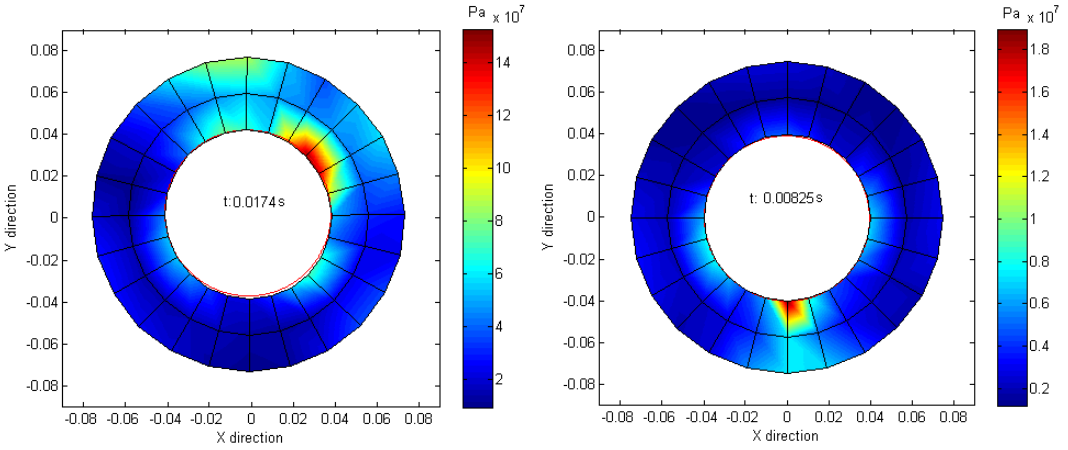

(a)Aluminum (b) Bronze

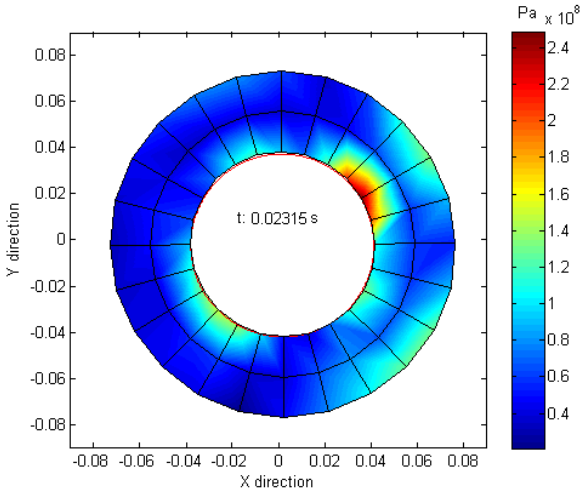

(c). Steel

Figure 88. Maximum Von Mises stress with different materials

Figure 89 shows the variations of the peak temperatures with different materials. The aluminum temperature is higher than bronze and steel during the first few hits. This is because the aluminum AB has the highest friction coefficient which induces reverse whirl. Additionally, it has the lowest thermal mass. Therefore, it can generate more heat power during contact and the temperature can also rise quicker. With the same heat convection boundary condition, the aluminum AB has a higher cooling rate which may be

caused by its relatively low thermal mass. The bronze has the lowest peak temperature in the first few hits. However, due to the sliding friction and the relatively concentrated contact area, its peak temperature gradually increases and surpasses the peak temperatures of the aluminum and steel AB. Its cooling rate is higher than the steel AB and lower than the aluminum AB.

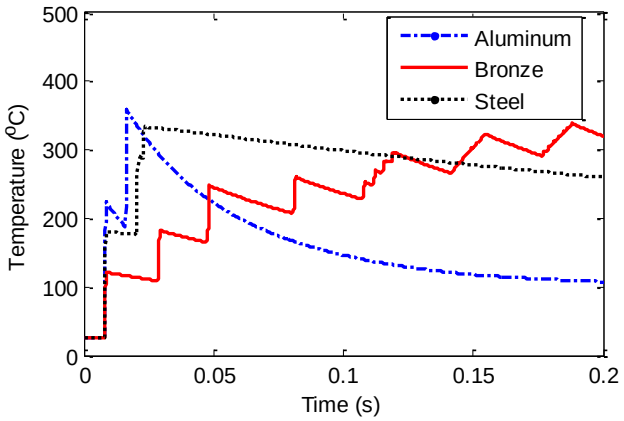

Figure 89. Variation of the peak temperature with different materials under unlubricated conditions

Figure 90 shows the temperature distributions when the peak temperature in the 0.2s transient period occurs for different materials. It can be seen that without the reverse whirl, the peak temperature usually occurs on the bottom of the sleeve bearing. The nodes, which have been impacted by the rotor, also have relatively higher temperatures. When there is reverse whirl, the temperature is about evenly distributed.

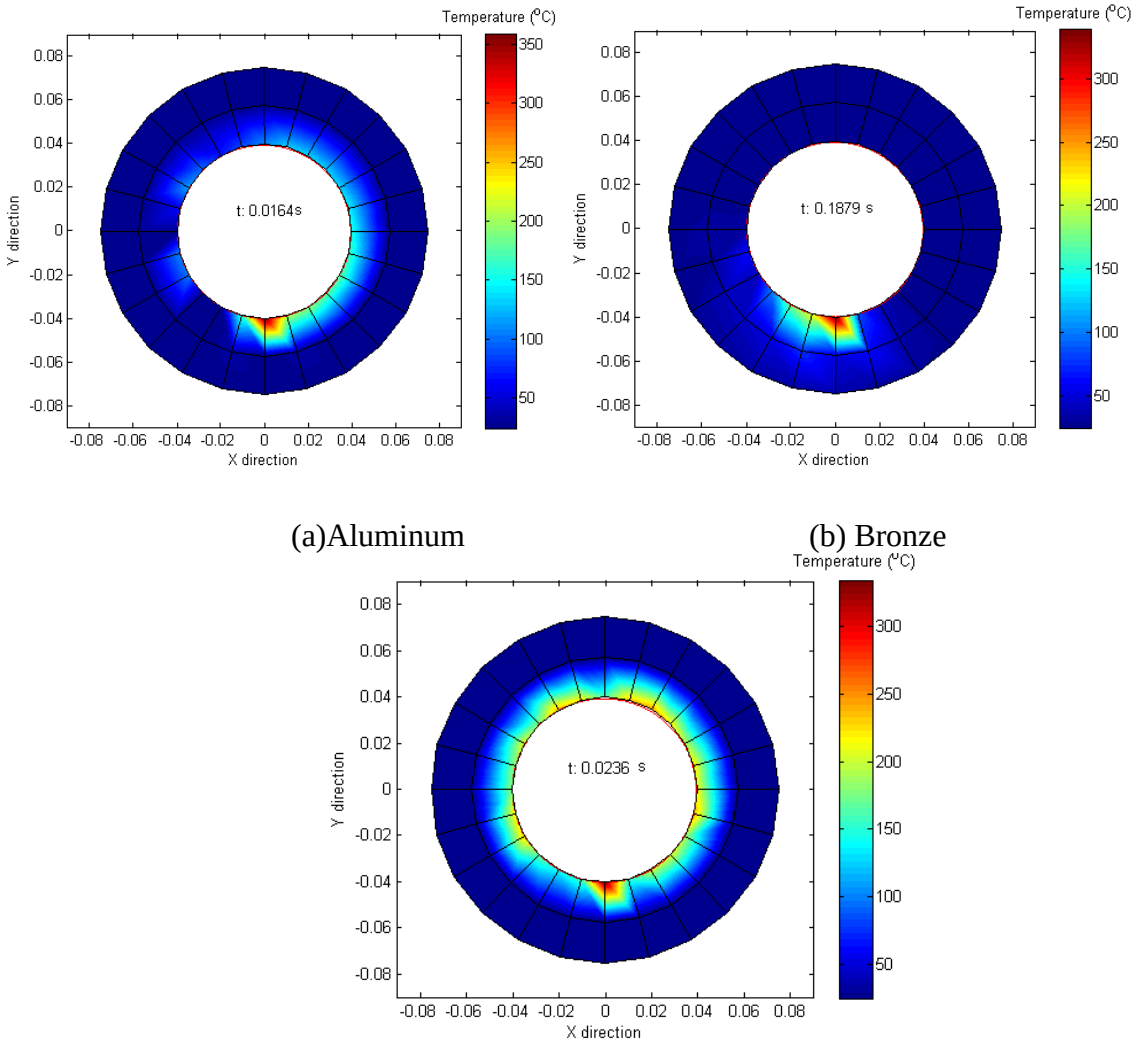

(a)Aluminum (b) Bronze

(c) Steel

Figure 90. Temperature distribution with different materials

From the above discussion, the unlubricated bronze AB does not generate reverse whirl, so it has the lowest normal contact force and Von Mises stress. However, due to its sliding friction and the concentrated contact area, it gradually gets the highest peak temperature among these three materials. Both aluminum and steel AB cases exhibit reverse whirl and have high contact force and Von Mises stress. Thus it can be seen that

without lubrication bronze performs better for this Auxiliary bearing simulation study as compared with steel and aluminum. Currently, all the friction coefficients in the above discussion are selected based [23] and [24].

6.6 Conclusion

The dynamic and thermal responses of the sleeve type Auxiliary bearing during the rotor drop event are analyzed. The bearing is constructed by the 2D plane strain model. The 2D heat transfer model is also integrated. Additionally, the thermal load, which is caused by the thermal expansion, is updated at each time step based on the temperature variation. For the drop analysis, the rotor is represented by a Timoshenko beam model. The temperature distributions and Von Mises stress distributions are predicted. The model is validated and compared with the experimental data from reference 13. The influences of different lubrication conditions, sleeve bearing materials are analyzed. The results provide the following findings.

1. The computation results qualitatively agree with the test data from Swanson et al.

2. When there is no reverse whirl, the areas with higher temperatures are all located near the contact points. When there is reverse whirl, the temperature is nearly evenly distributed.

3. Higher friction coefficients will result in higher contact force and Von Mises stress. The reverse whirl may lead to higher stress than the material's yield stress in the simulation cases.

4. The occurrence of reverse whirl does not necessarily cause higher peak temperatures than cases without reverse whirl. The normal contact force is very high but the friction force in rolling contact is relatively low and there is no slip, during pure rolling contact reverse whirl. Thus, the generated heat may less than in the sliding friction cases without reverse whirl.

5. By comparing the 3 types of unlubricated materials (stainless steel, bronze and aluminum), we found that using the stainless steel material can result in the highest normal contact force and Von-Mises stress. It is because it has the highest Young's modulus and a relatively high friction coefficient (0.5). Additionally, with the same heat convection boundary condition, due to its higher thermal mass, the steel sleeve bearing has the lowest cooling rate. The aluminum sleeve AB has the highest peak temperature in the first few hits but its cooling rate is also the highest. This may result from having the lowest thermal mass. The bronze sleeve AB's cooling rate is in the middle among the three materials considered and it also has the lowest peak Von Mises stress according to the simulation results. Thus, the bronze has the best performance for this application. This conclusion should be viewed with knowledge that the simulation results were very sensitive to the friction coefficient, which typically has considerable uncertainty. The friction coefficients in this paper are based on reference 10 and 13. Friction coefficients vary due to machining quality and environmental conditions, thus the final design of the AB for a given application should consider the material, machining and environment, and include a reasonable uncertainty in the friction coefficient.

The fatigue life calculated by the stress cycle and material S-N curve will be analyzed in the future. Additionally, sometimes the bearing will fail due to the extremely high local temperature such as in the thermal abrasion wear effect. Because the 2-D temperature distribution has been obtained, the thermal abrasion wear will be included to improve the fatigue life prediction of the sleeve bearing.

CHAPTER VII

ROTOR-AUXILIARY BEARING TEST RIG DEVELOPMENT AND RESULTS

This chapter discusses a new auxiliary bearing test rig wherein the rotor is spun at a high speed as initially supported with a self-aligning bearing and a tapered roller bearing. The drop test is initiated when the drive motor is mechanically pulled axially backwards, separating it from the rotating assembly, and in this process the gap in the magnetic coupling that connects the motor and rig rotor is suddenly thrust open. Next, the outer race of the tapered roller bearing is pushed forward by a solenoid-spring system opening a clearance in the bearing to let the rotor drop freely onto the Auxiliary bearing. The complete separation of the shaft from the tapered roller bearing was experimentally confirmed. A three axes piezoelectric load cell is installed under the Auxiliary bearing housing to measure the impact forces on the Auxiliary bearing during rotor drops. The high stiffness of the load cell and its support along with the 10 kHz DAQ sampling rate yield highly accurate measurements in both the horizontal and vertical directions. Tachometers are installed to measure the spin speeds of both the rotor and the Auxiliary bearing inner race. Parameters that varied during the rotor drop tests include Auxiliary bearing clearance, mass imbalances and rotational speed. The condition that the AB inner race is locked is considered as well. The friction coefficient between the rotor and auxiliary bearing inner race is carefully measured based on the three axes load cell. Then, the measured contact forces and vibrational motions are correlated with the high fidelity nonlinear auxiliary bearing model. In the simulation model, both the nonlinear Hertzian

contact and thermal expansion effect among each bearing component are considered. The flexible rotor is composed by the Timoshenko beam element. The simulation and experiment results agree well. This work lays the foundation of the experimental study of the fatigue life estimation of the auxiliary bearing. Additionally, the developed test rig enables the experimental analysis of the methods to reduce the contact and friction forces such as adding Auxiliary bearing dampers, changing Auxiliary bearing types and utilizing the surface coating techniques.

7.1 Test Rig Description

With reference to Figure 91, the rotor is run-up to the drop speed supported by a self-aligning bearing and a tapered roller bearing.

A solenoid driven mechanism then pushes the tapered roller bearing outer race outward in a nearly instantaneous manner, which creates a clearance between the tapered roller bearing TPR (Figure 2) inner and outer races to allow the rotor to drop onto the auxiliary bearings. This action is preceded by retraction of the motor which opens the magnetic coupling to insure that the deceleration of the rotor after drop is due solely to the friction in the bearings. Most papers with experimental results for rotor drops onto AB limited response measurements to the ensuing vibrations. A few papers also include measurements of the impact and friction forces between the rotor and the AB. This is a very important consideration since rolling element bearing life predictions rely on bearing loads and not shaft vibration. AB contact forces are measured in [15] however four single-axis (radial) load cells were employed which does not have a capability to directly measure friction forces that occur in the tangential direction. Reference [16] employed strain gage

load cells, which addresses the need to measure contact forces, however may introduce extra flexibility into the AB support and have bandwidth limitations. The latter is a concern since some contact force durations are shorter than 5 ms. The test rig in Figure 1 employs both vertically positioned and horizontally positioned three-axis piezoelectric load cells. This insures a near rigid AB support (1.75e9N/m), a capability to directly measure tangential as well as radial contact forces, a high measurement bandwidth (10 khz), and high load capacity (2.24 kN).

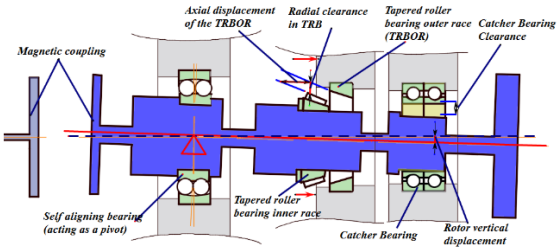

Figure 91. Rig diagram illustrating TRB release and magnetic coupling disengagement for rotor drop tests

(a) (b)

Figure 92. (a) Self-aligning bearing (b) Tapered roller bearing

Three-axial load cells were mounted in both the horizontal and vertical directions on the auxiliary bearing housing, as shown in Figures 3-5, to make the horizontal stiffness and vertical stiffness be nearly identical. The load cells were manufactured by PCB Piezotronics and have model number 261A01.

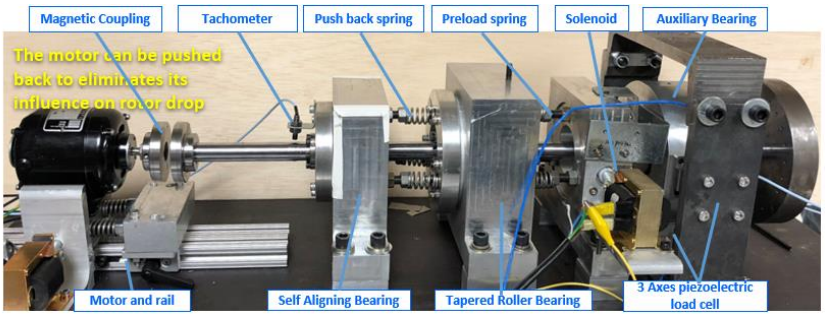

Figure 93. Auxiliary bearing test rig.

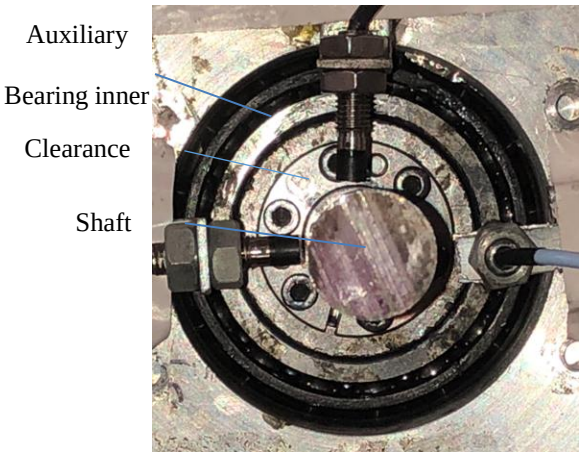

Figure 94. Mounting of the auxiliary bearing (The disk on the non-drive end is removed for a clearer view)

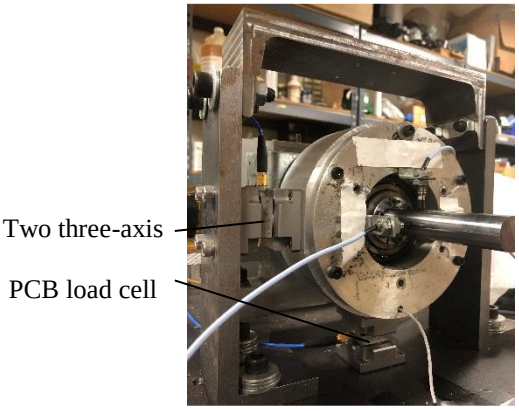

Figure 95. Two 3-axis load cells mounted on the AB housing (The disk on the non-drive end is removed for a clearer view of the load cell mounting)

(a) (b) (c)

Figure 96. Data acquisition system of the Catcher Bearing test rig. (a) Bently eddy current sensor (b) NI USB DAQ board with 8 channels (c) Load cell signal conditioner

Two Bently eddy current sensors were mounted as tachometers to capture the rotational speed of the rotor and of the auxiliary bearing inner race, as shown in Figure 4. The sampling rate for the data acquisition system shown in Figure 6 was 2000Hz, and the disk on the non-drive end of the test rig included 24 balancing holes. The clearance between the rotor and the AB was 0.2mm.

The results of a low speed (900 rpm) drop are presented here to illustrate the response measurement features of the test rig. Figure 97 shows the measured rotor orbit during the rotor drop event RDE. The displacement sensors are mounted to the AB housing, therefore the orbits indicate relative motion of the shaft very near to the AB with respect to the AB housing. The low friction and low rpm precluded the appearance of a clear whirl motion in this case. The horizontal and vertical relative rotor displacements are shown in Figure 98.

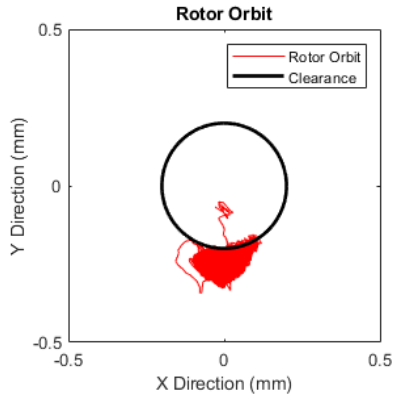

Figure 97. Rotor relative orbit for low speed RDE

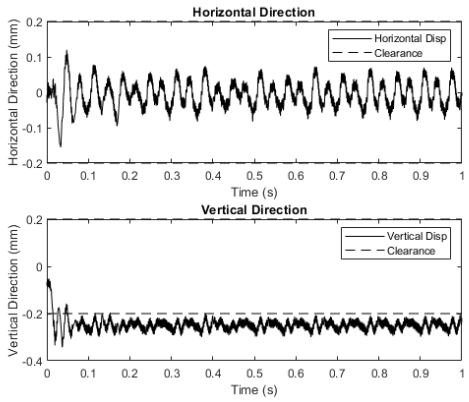

Figure 98. Rotor relative displacements for low speed RDE

Figure 99 shows the measured, total, horizontal and vertical contact forces between the rotor and the AB during the rotor drop event RDE. The largest contact force occurs at the first impact, and then the vertical forces converge to nearly 60N.

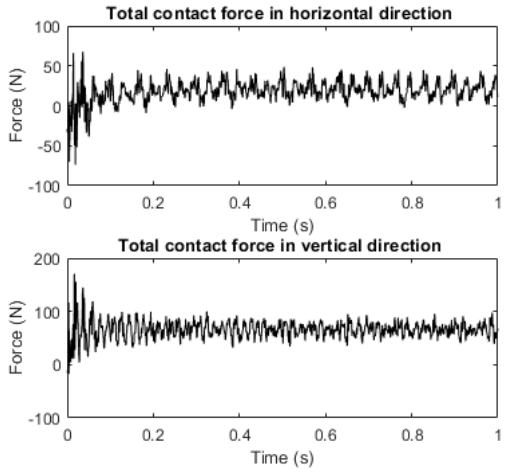

Figure 99. Contact forces for low speed RDE

The rotor's spin speed is seen to reduce from 900 rpm to 794.7 rpm over 5 seconds in Figure 100.

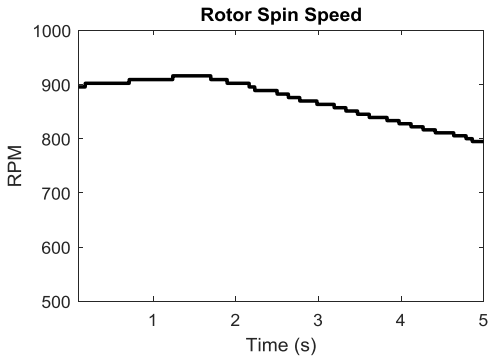

Figure 100. Rotor spin speed for low speed RDE

7.2 Observation of the ½ Subsynchrounous, Forward Whirl

The balanced rotor is run up through the critical speed at 1500 rpm (supported by the self-aligning bearing and the tapered roller bearing) to the drop speed of 6700 rpm. The drive motor is then retracted to remove the motor torque transmission through the coupling.

The test parameters are listed in Table 1 and the rotor dimensions are shown in Figure 101.

Table 15. Rotor drop test parameters

Rotational speed (RPM)	6700
Auxiliary bearing clearance(mm)	0.2
Auxiliary bearing type	7009 AB
Rotor material	Steel

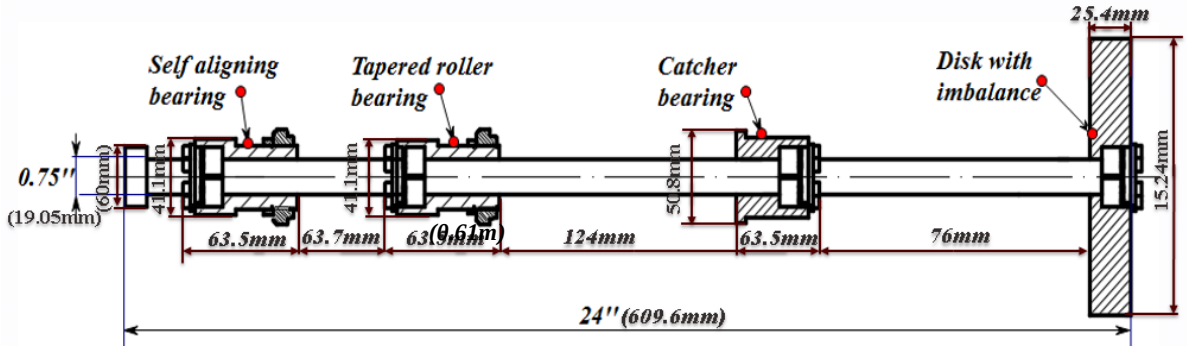

Figure 101. Dimensions of test rotor

The test results for the rotor orbit, displacements, whirl frequency and contact forces during the rotor drop event RDE are shown in Figures 12 through 17. Figure 11 (with the result in Figure 15) shows full clearance forward whirl from 15.5s to 42.4s and from 68s to 94s.

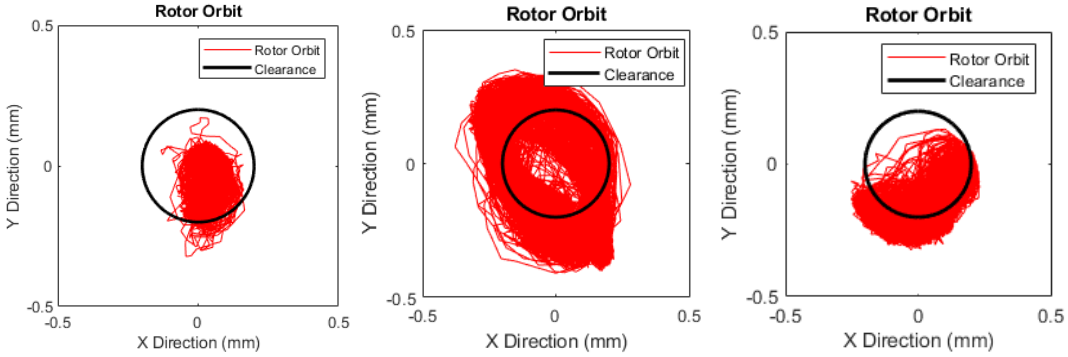

a. 0-15.5s b. 15.5-42.4s c. 42.4-68s

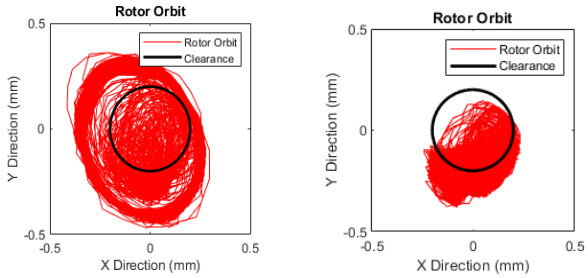

d. 68 - 94s e. 94 - 180s

Figure 102. Rotor orbit during a 6700 rpm RDE

Figure 103 and Figure 104 show the rotor's displacement in both the vertical and the horizontal direction and the rotor rpm during the RDE.

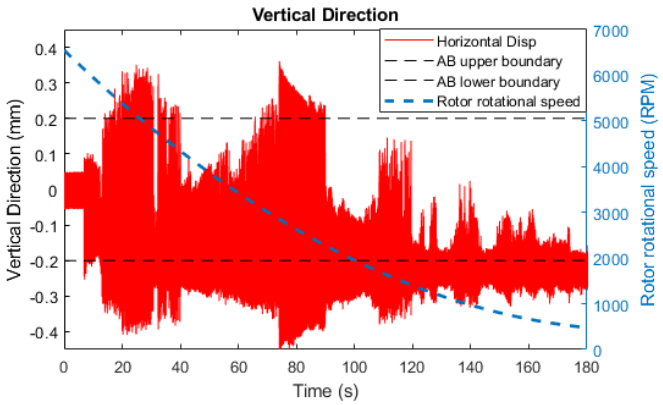

Figure 103. Vertical displacement during a 6700 rpm RDE

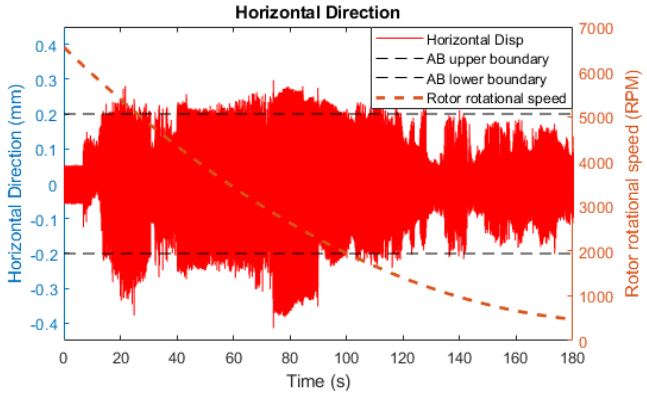

Figure 104. Horizontal displacement during a 6700 rpm RDE

Full clearance vibration occurs when the rotor passes through 6000RPM from 15s to 40s and passes through 3000RPM from 70s to 90s. The rotor orbits during these two periods are shown in Figure 12, which indicates full clearance whirl. Clearly, the magnetic pole gap would need to exceed these vibrations in the event that a magnetic bearing was installed.

In order to observe the rotor's whirl direction and frequency, the angular velocity of the rotor's whirling motion was calculated as

$$\dot{\varphi} = d \arctan \frac{y_r}{x_r} / dt = \frac{\dot{y}_r x_r - y_r \dot{x}_r}{{y_r}^2 + {x_r}^2} \tag{113}$$

where x_r is the rotor's displacement in x direction, y_r is the rotor's displacement in y direction, $\dot{x}_r$ is rotor's translation velocity in x direction, $\dot{y}_r$ is rotor's translation velocity in y direction. The $\dot{\varphi}$ negative (positive) values correspond backward (forward) whirl. The time history of the rotor whirling angular velocity $\dot{\varphi}$ during the RDE is shown in Figure 105. The whirl direction is the same as the rotor's spin direction during the large whirl occurrences, which indicates forward whirl.

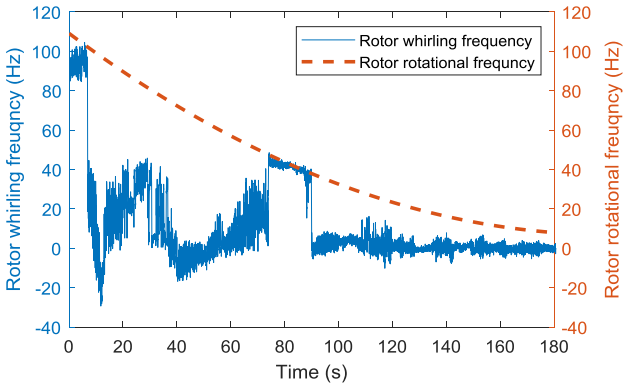

Figure 105. Rotor whirl frequency during a 6700 rpm RDE

Figure 106 shows that the frequency of the major vibration was near 48 Hz when the rotor speed was passing through 5700 RPM. This frequency is very near to ½ of the rotor's spin frequency. Similarly, the frequency of the major vibration was around 50Hz when the rotor speed was passing through 3000 RPM, indicating synchronous forward whirl. Both occurrences indicate that the frequency of the forward whirl is about 50Hz, which is explained in the discussion below.

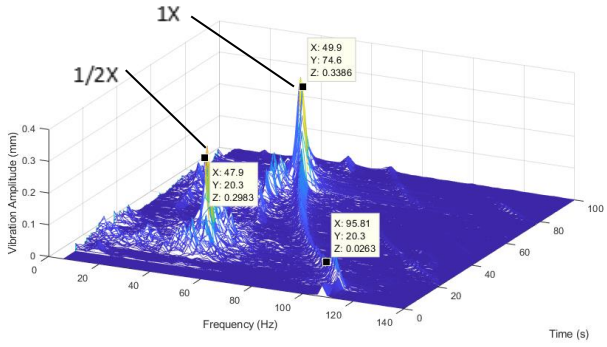

Figure 106. Spectrum analysis for a 6700 rpm RDE

Figure 107 shows that contact forces become very large during a sustained whirl occurrence, reaching a maximum of 825 Newtons. This is about 14 times the static reaction force between the rotor and the bearing as indicated in Figure 99.

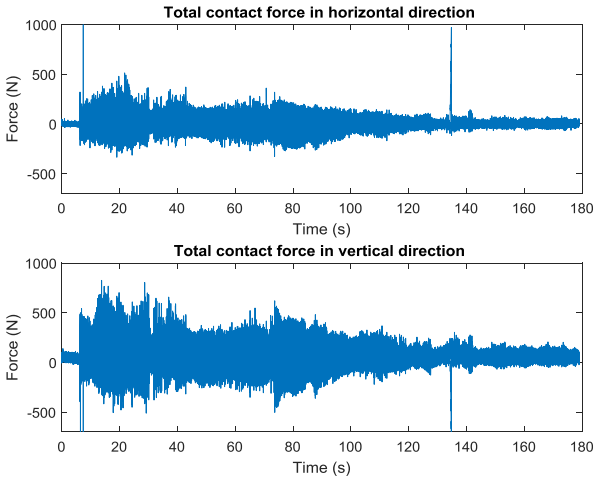

Figure 107. Contact forces during a 6700 rpm RDE

There was negligible axial contact between the rotor and the auxiliary bearing during these tests. Therefore, the forward whirl did not result from axial friction forces between the rotor and the auxiliary bearing. Additionally, the rotor was well balanced so that large imbalance was not the source of the measured forward whirl. Secondarily, if imbalance was the cause of the forward whirl the rotor would also experience forward whirl from 0s – 15.5s and 42s to 68, which did not occur. Therefore, another mechanism must have caused the measured forward whirl.

7.3 ½ Subsynchrounous Whirl and Mathieu-Hill Theory

½ subsynchronous whirl is an anomaly that has been discussed in the rotordymanic and machinery health literature.

Childs [25] utilized Mathieu – Hill theory to show that parametric excitation in the form of periodically changing stiffness can cause an instability when the excitation (spin) frequency coincided with twice the natural frequency. His discussion treated the case of rotor-stator rub that occurs in machines with conventional rolling element or fluid film type bearings.

Bently [18] identified 2 partial rub conditions that could be responsible for parametrically excited instability. The first was termed the "normal-tight" condition and referred to rubbing over a portion of the rotor's synchronous orbit causing a periodic increase in stiffness during the rub contact events. The second was termed the "normal-loose" condition and referred to a periodic loss of stiffness over a portion of the orbit due to a loose bearing fit. The rotor drop event is similar to a normal – loose state where the bearing stiffness is lost when the journal separates from the bearing bouncing occurs, or in a milder form when the bearing stiffness is significantly reduced due to the reduction in contact load, and corresponding reduction in the AB Hertzian contact stiffness.

Figure 108 shows a simplified Jeffcott type rotor model used to illustrate the possible occurrence of parametric instability in an AB supported machine during a drop event. The mass-clearance-spring-imbalance model is simple enough to analytically illustrate ½ subsynchronous vibration. A much more sophisticated model is then presented to demonstrate the phenomena numerically.

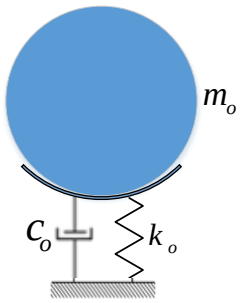

Figure 108. Simplified mass-clearance-spring-imbalance model to demonstrate AB parametric excitation

Let m_0 be the equivalent mass of the rotor at the auxiliary bearing location, and k_0 be the linearized equivalent stiffness of the auxiliary bearing system including the contact stiffness between the rotor and the AB. Consider the condition when the rotor drops onto the auxiliary bearing, and after a few bounces, experiences a small circular motion caused by imbalance of the rotor. While in contact, the rotor stays on the auxiliary bearing surface, and its equation of motion is

$$m_o\ddot{x}_o + c_o\dot{x}_o + k_o x_o = m_o e\omega^2 \cos(\omega t + \phi) - m_o g \tag{114}$$

However, the rotor intermittently losses contact due to the interplay of inertia, weight, stiffness and imbalance forces as shown in Figure 12 a, Figure 14, and Figure 110. Thus a more representative equation of motion is

$$m_o\ddot{x} + c_o\dot{x} + k_o(1-U(t))x = m_o e\omega^2 \cos(\omega t + \phi) - m_o g \tag{115}$$

where c_o is the equivalent damping of the rotor-AB system. and $U(t)$ is a time-dependent "contact" function which is shown in Figure 19. The test results for contact force in Figure 20 shows that the frequency of the step signal $U(t)$ is the rotational frequency.

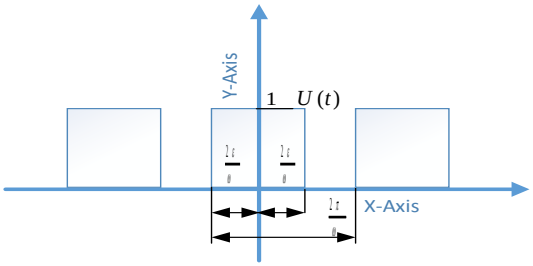

Figure 109. Time-dependent "contact" function $U(t)$

Figure 110 shows that the out of contact (loose) time is about 30% of the total vibration cycle time, which is the rotational period *T*.

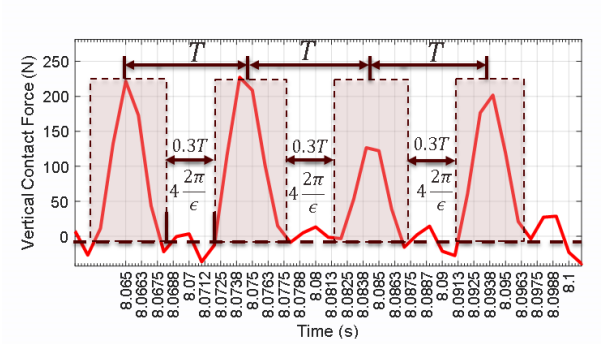

Figure 110. Measured vertical contact force caused by imbalance forces at 6000 rpm.

The rotor displacement $x(t)$ is approximated by the perturbed form

$$x(t) = x_o(t) + \eta(t)\text{, where } x_o(t) = D_{imb}\cos(\omega t) - D \tag{116}$$

where D is the static deflection on the AB stiffness due to weight and D_{imb} is the steady state imbalance response amplitude for the undamped system. Equation 3 becomes

$$\begin{aligned} &m_o(\ddot{x}_o + \ddot{\eta}) + c_o(\dot{x}_o + \dot{\eta}) + k_o(x_o + \eta) - k_o U(t)(x_o + \eta) \\ &\quad = me\omega^2\cos(\omega t + \phi) \end{aligned} \tag{117}$$

Substitution of (117) into (116) yields

$$m_o\ddot{\eta} + c_o\dot{\eta} + k_o\eta - k_o U(t)\eta = k_o U(t)x_o \tag{118}$$

Let $k_o = m_o\omega_n^{\,2}, c_o = 2\xi m_o\omega_n$, to obtain

$$\ddot{\eta} + 2\xi\omega_n\dot{\eta} + \omega_n^{\,2}\eta - \omega_n^{\,2}U(t)\eta = \omega_n^{\,2}U(t)x_o \tag{119}$$

The homogeneous component η_h of η satisfies

$$\ddot{\eta}_h + 2\xi\omega_n\dot{\eta}_h + \omega_n^{\,2}\eta_h - \omega_n^{\,2}U(t)\eta_h = 0 \tag{120}$$

The Fourier series expansion for $U(t)$ is

$$U(t) = \frac{1}{\pi}(2\varepsilon + 2\sum_{j=1}^{\infty}\frac{\sin(2\varepsilon j)}{j}\cos(j\omega t)) \tag{121}$$

Let $\tau = \omega t$ and then equation (121) becomes

$$\begin{aligned}\eta_h'' + 2\xi\frac{\omega_n}{\omega}\eta_h' + (\frac{\omega_n}{\omega})^2\eta_h \\ -\frac{2}{\pi}(\frac{\omega_n}{\omega})^2(\varepsilon + \sum_{j=1}^{\infty}\frac{\sin(2\varepsilon j)}{j}\cos(j\tau))\eta_h = 0\end{aligned} \tag{122}$$

The standard form of the Hill equation is

$$\eta_h'' + 2\mu\eta_h' + (\alpha + \gamma\sum_{j=1}^{\infty}(a_j\cos(j\tau) + b_j\sin(j\tau))\eta_h = 0 \tag{123}$$

where comparing to (9) and (10)

$$\alpha = \frac{\omega_n^{\,2}}{\omega^2}(1 - \frac{2\varepsilon}{\pi}),\ \gamma = \frac{2}{\pi}\left(\frac{\omega_n}{\omega}\right)^2,\ a_j = \frac{\sin(2\varepsilon j)}{j},\ b_j = 0 \tag{124}$$

Parametric excitation stability is evaluated by the location of (α, γ) on the Hill stability diagram in Figure 111.

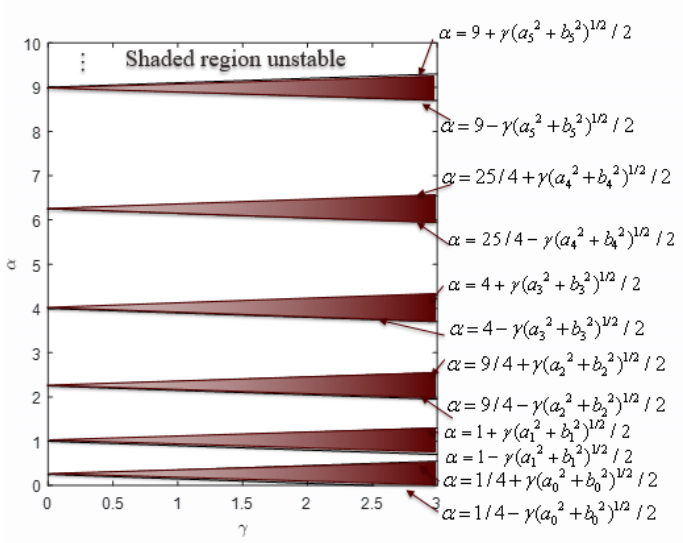

Figure 111. Instability bounds for Hill's Eq. by 1st order perturbation **[26]**

Based on the test data shown from Figure 102 to Figure 107, based on the measured contact force from Figure 110, the $\frac{2\varepsilon}{\omega}$ was about 0.003s to 0.0035s when ω was about 590 rad/s (94Hz) here $\varepsilon \approx 0.3 \times \pi / 2$. Therefore,

$$\alpha \approx 0.7 \frac{\omega_n^{\ 2}}{\omega^2} \tag{125}$$

Consider the condition when $\alpha = \frac{1}{4}$, i.e. $\omega = 1.7\omega_n$, and $\gamma = \frac{1}{2\pi}$, i.e. $a_1 = 0.8$, which lies in an instability zone in Figure 111. Therefore, large vibration is expected when the rotational speed is 1.7 times the natural frequency of the rotor-support system. Note that the rotational speed was not exactly twice of the natural frequency of the rotor-support system but only close to $2\omega_n$. Large vibration is also expected to occur when $\omega \approx \omega_n / 1.19$ ($\alpha = 1$) based on Figure 112.

A rotor drop test was conducted at zero rpm in order to obtain a value for ω_n. Figure 112 and 23 show the rotor's vertical displacement in the time and frequency domains, respectively. Figure 114 shows the contact force time domain response.

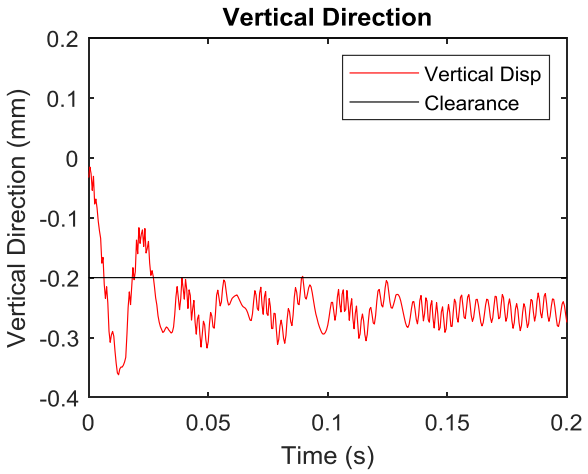

Figure 112. Vertical displacement of the rotor free drop test

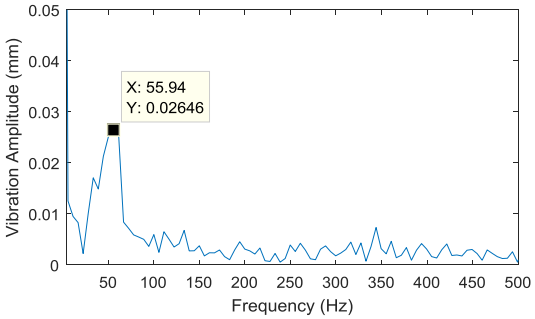

Figure 113. FFT of the displacement in Figure 112

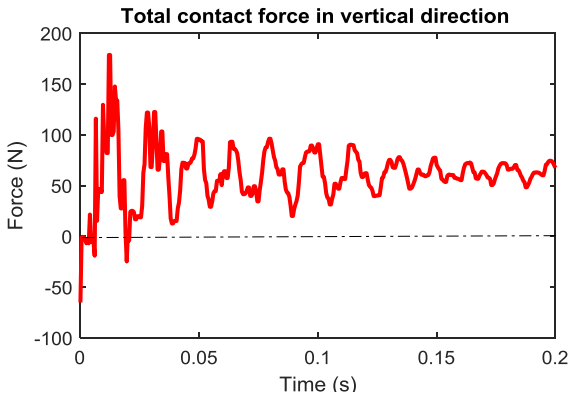

Figure 114. Vertical contact force

Figure 112 and Figure 114 show that after the first bounce, the rotor was in contact with the AB surface and both vibrate together with the measured natural frequency in Figure 113 (55.94Hz). Therefore $1.7\omega_n$ is 95 Hz, which is in the rotor spin frequency range (85Hz-100Hz) during the measured ½ X forward whirl. In like manner $\omega_n / 1.19$ is about 47Hz, which is in the range of the measured rotor spin frequency when the 1X forward whirl occurred. The measured whirl frequency (48Hz) is slightly smaller than the measured natural frequency (55.94Hz) with the rotor contacting the AB. This reduction in frequency is caused by the effect of the clearance between the rotor and AB, which increases the period.

This section utilizes Mathieu-Hill theory and test data to explain the 1/2X and 1X large vibration, which is caused by parametric excitation. A high fidelity numerical model is utilized to demonstrate that similar effects occur when the actual test rig is modeled with significant detail.

7.4 Correlation Between the Test and Simulation Results

Measurement of the friction coefficient between the rotor and the auxiliary bearing inner race was enabled with the two three-axis piezoelectric sensors that supported the AB. The inner race of the AB is locked by a pin when measuring the friction coefficient between the rotor and AB inner race. The rotor was spun on the AB very slowly, at less than 5RPM, with the load cells measuring the horizontal and vertical forces. The measured forces are shown in Figure 115.

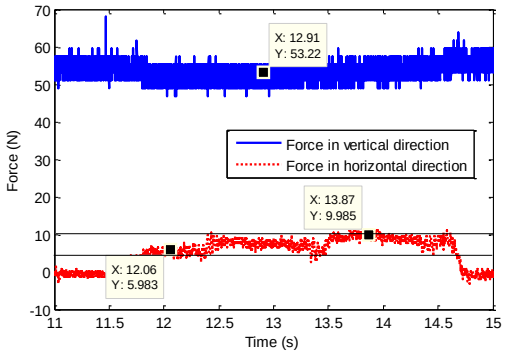

Figure 115. Measured contact force in the horizontal and vertical directions

From Figure 115, it can be seen that the range of the measured horizontal forces is between 5.411N to 9.985N. Thus, the friction coefficient is in the range of 0.11 to 0.187. Thus the friction coefficient is selected to be 0.15 in the simulations.

The simulation model is shown in Figure 116, where the self-aligning bearing is modeled by a 1e8N/m spring with no constraint in each angular direction.

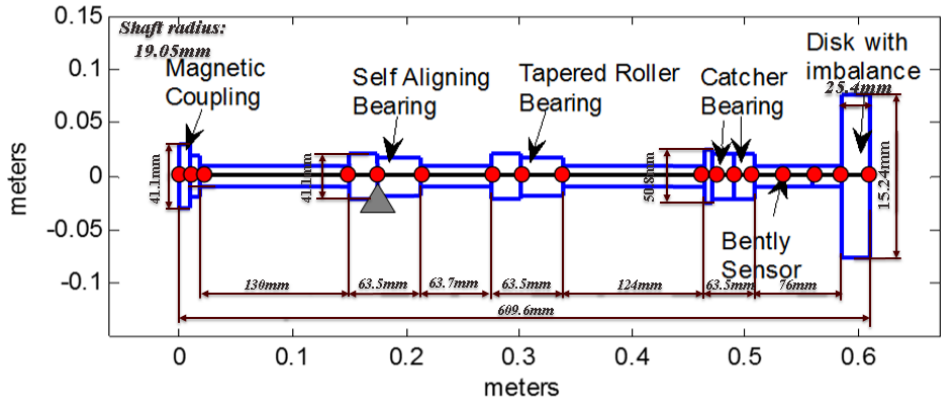

Figure 116. Simulation model of the rotor-catcher bearing system

The proportional damping utilized in the shaft model is 0.1%.

The first correlation study involved comparing the measured and predicted responses for a rotor drop at 0rpm. The parameters for this case are provided in Table 2.

Table 16. Simulation parameters 0 rpm drop test

Rotational Speed (RPM)	0
Housing Stiffness (N/m)	1.00E+09
Friction Coefficient	0.15
Imbalance (kg.mm)	0
Load cell vertical stiffness (N/m)	1.75E+09
Load cell horizontal stiffness (N/m)	5.00E+08
Rotor Proportional Damping	1.00E-03
Auxiliary bearing clearance(mm)	0.2
Auxiliary bearing damping(N.s/m)	3,500

The correlation of the vertical displacements and contact forces are shown in Figure 117 and 32. The AB damping coefficient was tuned to match the test data. It can be seen that the simulation results agreed well in the frequency and time domains. A good correlation for the zero-rpm drop test is very important to successfully predict the 1/2X forward whirl for rotor drop at high rpm since the whirl is highly related to the stiffness and damping of the support system. The apparent rotor motion outside of the clearance circle is large, which in part results from the sensor being located slightly outboard of the AB. The rotor tilts slightly during the drop event which amplifies the rotor motion at the sensor relative to the rotor motion at the AB centerline. The simulation displacements are at the location of the sensor in the model.

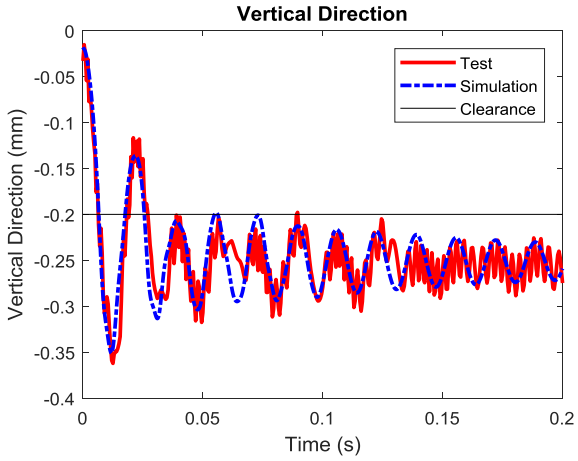

Figure 117. Rotor relative vertical displacement

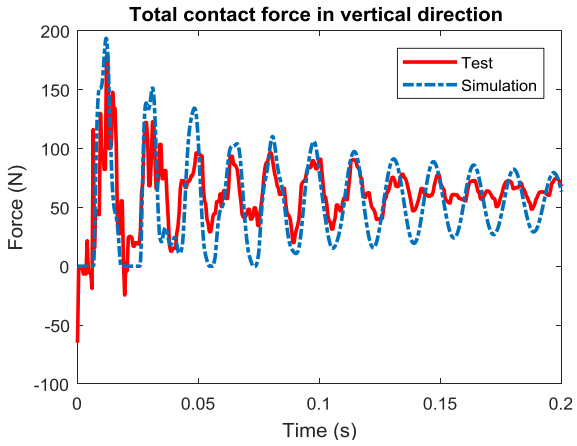

Figure 118. Vertical contact force

The following results are for non-zero rpm drop test event correlations. The test and simulation parameter values are listed in Table 17. The 0.13kg.mm imbalance is selected based on measurement and estimation.

Table 17. Simulation parameters 1,000 rpm drop test

Rotational Speed (RPM)	1,000
Housing Stiffness (N/m)	1.00E+09
Friction Coefficient	0.15
Imbalance (kg.mm)	0.13
Load cell vertical stiffness (N/m)	1.75E+09
Load cell horizontal stiffness (N/m)	5.00E+08
Proportional Damping	1.00E-03
Auxiliary bearing clearance(mm)	0.2
Auxiliary bearing damping(N.s/m)	3,500

The rotor orbit and time domain displacement correlations are shown in Figures 33 and 34, respectively. The response location is at the sensor position.

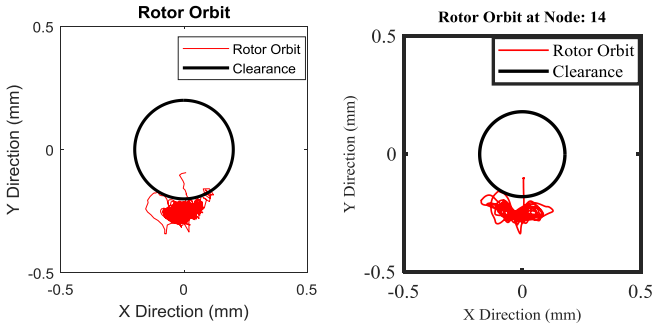

(a) Test (b) Simulation

Figure 119. Rotor orbit (a) test and (b) simulation results

The results show good qualitative, and to a smaller degree quantitative, agreement.

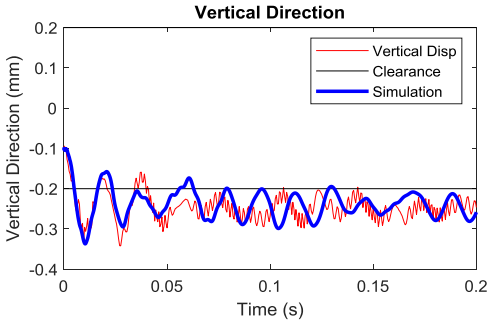

(a). Vertical rotor displacement comparison

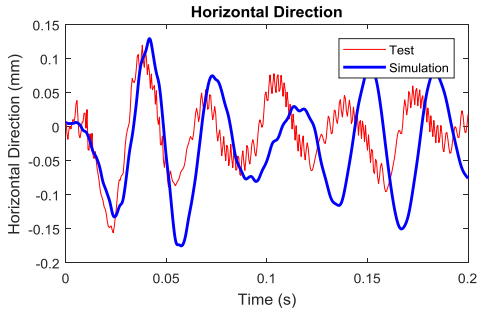

(b). Horizontal rotor displacement comparison

Figure 120. Displacement of the rotor at the sensor location

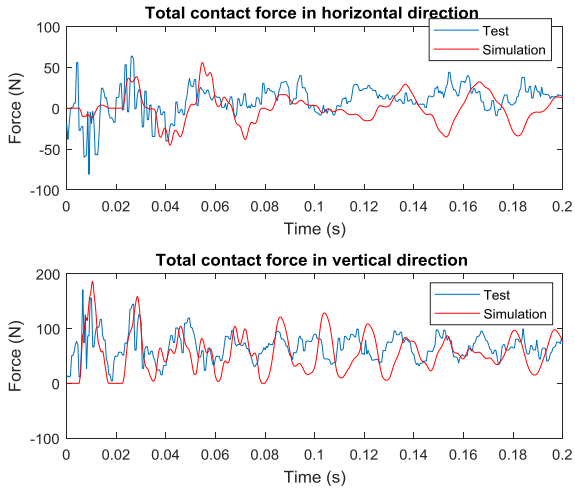

Figure 121. Contact force comparison

Figure 121 shows the horizontal and vertical contact force components vs. time during the drop event. The vertical forces are seen to dominate and the correlation shows less than an 8% difference in peak force amplitudes for the first 3 hits. The good agreement gives credibility to the simulation tool for predicting AB life which is greatly influenced by contact force.

The next correlation study corresponds to a drop speed of 5800 rpm. The parameters for the simulation is shown in Table 18.

Table 18. Simulation parameters 5,800 rpm drop test

Rotational Speed (RPM)	5,800
Housing Stiffness (N/m)	1.00E+09
Friction Coefficient	0.15
Imbalance (kg.mm)	0.13
Load cell vertical stiffness (N/m)	1.75E+09
Load cell horizontal stiffness (N/m)	5.00E+08
Rotor Proportional Damping (dim)	1.00E-03
Auxiliary bearing clearance(mm)	0.2
Auxiliary bearing damping(N.s/m)	3,500

Correlation results are shown in Figure 122 and Figure 123 for the orbits at the sensor locations and the rotor – AB contact forces. The orbits show good agreement especially in the vertical direction. The contact force agreement is not as good but does show common qualitative characteristics such as the emergence of whirl. In addition the prediction provides a reasonably conservative estimate of the measured forces.

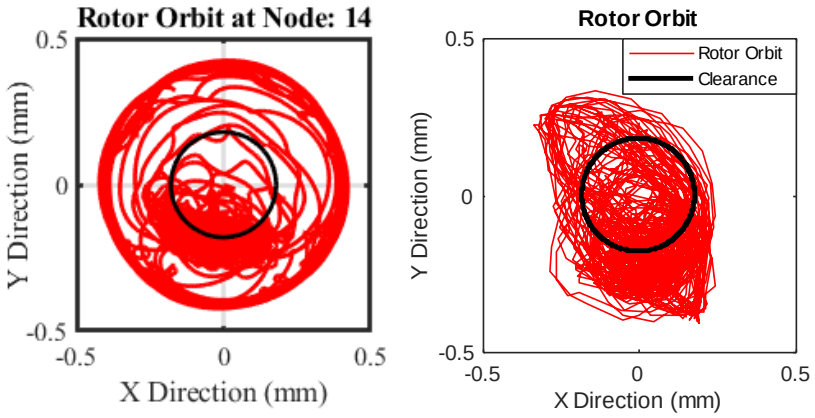

a. Simulation b. Test

Figure 122. Rotor Orbit (a) simulation and (b) test results

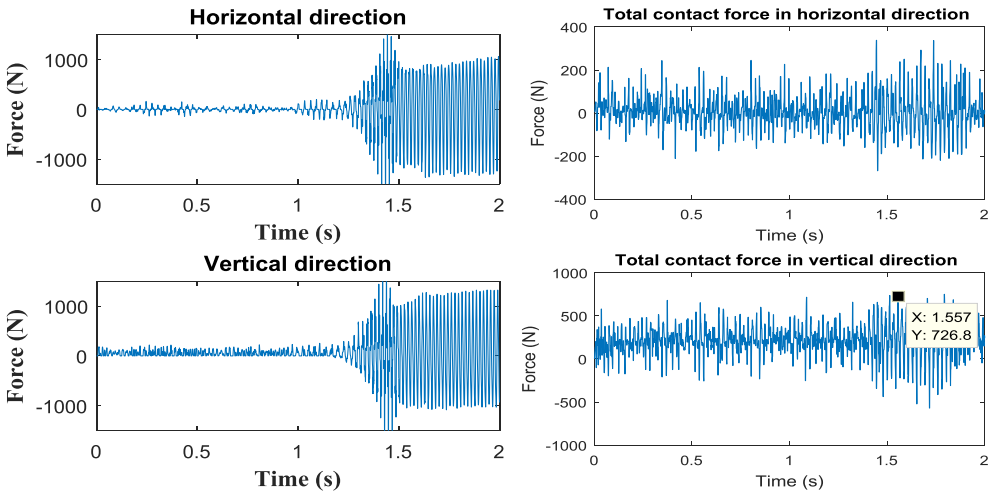

a. Simulation b. Test

Figure 123. (a) Simulation and (b) test contact force

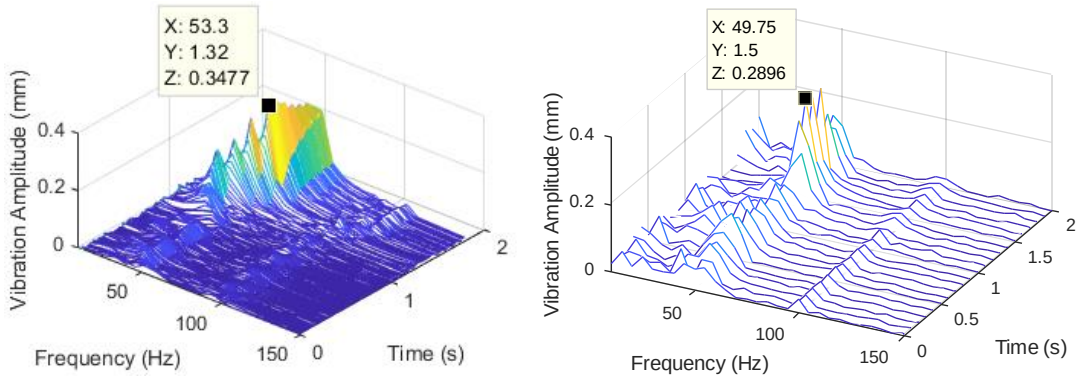

a. Simulation b. Test

Figure 124. Spectrum analysis

The large contact forces occur when the rotor begins to pass through the instability onsite speed, which is about twice the whirl frequency. Figure 124 shows good agreement between the test and predicted waterfall diagrams. The simulation successfully predicts the 1/2X vibration, and the vibration amplitudes are similar with the test results. Therefore,

the high fidelity numerical model successfully predicts the ½ X subsynchronous forward whirl.

7.5 Mitigation of the 1/2X, Subsynchrounous, Forward Whirl

Based on the previously mentioned simulations and analysis, the ½ subsynchronous forward whirl is caused by parametric excitation driven by the cyclic contact loss and the once per rev imbalance excitation. Dampers were developed for the AB support system to help mitigate the large vibration and contact forces occurring during the forward whirl events. An objective of the dampers was to reduce the natural frequency of the rotor-AB system, so as to reduce the whirl frequency, and resulting centrifugal force occurring during the whirl. Secondly, they can provide extra damping to the system to reduce the vibration amplitude to further mitigate the effects of forward whirl. The dampers can reduce the support stiffness to also reduce sharp impact forces that occur when the rotor impacts the AB.

Two types of dampers were implemented in the auxiliary bearing system of the test rig. One was elastomer O-rings, and the other was wavy spring.

7.5.1 Auxiliary Bearing Wavy Spring (WS) Damper

Damping devices such as the corrugated ribbon in Wilkes et al. [27] and the tolerance ring in Zhu et al. [28] appear in the AB literature. The shape of the metallic sheet WS is wavelike as illustrated in Figure 125, and it is placed between the ball bearing outer race and the bearing housing, as shown in Figure 126. The WS can increase the manufacturing tolerances of the bearing housing to reduce cost, and the WS has been

applied to an AB in [27]. The stiffness of the wavy spring is comparatively lower than the AB housing, thereby lowering the contact force after a rotor drop. The Coulomb friction forces due to internal sliding between the bearing outer race, the wavy spring (WS) and the housing, will also provide extra damping to increase the stability of the rotor-auxiliary bearing system.

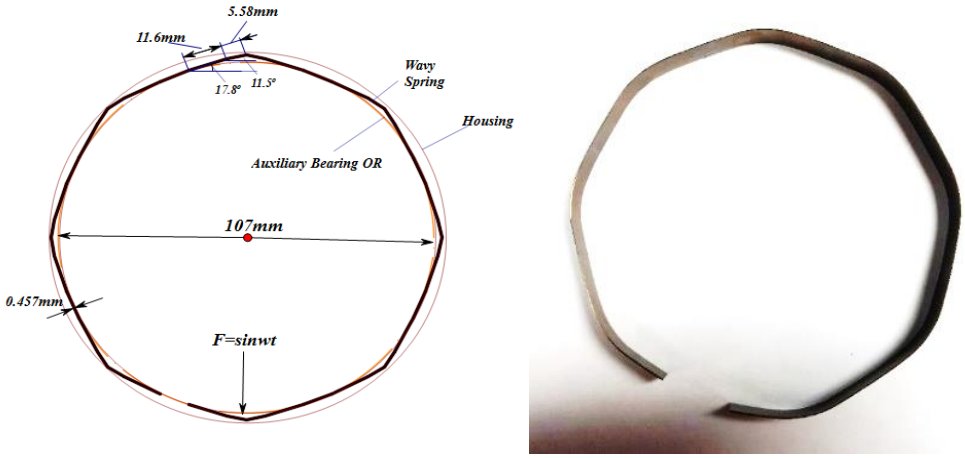

a. Wavy spring dimensions b. Wavy spring photo

Figure 125. Wavy spring geometry

Figure 126. Mounting of the wavy spring

A high spin speed rotor (6000RPM) drop test with wavy springs was conducted to test whether the WFS could effectively mitigate the large vibrations. Figure 127 shows the rotor orbits of the cases with and without the wavy springs. It can be seen that after including the wavy springs, the full clearance whirl was not observed.

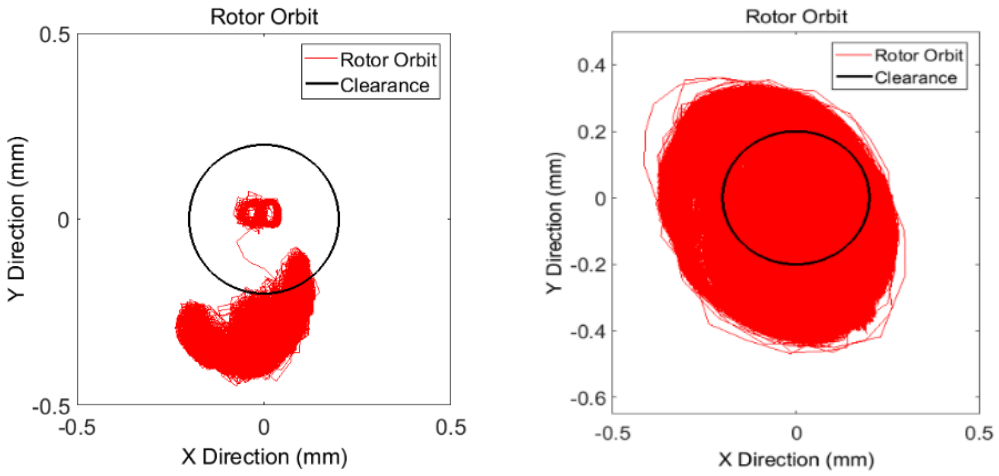

a. With wavy spring b. Without wavy spring

Figure 127. Rotor orbit

Figure 128 shows the waterfalls plot of the rotor's vertical displacements with and without the wavy springs. It can be seen that although the 1/2X and 1X vibrations were also observed in the case including the wavy springs, the vibration amplitudes were greatly reduced. The peak vibration amplitude of the 1/2X vibration was reduced from 0.2935mm to 0.1053mm, while the peak vibration amplitude of the 1X vibration is reduced from 0.3537mm to 0.1123mm. Therefore, the wavy springs could successfully mitigate the 1/2X and 1X vibrations.

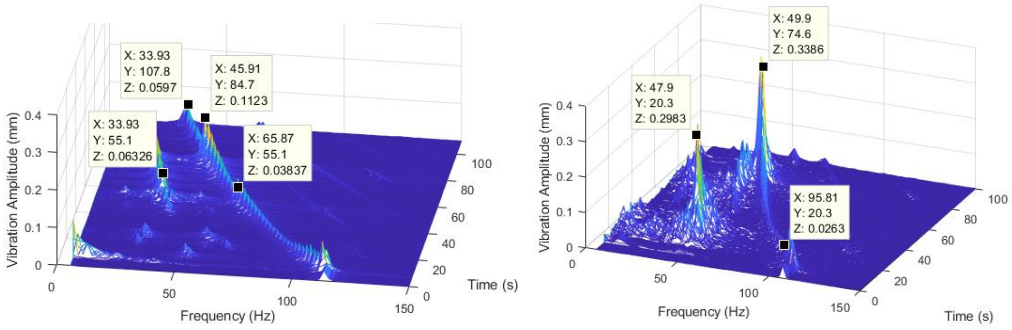

a. With wavy spring b. Without wavy spring

Figure 128. Waterfall plot of the rotor vertical displacement

Figure 129 shows the measured contact forces in both the horizontal and vertical directions for the cases with and without the wavy springs. It can be seen that both of the contact forces in horizontal and vertical directions are greatly reduced after including the wavy springs. The peak contact force is reduced from 825N to 253.7N. Therefore, the wavy spring can effectively greatly reduce the rotor bearing contact force and increase life.

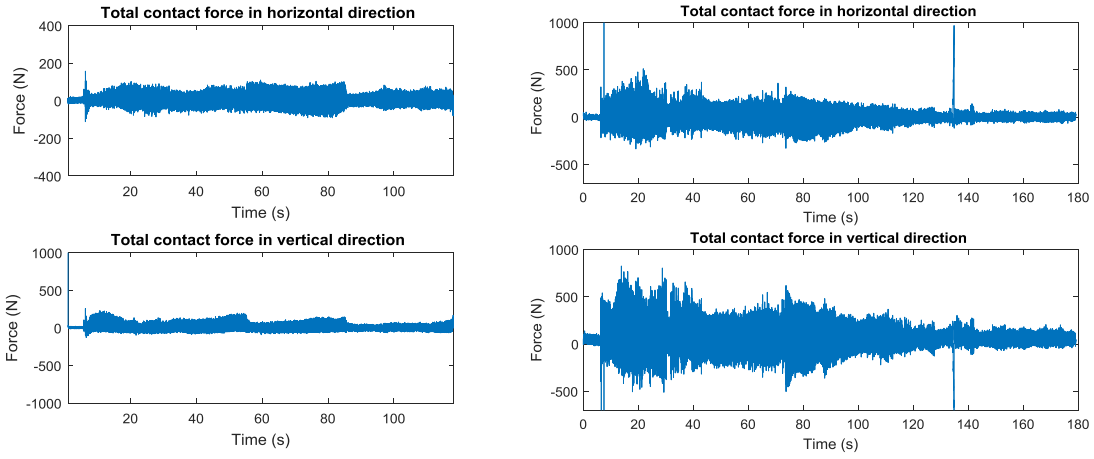

a. With wavy spring b. Without wavy spring

Figure 129. Contact force during rotor drop

Therefore, the results show that the wavy spring can significantly reduce the contact force and the vibration.

7.5.2 Auxiliary Bearing O-Ring Damper

Elastomeric dampers are widely used in rotating machines due of their simplicity, inherent combination of stiffness and damping, and no need for seals or an oil supply. The elastomer O-rings were integrated into the AB support as shown in Figure 130 and Figure 131.

The Viton O-ring's are inserted in 2 slots machined into a cylindrical cartridge. The O-ring's squeeze ratio can be adjusted by inserting shims into the slots. Shims are used to align the AB during the mounting process since the two O-ring assemblies may not be exactly identical causing the AB to slightly tilt.

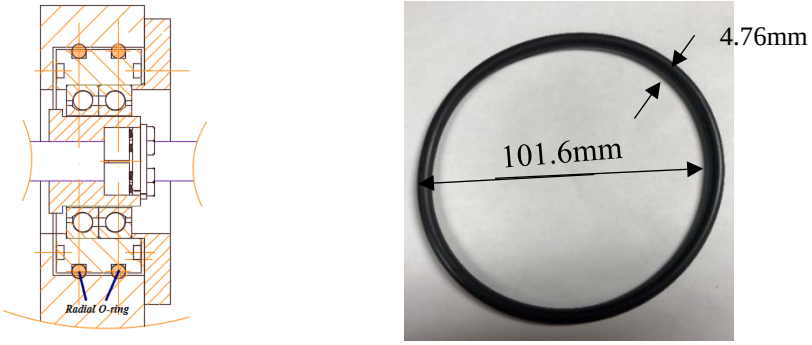

a. b.

Figure 130. a. Drawing of the O-ring mount and b. photo of the O-ring

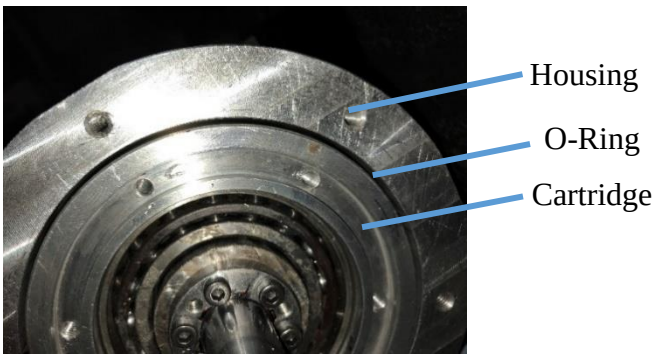

Figure 131. Mounting of the O-ring

A high spin speed rotor drop test with O-rings was conducted to test whether the O-ring would effectively mitigate large vibration and contact forces. Figure 132 shows rotor orbits with and without the O-rings. It can be seen that full clearance whirl is eliminated by including the O-ring damper.

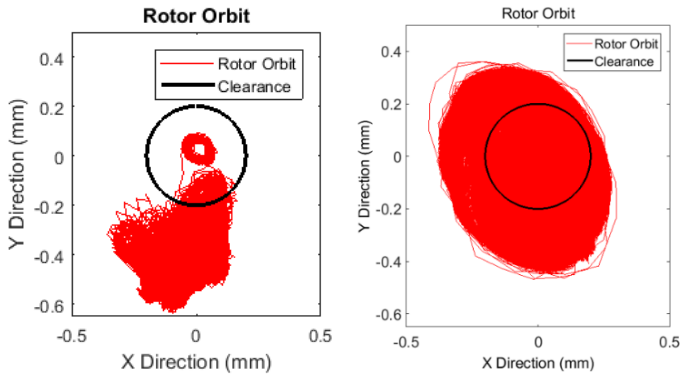

a. With O-rings b. Without O-ring

Figure 132. Rotor orbit

Figure 133 shows the measured contact forces in both the horizontal and vertical directions for the cases with and without the O-rings. These forces were significantly reduced after including the O-rings. The peak contact force is reduced from 825N to 220.7N which will have a very positive impact on AB life.

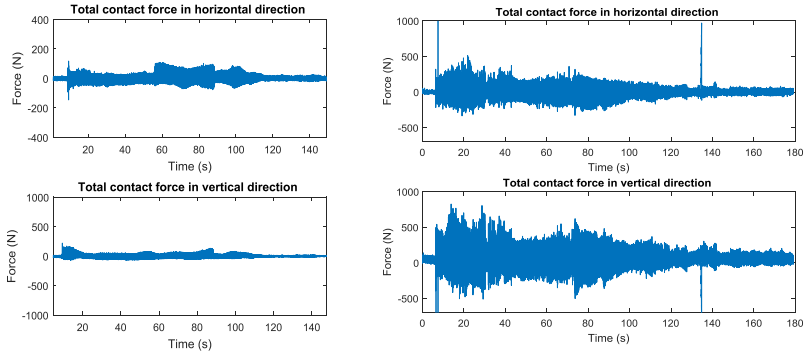

a. With O-rings b. Without O-rings

Figure 133. Contact force during rotor drop

Figure 134 shows a waterfall plot of the rotor's vertical displacements with and without the O-rings. It can be seen that although the 1/2X and 1X vibrations occur in the case including the O-rings, the vibration amplitudes are greatly reduced. The peak vibration amplitude of the 1/2X vibration was reduced from 0.2935mm to 0.09738mm, while the peak vibration amplitude of the 1X vibration is reduced from 0.3537mm to 0.1799mm. Therefore, the O-ring damper successfully mitigated the 1/2X and 1X vibrations. The results show that the O-rings significantly reduced the contact forces and the vibration amplitudes.

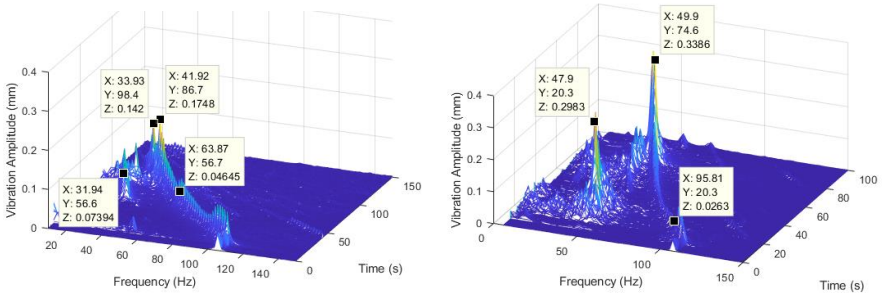

a. With O-rings b. Without O-rings

Figure 134. Waterfall plot of the rotor vertical displacement for the (a) With and (b) Without O-rings cases

7.6 Conclusion

Previous publications provide insightful explanations to the phenomena of forward whirl during drop events on AB, a phenomena which on the surface appears counter intuitive when considering only tangential friction forces. These explanations include friction from axial loading of the AB and large imbalance. A goal of the present work was to identify an alternative cause for AB forward whirl when axial loading is negligible and the rotor is finely balanced. The works of Childs, Bently and others on periodic rub contact provided an impetus for applying parametric vibration theory, in the form of the Mathieu-Hill equation, to the AB drop event response, to explain the experimentally observed near synchronous and near ½x subsynchronous forward whirl responses. The 1/2x response occurred near to when the rotor speed was approximately twice the undamped natural frequency. This provided a physical mechanism to better understand the observed forward whirl. A high fidelity, numerical rotordynamics model, including a detailed ball bearing model, was then developed to provide a high reliability simulation tool for predicting drop event response. The correlation of the model's predictions and test results for vibration and contact force during a drop event was very good. The next part of the paper highlights implementation of experimental means to suppress the high vibrations and contact loads that were measured during the forward whirl periods during a drop event. Large reductions of vibration and contact force were achieved utilizing an AB wavy spring damper and an AB O-ring damper.

Future work will include perfecting the component models of the wavy spring and O-ring dampers, increasing the efficiency of the rotordynamics – AB simulation software, and testing an AB – squeeze film damper.

CHAPTER VIII

SUMMARY AND POSSIBLE FUTURE WORKS

The previously described works are designed to develop high fidelity auxiliary bearings and the related damper models together with the related experiments. The contributions and novelties of the research include:

1) Integrated a high fidelity grooved squeeze film damper model considering the fluid inertia effect into the auxiliary bearing system;

2) Integrated a high fidelity wavy spring damper model into the auxiliary bearing system, considering the multi contact nodes' frictions between the wavy spring and the ABOR and the bearing housing.

3) Integrated a frequency dependent elastomer O-ring model into the auxiliary bearing system.

4) Developed a 2D elastic thermal coupled plane strain sleeve type auxiliary bearing model, which can predict the 2D temperature distribution and 2D stress distribution;

5) Auxiliary bearing test rig development, enabling the contact force measurement, rotor orbit measurement, rotor rotational speed measurement, auxiliary bearing inner race measurement, and eliminating the influence of the motor during rotor drop.

6) Observation and explanation of ½ subsychronous forward whirl during rotor drop.

7) Auxiliary bearing damper system testing, investigated the influence of the auxiliary bearing dampers (wavy spring and O-rings) on the rotor drop orbit and contact

forces. Mitigate the ½ subsychronous forward by including the wavy spring and the elastomer O-rings.

While the possible future works may include:

1) Experimental analysis of the sleeve type auxiliary bearings, which includes the influence of different material, with different temperatures especially in high temperature environments.

2) Test of rotor drop onto the sleeve type auxiliary bearings in the super critical CO2 environment.

3) Model the sleeve type auxiliary bearing with 3D finite elements.

4) Experimental analysis when a rotor drops onto the auxiliary bearing with the forces in both axial and lateral directions from auxiliary bearings.

REFERENCES

[1] A Gelin, Pugnet JM, Hagopian J D, "Dynamic behavior of flexible rotors with active magnetic bearings on safety auxiliary bearings," in *Procedings of 3rd Inernational Conference on Rotor Dynamics*, Lyon, France, 1990.

[2] T Ishii, R. G. Kirk, "Transient Response Techique Applied to Active Magnetic Bearing Machinery During Rotor Drop," *ASME Journal of Vibration and Acoustic,* vol. 118, pp. 154-163, 1996.

[3] Guangyong Sun, Alan Palazzolo, A Provenza, G Montague, "Detailed ball bearing model for magnetic suspension auxiliary service," *Journal of sound and vibration,* vol. 269, no. 3, pp. 933-963, 2004.

[4] Guangyong Sun, Alan Palazzolo, "Rotor drop and following thermal growth simulations using detailed auxiliary bearing and damper models," *Jounral of sound and vibration,* vol. 289, no. 1, pp. 334-359, 2006.

[5] Jung gu Lee, Alan Palazzolo, "Catcher bearing life prediction using a rainflow counting approach," *Journal of tribology,* vol. 134, no. 3, p. 03301, 2012.

[6] Jason Wilkes, J. Moore, D. Ransom, G. Vannini, "An Improved Catcher Bearing Model and and Explanation of the Forward Whirl/Whip Phenomenon Observed in Active Magnetic Bearing," *ASME J. Eng. Gas Turbines Power,* vol. 136, 2013.

[7] Adolfo Delgado, Luis San Andres, "A Model for Improved Prediction of Foce Coefficients in Grooved Squeeze Film Dampers and Oil Seal Rigns," *Journal of Tribology*, pp. 032202-1-12, 2010.

[8] Matthew T. Caprio, Brian Murphy, John Herbst, "Spin Commisioning and Drop Tests of a 130 kW-hr Composite Flywheel," in *Proc. 9th Int. Symp. Magnetic Bearings*, Lexington, KY, 2004.

[9] Yili Zhu, Yongchen Zhang, "Optimal Design of Tolerance Ring in Double-Decher Auxiliary Bearing System," *The Open Mechanical Engineering Journal*, vol. 9, pp. 618-213, 2015.

[10] A. J. Smalley, M. S. Darlow, R. K. Mehta, "The Dynamic Characteristics of O-Rings," *Journal of Mechanical Design*, pp. 132-138, 1978.

[11] David Ransom, Andrea Masala, Jeffrey Moore, Giuseppe Vannini, Massimo Camatti, Michel Lacour, "Development and application of a vertical high speed motor-compressor simulator for rotor drop onto auxiliary bearings," in *Proceedings of the thirty-eighth turbomachinery symposium*, Houston, TX, USA, 2009.

[12] Y. Zhu, "Dynamic Analysis of Auxiliary Bearing with Elastic Ring," *Journal of Mechanical Engineering*, vol. 47, 2011.

[13] Federal Mogul News Update, "Federal-Mogul Magnetic Bearings, Mystic, CT," [Online]. [Accessed 1999].

[14] E. E. Swanson, K. V. S. Raju, R. G. Kirk, "Test Results and Numerical Simulation of AMB ROtor Drop," in *Proc. 6th Int'l Conf. on Vibrations in Rotating Mach.*.

[15] E. E. Swanson, R. G. Kirk, "AMB Rotor Drop Initial Transient on Ball and Solid Bearings," in *Proceedng of Magnetic Bearing*, 1995.

[16] Jason Wilkes, T. Allison, "A General Model for Two-Point Contact Dry-Friction Whip and Whirl," in *ASME. Turbo Expo*, Montreal, Canada, 2015.

[17] Paweł Olejnik, Jan Awrejcewicz, Michal Fečkan, Modeling, analysis and control of dynamical systems : with friction and impacts, World Scitific, 2018.

[18] N. Raje, F. Sadeghi, "Statistical numerical modeling of sub-surface initiated spalling in bearing contacts," *Journal of Engineering Tribology*, vol. 223, no. 6, pp. 849-858, 2009.

[19] L. S. Andres, "Squeezze Film Dampers: Operation, Models and Technical Issues, Lecture Note," [Online].

[20] Don-Hyun Lee, Young Cheol Kim, Kyung-Woong Kim, "The effect of Coulomb friction on the static performance of foil journal bearings," *Tribology International*, vol. 43, no. 5-6, pp. 1065-1072, 2010.

[21] A. Palazzolo, Vibration Theory and Application with Finite Elements and Active Vibration Control, Wiley, 2016.

[22] J. N. Reddy, Finite Element Method, Thired Edition, McGraw-Hill, 2005.

[23] E. Oberg, Machinery's Handbook, 23rd Edition, New York: Industrial Press Inc..

[24] R. Norton, Machinery's Handbook, New York: Industrial Ress Inc..

[25] D. Childs, Turbomachinery Rotordynamics, Phenomena, Modeling, & Analysis, Wiley-Interscience, 1993.

[26] G. M. Mohmoud, "Stability Regions for Couples Hill's Equations," *Physica A*, pp. 239-249, 1997.

[27] Jason Wilkes, J. Moore, D. Ransom, G. Vannini, "An Improved Catcher Bearing Model and an Explanation of the Forward Whirl/Whip Phenomenon Observed in Active Magnetic Bearing," *ASME J. Eng. Gas Turbines Power*, vol. 136, 2013.

[28] Yili Zhu, Yongchen Zhang, "Optimal Design of Tolerance Ring in Double-Decker Auxiliary Bearing System," *The Open Mechanical Engineering Journal*, vol. 9, pp. 618-213, 2015.

[29] Y. Zhu, "Dynamic Analysis of Auxiliary Bearing with Elastic Ring," *Journal of Mechanical Engieering*, vol. 47, 2011.

[30] A. Palazzolo, "Nonlinear Vibration lecture notes," College Station, TX, 2015.

[31] R. L. Norton, Machine Design, An Integraed Approach, Prentice Hall.

[32] B. T. M. M. T. Caprio, "Spin Sommissioning and Drop Tests of a 130 kW-hr Composite Flywheel," in *9th International Symposium on Magnetic Bearings*, Lexington, KY, 2004.

[33] J. C. P. J. Schmied, "Behavior of a One Ton Rotor Being Dropped Into Auxiliary Bearings," in *Third International Symposium on Magnetic Bearings*, Alexandria, VA, 1992.

[34] T. A. Harris, Rolling Bearing Analysis, 5th edition, New York: Wiley, 2006.

[35] M. A. Fumagalli, Modeling and Measurement Analysis of the Contact Interaction between a High Speed Rotor and its Stator, ETH: Doctoral Dissertation, 1997.

[36] D. Bentley, "Forced Subrotative Speed Dynamic Action of Rotating Machinery," in *ASME*, Dallas, TX.

[37] Fawaz Y. Saket, M. Necip Sahinkaya, Patrick S. Keogh, "Thouchdown Bearing Contact FOrces in Mangetic Bearing System," in *Proceedings of ASME Turbo Expo 2013*, San Antonio, TX, 2013.

[38] E. E. Swanson, R. G. Kirk, "Test Results and Numerical Simulation of AMB Rotor Drop," in *AMB ROtor Drop Initial Transient on Ball and Solid Bearings*, 1995.

[39] L. Hawkins, Alexei Filatov, Shamim Imani, Darren Prosser, "Test Results and Analytical Predictions for Rotor Drop Testing of an Active Magnetic Bearing Expander/Generator," *Journal of Engineering for Gas Turbines and Power*, pp. 522-529, 2007.

[40] P S Keogh, M O T Cole, "Rotor Vibration with Auxiliary Bearing Contact in Magnetic Bearing Systems Part 1: Synchronous Dynamics," *J. Mechanical Engineering Science*, pp. 377-392, 2003.

[41] Luis San Andres, Sung-Hwa Jeung, "Response of a Squeeze Film Damper-Elastic Structure System to Multiple and Consecutive Impact Loads," *Journal of Engineering for Gas Turbines and Power*, vol. 128, 2016.

[42] Andrea Masala, Giuseppe Vannini, David Ransom, Jeff Moore, Luc Baudelocque, "Numerical simulation and full scale landing test of a 12.5MW vertical motor compressor levitated by active magnetic bearings," in *Proceeding of ASME Turbo Expo* , Vancouver, British Columbia, Canada, 2011.

[43] Pawel Olejnik, Modeling, Analysis and Control of Dynamical Systems with Friction and Impacts, World Scitific, 2018.

[44] Gerhard Schweitzer, Eric H. Maslen, Magnetic Bearings Theory, Design, and Application to Rotating Machinery, London: Springer, 2009.

[45] John Tichy, Benyebka Bou-Said, "Hydrodynamic Lubrication and Bearing Behavior with Impulsive Loads," *Tribology Transactions,* vol. 34, pp. 505-512, 1990.

[46] "https://www.smalley.com/wave-springs/marcel-expanders," Smalley spring ring company. [Online].

[47] "http://www.borrelly.com/stock-dimensions/39-ball-bearing-spring-ribbon.html," Borrelly Spring Washers. [Online].

[48] P. McMullen, V. Vuong, L. Hawkins, "Flywheel Energy Storage System With AMB's and Hybrid Backup Bearings," in *10th International Symposium on Magnetic Bearings*, Martigny, Switzerland, 2007.

[49] Said Lahiri, Ilmar F. Santos, "Experimental quantification of dynamic forces and shaft motion in two different types of backup bearings under several contact conditions," *Mechanical Systems and Signal Processing,* 2013.

[50] Xiao Kang, Guojun Yang, Suyuan Yu, "Dynamic behavior of the AMB's vertical arranged rotor during its drop process," in *22nd International Conference on Nuclear Engineering*, Prague, Czech Republic, 2014.

[51] A Gelin, Pugnet JM, Hagopian J D, "Dynamic behavior of flexible rotors with active magnetic bearings on safety auxiliary bearings," in *Proceedings of 3rd Inernational Conference on Rotor Dynamics*, Lyon, France, 1990.

[52] Xiao Kang, Alan Palazzolo, "Dynamic and Thermal Analysis When Rotor Drop onto the Sleeve Type Auxiliary Bearings," *Journal of Engineering for Gas Turbines and Power,* vol. 140, pp. 022501-15, 2018.

[53] L. Hawkins, P. McMullen, R. Larsonneur, "Development of an AMB Energy Storage Flywheel for Commerical Application," in *8th International Symposium on Magnetic Suspension Technology*, Dresden, Germany, 2005.

[54] Jung gu Lee, Alan Palazzolo, "Catcher bearing life prediction using a rainflow counting approach," *Journal of Tribology,* vol. 134, no. 3, p. 03301, 2012.

[55] Guangyong Sun, "Auxiliary Bearing Life Prediction Using Hertzian Contact Bearing Model," *Journal of Sound and Vibration,* vol. 128, pp. 203-209.

[56] E. E. Swanson, R. G. Kirk, "AMB Rotor Drop Initial Transient on Ball and Solid Bearings," in *Proceeding of Magnetic Bearing*, 1995.

[57] Adolfo Delgado, Luis San Andres, "A Model for Improved Prediction of Foce Coefficients in Grooved Squeeze Film Dampers and Oil Seal Rings," *Journal of Tribology*, pp. 032202-1-12, 2010.